

ISSN en trámite



Geofísica Internacional

Revista Trimestral Publicada por el Instituto de Geofísica de la
Universidad Nacional Autónoma de México



México

Volume 61 Number 4
October - December
2022

— Geofísica Internacional —

Dr. José Luis Macías Vázquez
Director of Instituto de Geofísica

Dr. Arturo Iglesias Mendoza
President of Unión Geofísica Mexicana

Editor Chief

Dr. Servando De la Cruz-Reyna
Instituto de Geofísica, UNAM
sdelacrr@geofisica.unam.mx

Technical Editor

Mtra. Andrea Rostan Robledo
Instituto de Geofísica, UNAM
arostan@igeofisica.unam.mx

Editorial Board

Donald Bruce Dingwell
Earth and Environment
Ludwig Maximilian University of Munich,
Germany

Eric Desmond Barton
Departamento de Oceanografía
Instituto de Investigaciones Marinas, Spain

Jorge Clavero
Amawta Consultores, Chile

Gerhardt Jentzsch
Institut für Geowissenschaften
Friedrich-Schiller-Universität Jena, Germany

Peter Malischewsky
Institut für Geowissenschaften
Friedrich-Schiller-Universität Jena, Germany

François Michaud
Géosciences Azur
Université Pierre et Marie Curie, France

Olga Borisovna Popovicheva
Scobeltzine Institute of Nuclear Physics
Moscow State University, Rusia

Jaime Pous
Facultad de Geología
Universidad de Barcelona, Spain

Joaquín Ruiz
UA Science
University of Arizona, United States

Angelos Vourlidis
Solar Physics Branch
NASA Goddard Space Flight Center, United States

Théophile Ndougsa Mbarga
Department of Physics
University of Yaoundé I, Cameroon

Associate Editors

José Agustín García Reynoso
Atmospheric Science
Centro de Ciencias de la Atmósfera, UNAM,
Mexico

Tereza Cavazos
Atmospheric Science
Departamento de Oceanografía Física CICESE,
Mexico

Dante Jaime Morán-Zenteno
Geochemistry
Instituto de Geología, UNAM, Mexico

Margarita López
Geochemistry
Instituto de Geología, UNAM, Mexico

Ayto Gogichaisvili
Geomagnetism And Paleomagnetism
Instituto de Geofísica, UNAM, Mexico

Jaime Urrutia-Fucugauchi
Geomagnetism And Paleomagnetism
Instituto de Geofísica, UNAM, Mexico

Felipe I. Arreguín Cortés
Hydrology
Instituto Mexicano de Tecnología del Agua IMTA,
Mexico

William Lee Bandy
Marine Geology And Geophysics
Instituto de Geofísica, UNAM, Mexico

Fabian García-Nocetti
**Mathematical And Computational
Modeling**
Instituto de Investigaciones en Matemáticas
Aplicadas y en Sistemas, UNAM, Mexico

Graciela Herrera-Zamarrón
Mathematical Modeling
Instituto de Geofísica, UNAM, Mexico

Ismael Herrera Revilla
**Mathematical And Computational
Modeling**
Instituto de Geofísica, UNAM, Mexico

Rene Chávez Segura
Near-Surface Geophysics
Instituto de Geofísica, UNAM, Mexico

Juan García-Abdeslem
Near-Surface Geophysics
División de Ciencias de la Tierra CICESE, Mexico

Alec Torres-Freyermuth
Oceanography
Instituto de Ingeniería, UNAM, Mexico

Jorge Zavala Hidalgo
Oceanography
Instituto de Ciencias de la Atmósfera y Cambio
Climático, UNAM, Mexico

Shri Krishna Singh
Seismology
Instituto de Geofísica, UNAM, Mexico

Xyoli Pérez-Campos
Seismology
Instituto de Geofísica, UNAM, Mexico

Blanca Mendoza Ortega
Space Physics
Instituto de Ciencias de la Atmósfera y Cambio
Climático, UNAM, Mexico

Inez Staciari Batista
Space Physics
Instituto Nacional de Pesquisas Espaciais, Brazil

Roberto Carniel
Volcanology
Laboratorio di misure e trattamento dei segnali
DPIA, Università di Udine, Italy

Miguel Moctezuma-Flores
Satellite Geophysics
Facultad de Ingeniería, UNAM, Mexico

Assistance

Elizabeth Morales Hernández,
Management
eliedit@igeofisica.unam.mx



GEOFÍSICA INTERNACIONAL, Año 61, Vol. 61, Núm. 4, octubre - diciembre de 2022 es una publicación trimestral, editada por la Universidad Nacional Autónoma de México, Ciudad Universitaria, Alcaldía Coyoacán, C.P. 04150, Ciudad de México, a través del Instituto de Geofísica, Circuito de la Investigación Científica s/n, Ciudad Universitaria, Alcaldía Coyoacán, C.P. 04150, Ciudad de México, Tel. (55)56 22 41 15. URL: <http://revistagi.geofisica.unam.mx>, correo electrónico: revistagi@igeofisica.unam.mx. Editora responsable: Andrea Rostan Robledo. Certificado de Reserva de Derechos al uso Exclusivo del Título: 04-2022-081610251200-102, ISSN: en trámite, otorgados por el Instituto Nacional del Derecho de Autor (INDAUTOR). Responsable de la última actualización Saúl Armendáriz Sánchez, Editor Técnico. Fecha de la última modificación: 30 de septiembre 2022, Circuito de la Investigación Científica s/n, Ciudad Universitaria, Alcaldía Coyoacán, C.P. 04150, Ciudad de México.

El contenido de los artículos es responsabilidad de los autores y no refleja el punto de vista de los árbitros, del Editor o de la UNAM. Se autoriza la reproducción total o parcial de los textos siempre y cuando se cite la fuente completa y la dirección electrónica de la publicación.



Esta obra está bajo una Licencia Creative Commons Atribución-NoComercial-SinDerivadas 4.0 Internacional.

Contents

Intense Geomagnetic Storms in The Maximum Phase of Solar Cycle 24 Observed From a Low-Latitude Ground Station

Juan A. Lazzús, Ignacio Salfate, Pedro Vega-Jorquera

267

Identification for a Favorable Area of Groundwater Exploitation Based on Structural and Geoelectrical Data in Fractured Aquifer in Southern Brazil

César Augusto Moreira, Livia Portes Innocenti Helene

287

Content of Total Organic Carbon Using Random Forest, Borehole Imaging, and Fractal Analysis: A Methodology Applied in the Cretaceous La Luna Formation, South America

Jorge A. Leal F., Luis H. Ochoa G., Gustavo A. Sarmiento P.

301

Modelling of Residual Gravity Data due to a Near Surface Dyke Structure Using Damped SVD and Marquardt Inverse Methods

Ata Eshaghzadeh, Alireza Hajian

325

Seal Cap Resistivity Structure of Los Humeros Geothermal Field from Direct Current and Transient Electromagnetic Soundings

Carlos Flores¹, Thalia Avilés Esquivel, Claudia Arango-Galván, José Luis Salas

351

<https://doi.org/10.22201/igeof.00167169p.2022.61.4.2028>

Intense Geomagnetic Storms in The Maximum Phase of Solar Cycle 24 Observed From a Low-Latitude Ground Station

Juan A. Lazzús^{1,2,*} , Ignacio Salfate¹, Pedro Vega-Jorquera¹

Received: January 29, 2020; accepted: April 8, 2022; published on-line: October 1, 2022.

RESUMEN

Debido a las complejidades de la investigación magnetosférica, la instalación y gestión de nuevas estaciones terrestres magnéticas de acuerdo con los estándares modernos es crucial para monitorear las perturbaciones magnetosféricas y los fenómenos relacionados. En respuesta al desarrollo de nuevas herramientas in situ y conjuntos de datos tomados en tierra que respalden estos estudios, se evaluaron los datos generados por la estación terrestre magnética de baja latitud de La Serena (en las coordenadas geográficas: -29.827 , -71.261 ; y coordenadas magnéticas: -16.55 , 0.17) para describir tormentas geomagnéticas intensas. Esta estación en la ciudad de La Serena (Chile), es dependiente del Laboratorio de Física Espacial y Atmosférica de la Universidad de La Serena (LAFESAT). Con estos datos, estudiamos las cinco tormentas geomagnéticas más intensas ($Dst < -100$ nT) ocurridas durante la fase máxima del ciclo solar 24 (desde 2014 hasta principios de 2016). Los resultados muestran que las variaciones de la componente H de las mediciones de la estación La Serena son consistentes con las variaciones del índice Dst reportadas para cada tormenta analizada, obteniendo valores de coeficiente de correlación de hasta 0.97 para tormentas con $Dst < -200$ nT. Además, nuestros resultados son consistentes con la fuerte influencia que tienen de los sistemas de corriente magnetosférica/ionosférica sobre el componente H durante una intensa tormenta geomagnética.

PALABRAS CLAVE: Observatorio magnético, Componentes del campo geomagnético, Ciclo solar 24, Tormenta geomagnética del Día de San Patricio y Índice Dst.

Editorial responsibility: Marni Pazos

*Corresponding author at jlazzus@userena.cl

¹Departamento de Física, Universidad de La Serena, Casilla 554, La Serena, Chile.

ORCID: <https://orcid.org/0000-0003-1136-3395>

² Instituto de Investigación Multidisciplinario en Ciencias y Tecnología, Universidad de La Serena, Casilla 554, La Serena, Chile.

ABSTRACT

Due to the complexities of magnetospheric research, the installation and management of new magnetic ground stations according to modern standards is crucial for monitoring magnetospheric disturbances and related phenomena. In response to the development of new in situ tools and ground-based data sets that support these studies, data generated by La Serena low-latitude magnetic ground station (at geographic coordinates: -29.827 , -71.261 ; and magnetic coordinates: -16.55 , 0.17) to describe intense geomagnetic storms were evaluated. This station in the city of La Serena (Chile), is supported by the University of La Serena's Laboratory for Space and Atmospheric Physics (LAFE-SAT). With these data, we studied the five most intense geomagnetic storms ($Dst < -100$ nT) occurring during the maximum phase of solar cycle 24 (from 2014 to early 2016). Results show that the H component variations of the La Serena station measurements consistent with the Dst index variations reported for each storm analyzed, obtaining correlation coefficient values of up to 0.97 for storms with $Dst < -200$ nT. Also, our results are consistent with the strong influence of the magnetospheric/ionospheric current systems over the H component during an intense geomagnetic storm.

KEY WORDS: Magnetic Observatory, Geomagnetic field components, Solar cycle 24, St. Patrick's Day geomagnetic storm and Dst index.

INTRODUCTION

Ground-level magnetic field data are crucial for several applications, including monitoring of evolving geomagnetic storms and the space weather conditions (Love, 2008; Matzka *et al.*, 2010; Love & Finn, 2011; Mandaia & Korte, 2011; Onsager, 2012; Love & Chulliat, 2013; Waters *et al.*, 2015).

A geomagnetic storm is the strongest perturbation in the Earth's environment. The general triggering for geomagnetic storms is the magnetic interaction/reconnection between the Earth's magnetosphere and interplanetary magnetic field. These disturbances result in intense currents in the magnetosphere and ionosphere (Ganushkina *et al.*, 2018). The strongest geomagnetic storms occur when coronal mass ejections (CMEs) are emitted toward the Earth, causing a substantial injection of energetic particles drifting around the Earth causing a compression of the magnetosphere (Tsurutani *et al.*, 1988; Gosling *et al.*, 1991; Gopalswamy *et al.*, 2005; Chen, 2011; Joshi *et al.*, 2011; Webb & Howard, 2012), and at the same time an intensification of the currents in the magnetosphere-ionosphere system (Ganushkina *et al.*, 2018). The current systems that can be affected during a geomagnetic storm are: (1) the magnetopause currents shielding earth's dipole and the ring current; (2) the symmetric ring current; (3) the cross-tail current along with the closure currents on the magnetopause; and (4) the partial ring current, which connects the Region 2 field-aligned currents (Ganushkina *et al.*, 2018).

During the storm, the ring current particles which are energized causing a compression of the low-latitude horizontal component of the terrestrial magnetic field and change the magnetospheric ring current during a prolonged time interval (Gonzalez *et al.*, 1994). To quantify the effect of this current, the 1-hour-disturbance storm time (Dst) index is employed to characterize the intensity of the geomagnetic storms (Sugiura, 1964). This index uses the geomagnetic field data from 4 low latitude stations: Kakioka KAK (36.2°N , 140.2°E) in Japan; Honolulu HON (21.3°N , 158.0°W) in Hawaii; San Juan SJG (18.1°N , 66.2°W) in Puerto Rico; and Hermanus HER (34.4°S , 19.2°E) in South Africa. From these stations, the time series of the horizontal (H) component of the geomagnetic field

is obtained by subtracting the background magnetic field and the solar quiet (Sq) variation of the geomagnetic field. Thus, the H component is averaged over these stations and normalized to the geomagnetic equator, as $Dst = \overline{H} / \overline{\cos\theta}$, where θ is geomagnetic latitude and the overbars indicate the arithmetic average over longitude (Sugiura & Kamei, 1991). Additionally, other currents produced in the magnetosphere, such as the field-aligned and auroral currents (associated or not with a geomagnetic storm), cause subauroral geomagnetic disturbances that are used for calculating the 3-hour-planetary geomagnetic disturbance (Kp) index (Bartels *et al.*, 1949; Matzka *et al.*, 2021). This index is provided by 13 subauroral stations for eight three-hourly intervals of the day. Each station is calibrated according to its latitude and reports a K-index itself based on a quasi-logarithmic scale that characterizes the geomagnetic activity at the given location and time compared to a calm day curve. This activity is classified into a scale from 0 to 9 where 0 represents very little geomagnetic activity and 9 is an extreme activity (Matzka *et al.*, 2010; Matzka *et al.*, 2021).

Geomagnetic storms evolve in three phases: (1) the initial phase is an abrupt positive variation in the Dst index, called sudden storm commencement (SSC). An SSC is produced by sudden compression in the magnetosphere caused by an increment of the dynamic pressure of the solar wind. (2) the main phase where the Dst index takes negative values during the injection of energized plasma in the equatorial ring current until it reaches a minimum Dst value; and (3) the recovery phase where Dst values increase until they reach pre-sudden commencement values during the return of the geomagnetic field to normality (Gonzalez *et al.*, 1994; Loewe & Prölss, 1997). During this process, Dst values decrease from close to zero to negative until a minimum Dst value of later increases recovers values closer to zero. According to this minimum value, storms are classified into: weak ($-30 > Dst > -50$ nT, with $0 \leq Kp \leq 5$), moderate ($-50 > Dst > -100$ nT, with $5 < Kp < 7$), and intense ($Dst < -100$ nT, with $7 \leq Kp \leq 9$) categories (Gonzalez *et al.*, 1994; Matzka *et al.*, 2021). Thus, a negative Dst index value indicates increasing intensity of the ring current (Gonzalez *et al.*, 1994; Loewe & Prölss, 1997). This Dst decay is controlled by the ring current and the magnetospheric tail current. During the main phase, the ring current increases its density of O⁺ ions, of ionospheric origin, contributing to the plasma pressure in the inner magnetosphere (Keika *et al.*, 2013; Daglis *et al.*, 1999; Welling *et al.*, 2011). During the recovery phase, particle transport into the ring current slows, allowing various loss processes to reduce ring current particle fluxes to their quiet-time level. The loss mechanisms are more efficient near dawn and dusk (Le, 2013) and explain why the ring current and the ionosphere control the electric fields in the interior of the magnetosphere at dawn and dusk (Bogdanova *et al.*, 2014). These effects are due to the electric fields that appear during dusk near the equatorial ionosphere (Tsurutani *et al.*, 2012). Thus, the ring current becomes the dominant Dst source during intense geomagnetic storms, but during moderate storms, its contribution to Dst is comparable with the tail current's contribution (Kalegaev & Makarenkov, 2008).

Intense storms could represent a latent hazard for space technology systems and human activities on the Earth's surface (Hapgood, 2011; Love & Finn, 2011; Love *et al.*, 2014). To study these events, magnetic ground stations around the world monitor the onset of solar-induced storms and give warnings that help diminish related economic losses (Love & Finn, 2011; Onsager, 2012; Love & Chulliat, 2013). Magnetometer measurements of ground stations at low latitudes are used to monitor the electrodynamics of the ionosphere that control ionospheric plasma distributions during a geomagnetic storm (Kamide *et al.*, 1981; Richmond & Kamide, 1988; Yizengaw *et al.*, 2014; Anderson *et al.*, 2004).

In this contribution, we studied five intense geomagnetic storms during the maximum phase of solar cycle 24 by using ground-level magnetic field data gathered at the La Serena low-latitude magnetic ground station as a response to development of new in situ tools and ground-based data sets that support magnetospheric research.

SOLAR CYCLE 24

Solar activity (such as sunspot area, radio flux, solar flares, CMEs, and other related phenomena) can increase or decrease following an 11-year cycle of activity (Schwabe, 1844). Each solar cycle has unique characteristics; however, solar cycle 24 has exhibited hitherto unusual and unprecedented solar activity (Richardson, 2013; Kamide & Kusano, 2013; Gopalswamy *et al.*, 2014; Pesnell, 2014; Watari, 2017).

Solar cycle 24 (2008–present) (Pesnell, 2014), preceded by the lowest and the longest solar minimum in the last solar cycles (Russell *et al.*, 2010; Richardson, 2013), is the most recently completed solar cycle (Kamide & Kusano, 2013; Gopalswamy *et al.*, 2014; Watari, 2017). The extended minimum from ~2008 to 2010 (Gopalswamy *et al.*, 2014; Lingri *et al.*, 2016) was followed by high activity during a short phase beginning at the end of 2011 (Lingri *et al.*, 2016; Watari, 2017) with an activity peak reached before 2013, as it then decreased and peaked again in 2014 (Gopalswamy *et al.*, 2014; Lingri *et al.*, 2016), registering its maximum activity phase from 2014 to 2015 (Pesnell, 2014). Several authors have speculated that this extraordinarily low minimum has shown unexpected Sun and solar wind conditions compared only with strange states of the Sun occurred in the past, such as Maunder and Dalton minima (Agee *et al.*, 2010; McDonald *et al.*, 2010; Feynman & Ruzmaikin, 2011; Hao & Zhang, 2011; White *et al.*, 2011; Williams & Pesnell, 2011). The Maunder minimum (1645–1715) and Dalton minimum (1790–1820) were periods with extremely low sunspot numbers where the Earth experienced abnormal cooling times (Eddy, 1976; Mauquoy *et al.*, 2002; Owens *et al.*, 2017).

INSTRUMENTS AND DATA

In this study, we used data recorded by a low-latitude magnetic ground station. The La Serena magnetic ground station (SER) in the Villa Juan Soldado sector at the outskirts of La Serena, Chile (see Figure 1), is far from urban settlements. For reference, the geographical coordinates of SER are 29.827° S, 71.261° W, at 28 [masl], with corrected geomagnetic coordinates to -16.55 latitude, 0.17 longitude, and L-value of 1.09. SER is supported by the University of La Serena's Laboratory for Space and Atmospheric Physics (LAFESAT) through the Department of Physics of the University of La Serena (DFULS).

SER records geomagnetic field intensity data in nT units using the X (North) Y (East) Z (Down) coordinate system in both ASCII and CDF formats at 1 sec and 1 min time resolution by using a fluxgate magnetometer from the University of California Los Angeles (UCLA). Figure 2 details this instrumentation (Engebretson & Zesta, 2017). Our study applies to five geomagnetic storms observed from 2014 to early 2016. To describe these storms, the geomagnetic Dst index was obtained from Kyoto's World Data Center for Geomagnetism (WDC) database at 1 h resolution (<http://wdc.kugi.kyoto-u.ac.jp/>).

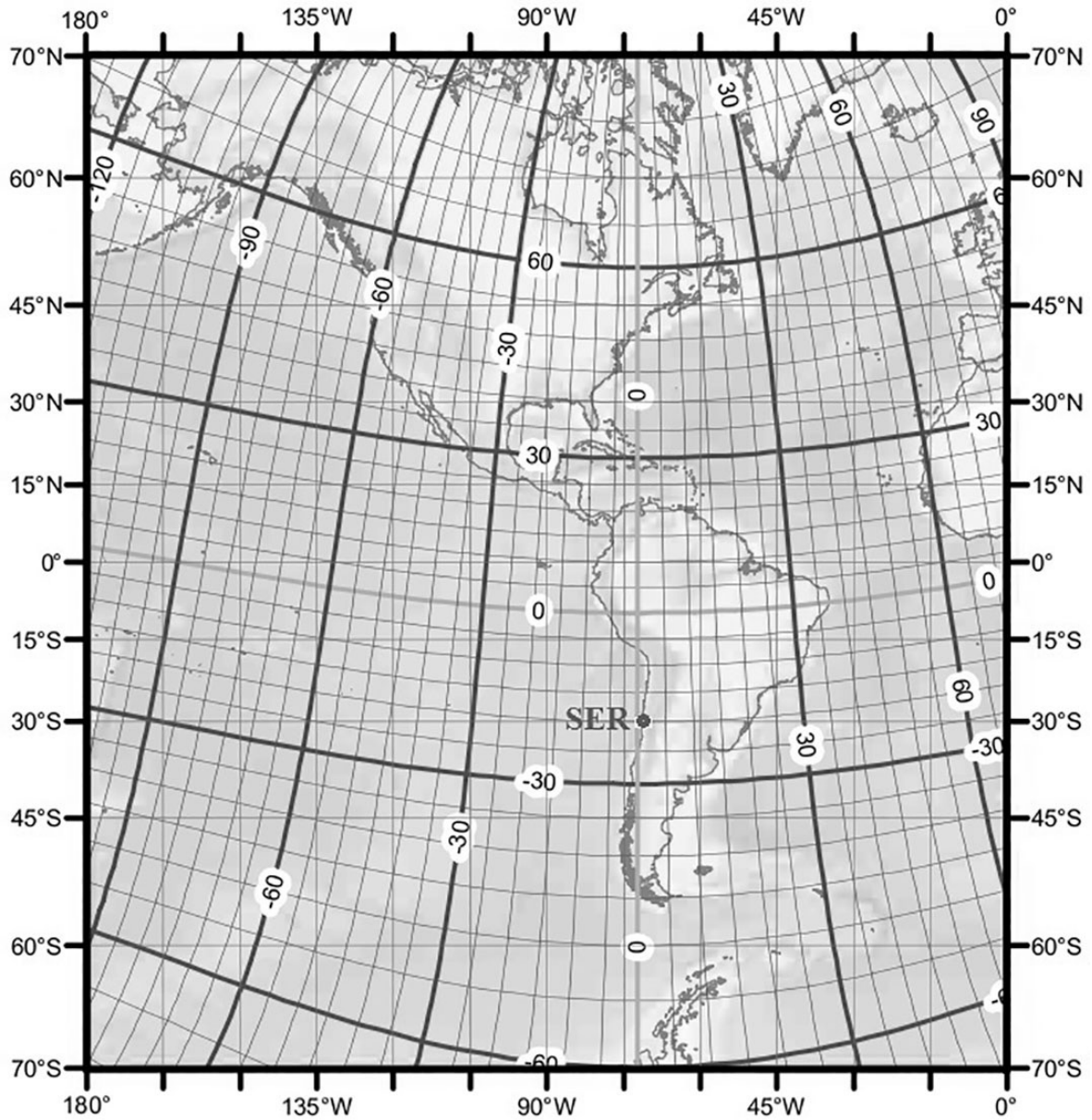


Figure 1. Geographic and magnetic coordinates of SER.

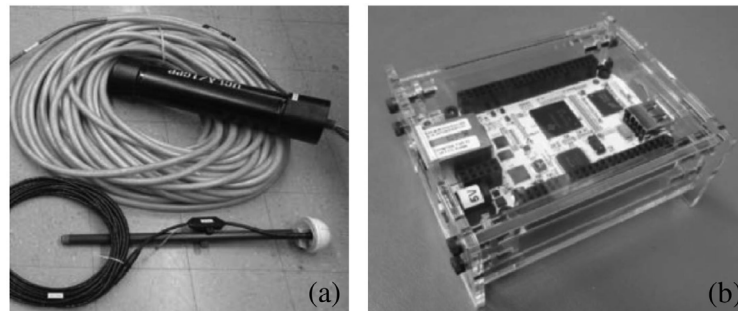


Figure 2. Instruments used by SER. (a) UCLA magnetometer sensor and GPS antenna, and (b) Beaglebone controller/recording system.

Table 1. List of intense geomagnetic storm reported during the maximum phase of solar cycle 24 (in decreasing order).

Code	Start	End	Dst _{min} [nT]	Kp	Type	Solar sources	Reports
I ₁	2015/03/17	2015/03/21	-223	7.7	SC ^a	PH ^c (sheath, MC ^d) CH ^e	(Astafyeva <i>et al.</i> , 2015)
							(Liu <i>et al.</i> , 2015)
							(Baker <i>et al.</i> , 2016)
							(Jacobsen & Andalsvik, 2016)
							(Kalita <i>et al.</i> , 2016)
							(Goldstein <i>et al.</i> , 2016)
							(Hairston <i>et al.</i> , 2016)
							(Nava <i>et al.</i> , 2016)
							(Salinas <i>et al.</i> , 2016)
							(Verkhoglyadova <i>et al.</i> , 2016)
							(Wu <i>et al.</i> , 2016)
							(Yao <i>et al.</i> , 2016)
							(Zakharenkova <i>et al.</i> , 2016)
(Ray <i>et al.</i> , 2017)							
(Watari, 2017)							
(Zolotukhina <i>et al.</i> , 2017)							
I ₂	2015/06/22	2015/06/24	-204	7.7	SC	PH (sheath, MC) multiple	(Liu <i>et al.</i> , 2015)
							(Baker <i>et al.</i> , 2016)
							(Gromova <i>et al.</i> , 2016)
							(Reiff <i>et al.</i> , 2016)
							(Le <i>et al.</i> , 2017)
(Piersanti <i>et al.</i> , 2017)							
(Watari, 2017)							
I ₃	2015/12/19	2015/12/22	-155	6.3	SC	Hf (MC)	(Watari, 2017)
I ₄	2014/02/18	2014/02/22	-119	6.3	GCB	PH (MC) multiple	(Atulkar <i>et al.</i> , 2014)
							(Zakharenkova <i>et al.</i> , 2015)
							(Ghamry <i>et al.</i> , 2016)
							(Durgonics <i>et al.</i> , 2017)
(Watari, 2017)							
I ₅	2015/12/31	2016/01/02	-110	6.0	SC	PH (MC)	(Berdichevsky <i>et al.</i> , 2016)
							(Watari, 2017)

^aSC: sudden commencement; ^bGC: gradual commencement; ^cPH: partial halo CME; ^dMC: magnetic cloud; ^eCH: coronal hole; ^fH: full halo CME.

COMPARISON OF LOCAL MEASUREMENTS AND GLOBAL INDEXES

We investigate five intense geomagnetic storms ($Dst < -100$ nT, $7 \leq Kp \leq 9$) that occurred during the maximum phases of solar cycle 24. Note that the magnetosphere and solar wind parameters (e.g. IMF and plasma parameters) and other solar sources (e.g. CME) of these storms are not studied here. Thus, we select the most intense events registered between 2014 and early 2016 whose characteristics and sources many authors reported (see, Table 1). This Table summarizes the main characteristics of the selected storms.

To describe these events from ground-level measurements, we employ a graphical description based on: (i) the local records of the XYZ-components of the geomagnetic field taken from SER (<http://magnetometers.bc.edu/>) to obtain horizontal component $H = (X^2 + Y^2)^{1/2}$ and the rates dH/dt ; (ii) the geomagnetic Dst index taken from the WDC database (<http://wdc.kugi.kyoto-u.ac.jp/>); and (iii) the Kp index taken from GFZ Helmholtz Centre Potsdam (<https://www.gfz-potsdam.de/>), and

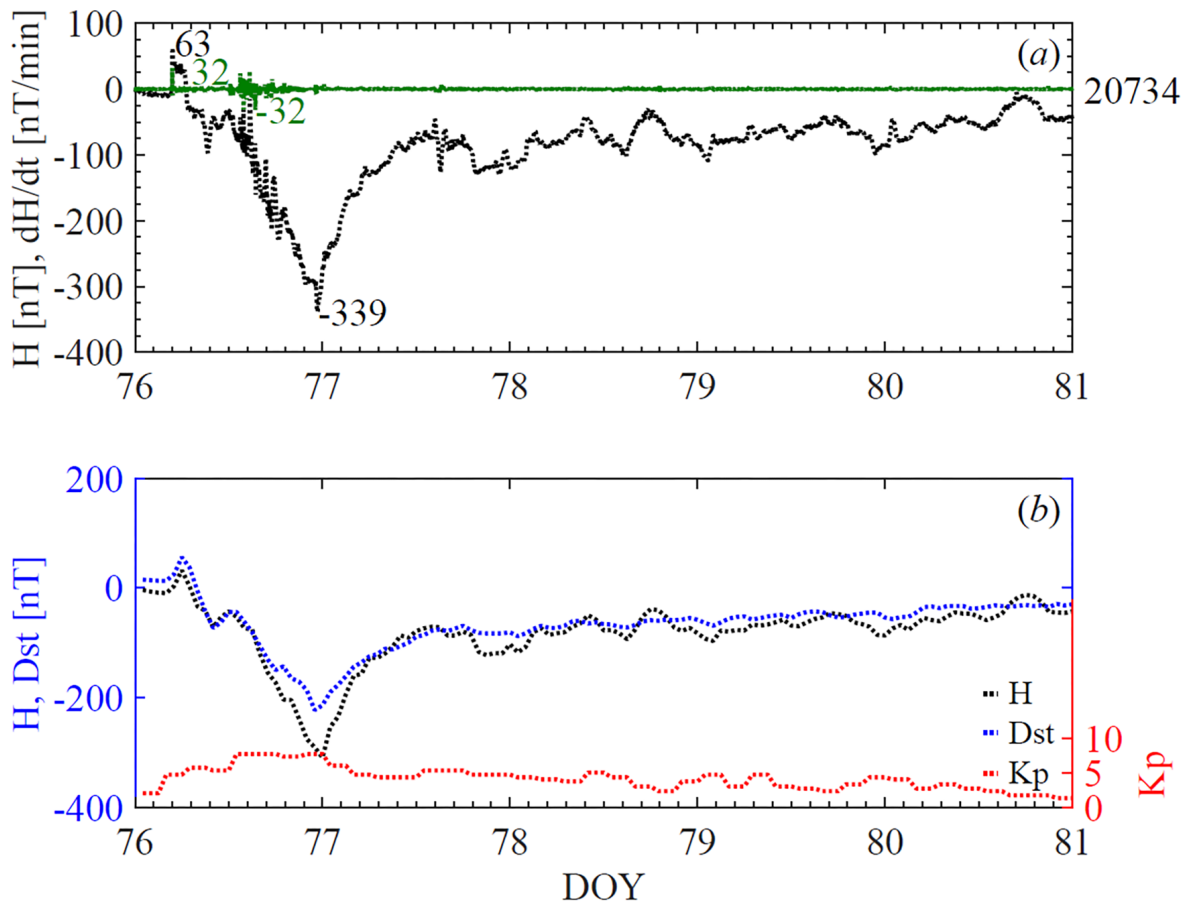


Figure 3. Geomagnetic field variations during the St. Patrick's Day storm (I_1) recorded by SER. (a) H component and rate dH/dt ; (b) comparison of geomagnetic field variations recorded by SER, and the Dst index reported by WDC during this storm. Here, the baseline for the H component was obtained using the method reported by Sugiura & Kamei (1991). The number at the right of the top panel is the reference value obtained by SER. The Kp index in the bottom panel was included to complement the geomagnetic activity due to the storm.

included to complement the geomagnetic activity produced by each storm. In these descriptions, we use universal time (UT) and the day of the year (DOY) to specify the sudden commencement and the phases of each storm.

MARCH 17 (2015) STORM

The March 17–21, 2015 event, called St. Patrick's Day geomagnetic storm, was the most intense storm of solar cycle 24, with a minimum Dst value of -223 nT (Kamide & Kusano, 2015; Wu *et al.*, 2016; Watari, 2017). Figure 3a shows a graphical description of this storm using the H-component of the geomagnetic field recorded by SER at 1 min resolution. Note that in this and the following cases, the baseline for the H component was obtained using the same methodology employed in the derivation of the Dst index (see Sugiura & Kamei, 1991). On March 17 (DOY 76), around 04:45 UT appears the SSC with a 63 nT increase of the H component and a rate $dH/dt=32$ nT/min. Next, the geomagnetic component values fell to a minimum up to $H \sim -200$ nT at 17:00 UT with rates up to $dH/dt=-32$ nT/min. Later, a second storm intensification reached $H=-339$ nT at $\sim 22:00$ UT

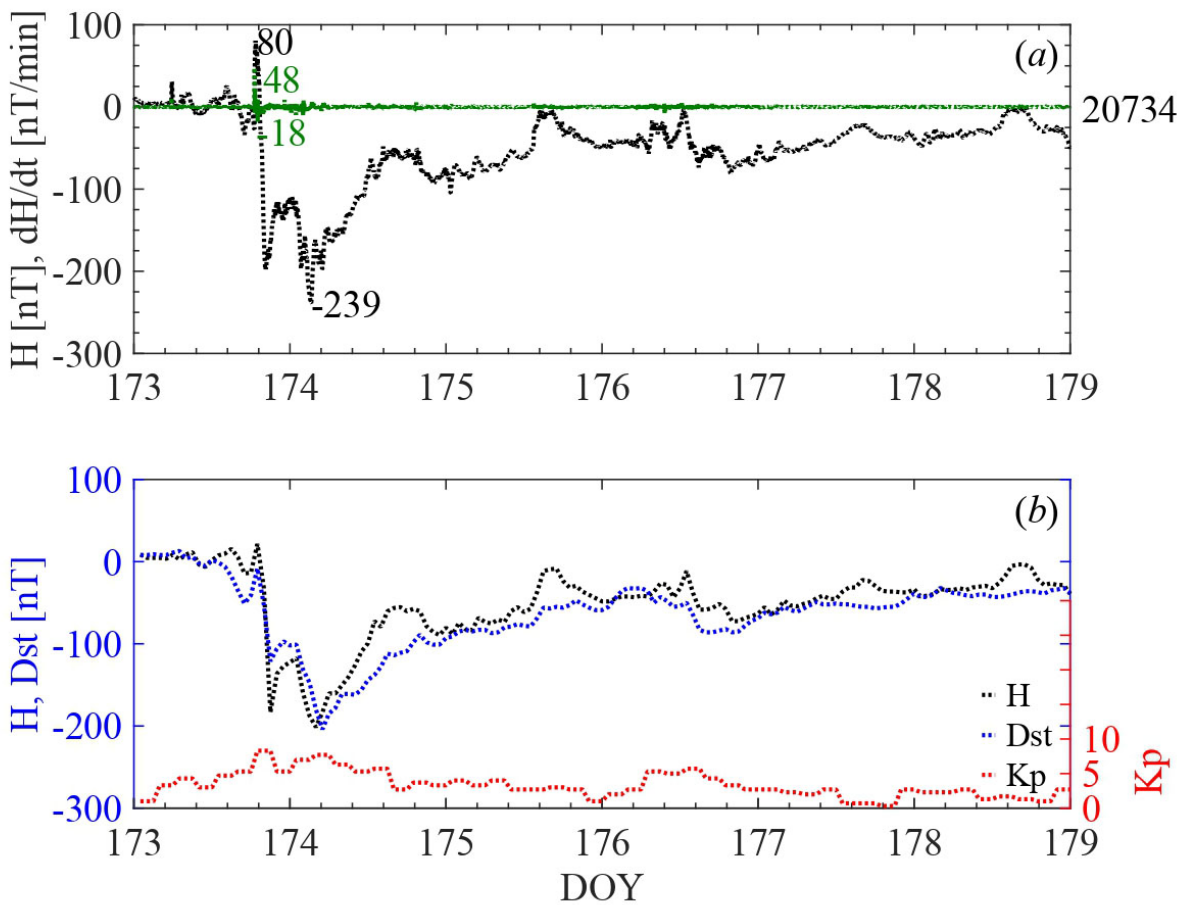


Figure 4. Geomagnetic field variations during the June 22–24, 2015, storm (I2) recorded by SER. The description of this Figure is similar to Fig. 3.

on March 17, and with rates of $dH/dt=10$ nT/min. A few hours later, the geomagnetic component values slowly increased during a recovery phase that lasted several days. Besides, Fig. 3b shows a good correlation between Dst index and the H component for all storms phases.

JUNE 22 (2015) STORM

The geomagnetic storm of June 22–24, 2015, is so far the second most intense event of solar cycle 24 (Le *et al.*, 2017; Piersanti *et al.*, 2017; Watari, 2017). Figure 4 shows its graphical description by using the H-component of the geomagnetic field recorded by SER at 1 min resolution. Fig. 4a displays positive H peak values marking an SSC observed at 06:00 UT on June 22 (DOY 173) with a rate $dH/dt>10$ nT/min. A second SSC was observed around 18:00 UT registering $H=80$ nT and $dH/dt=48$ nT/min. This storm followed a two-step development during its main phase with a first moderate peak at $\sim 20:00$ UT with $H=-190$ nT and $dH/dt=-18$ nT/min; and a second peak of $H=-239$ nT at $\sim 04:00$ UT on June 23 (DOY 174). Next, the recovery phase also unfolded in two-steps observed at $\sim 22:00$ UT on June 23 and at $\sim 14:00$ UT on June 24, both with much rate variation of dH/dt . In addition, Fig. 4b shows the contrast of records of geomagnetic fields measured by

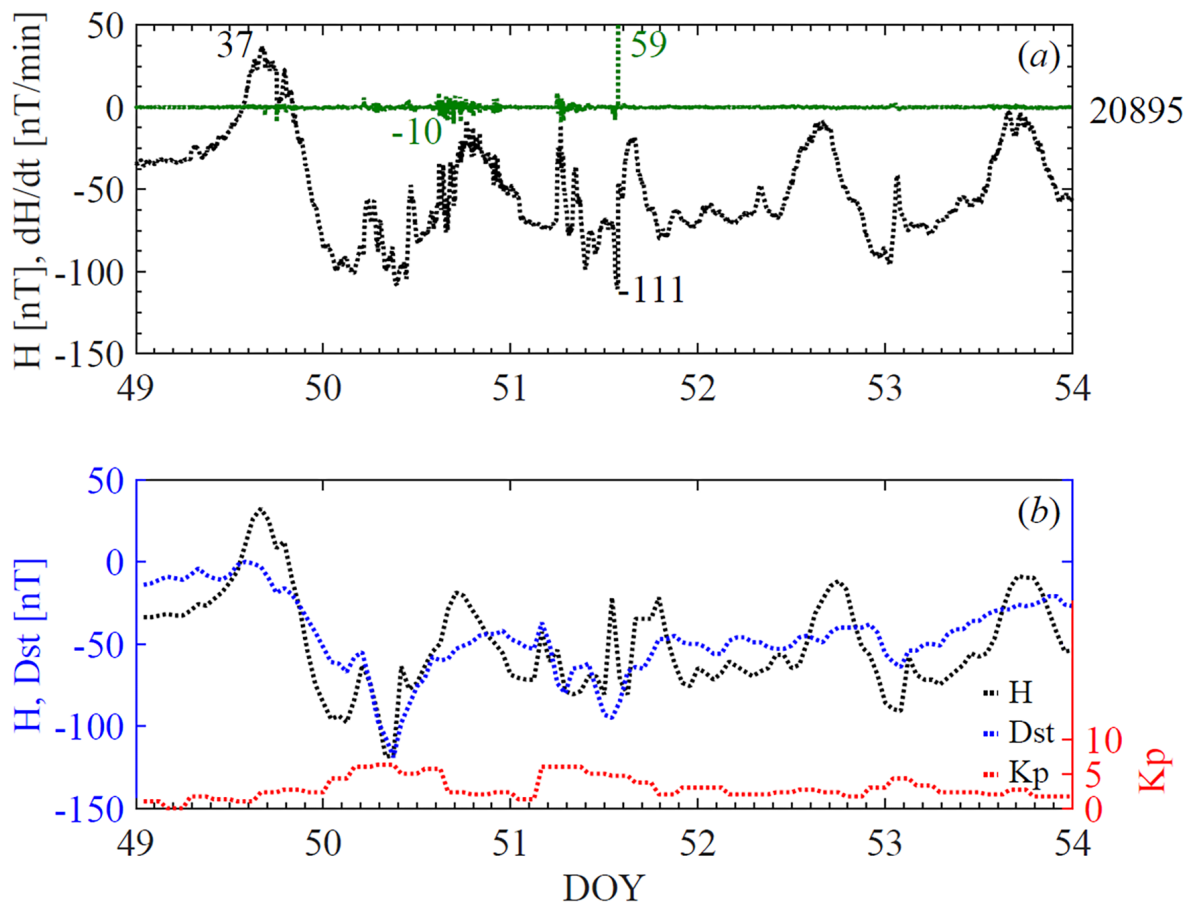


Figure 5. Geomagnetic field variations during the December 19–22, 2015, storm (I3) recorded by SER. The description of this Figure is similar to Fig. 3.

SER and the Dst index reported by WDC. In the Dst data, two minimum value events emerged. One occurred around 05:30 UT on June 23, and the other more powerful event causing a Dst peak of -204 nT on June 24. The storm's main phase lasted about half a day, but its recovery phase took many days. Here, the H component record similar observations as the Dst index.

DECEMBER 19 (2015) STORM

The measured H values by SER (at 1 min resolution) for the December 19–22, 2015, storm and its graphical description appear in Fig. 5a. It shows positive H peak values, corresponding to two SSC at 18:00 UT on December 19 (DOY 353) with $H \approx -110$ nT and $dH/dt = 32$ nT/min; and another at 22:00 UT on December 19 with $H \approx -116$ nT and a rate $dH/dt = 10$ nT/min. Its main phase started during December 20 (DOY 354) and peaked around 22:00 UT that same day, with $H \approx -219$ nT and $dH/dt \approx -12$ nT/min. Then, the geomagnetic component values increased slowly until December 23 (DOY 357). Also, Fig. 5b exhibits the contrast of records between the geomagnetic field measured by SER and the Dst index reported by WDC. Here Dst index shows a minimum of -155 nT at 22:00 UT on December 20 (DOY 254), and similar behavior as H component.

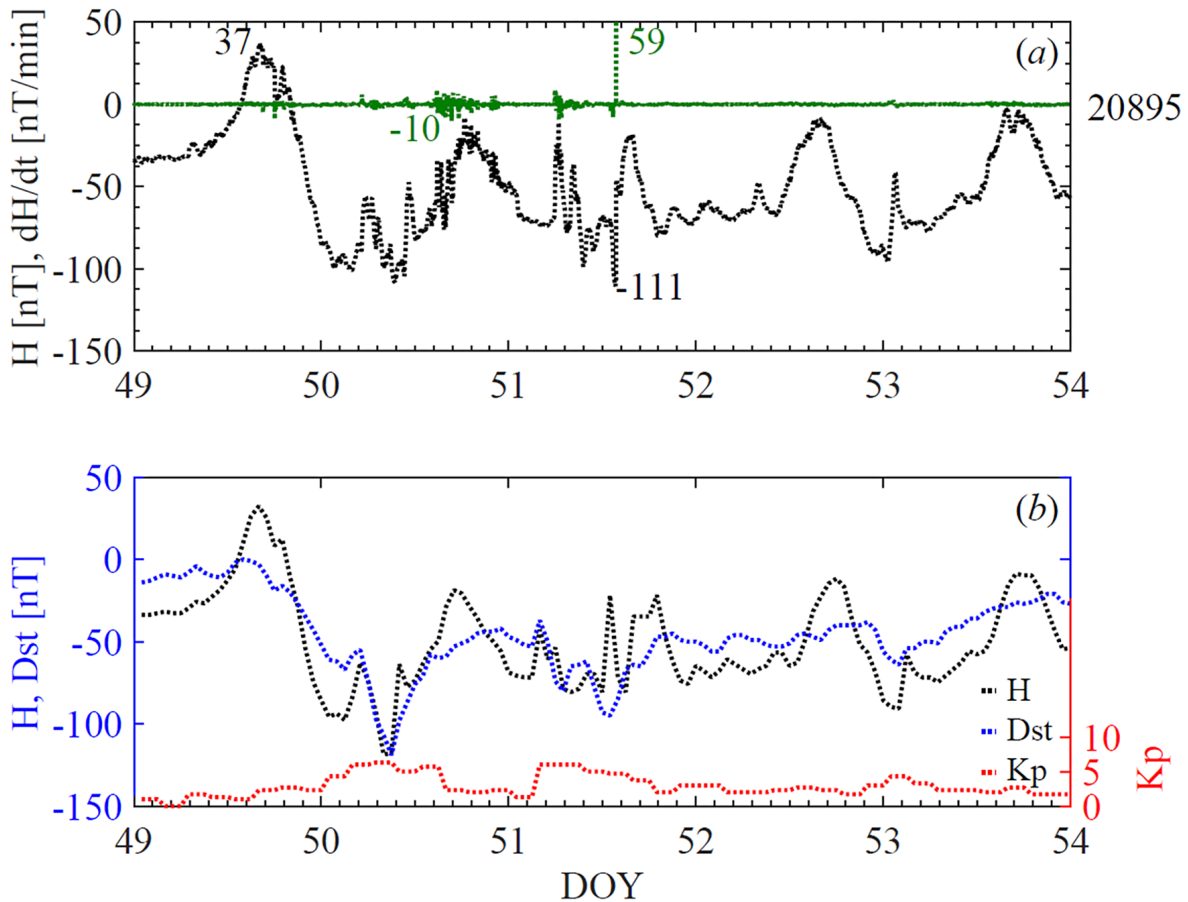


Figure 6. Geomagnetic field variations during the February 18–22, 2014, storm (I4) recorded by SER. The description of this Figure is similar to Fig. 3.

FEBRUARY 18 (2014) STORM

A graphical description of the February 18–22, 2014, storm appears in Figure 6. This Figure details two successive storms that hit the Earth's magnetosphere, recorded by the H component of the geomagnetic field (at 1 min resolution) in SER. Fig. 6a shows the positive values on the H component of the geomagnetic field with amplitude $H=37$ nT at $\sim 14:00$ UT marking the SSC that started the first storm on February 18 (DOY 49). This manifests with a rate $dH/dt \sim 5$ nT/min. The peak of this first event ($H=-109$ nT) was observed at $\sim 09:00$ UT on February 19 (DOY 50) with a rate $dH/dt=6$ nT/min. The second event started $\sim 04:00$ UT on February 20 when this storm's main phase started a two-step development and registered rate $dH/dt=-10$ nT/min. On February 20 (DOY 51), the H component dropped to -111 nT at $\sim 12:30$ UT but recovered rapidly to ~ 25 nT and fell again to -58 nT at $02:00$ UT on February 22. Besides, contrasting these observations with the ones provided for the Dst index from WDC, shows the same behavior as the H component with a minimum $Dst=-119$ nT during the first storm (DOY 50) and another minimum of -95 nT for the second storm on February 20 (DOY 51) as in Fig. 6b.

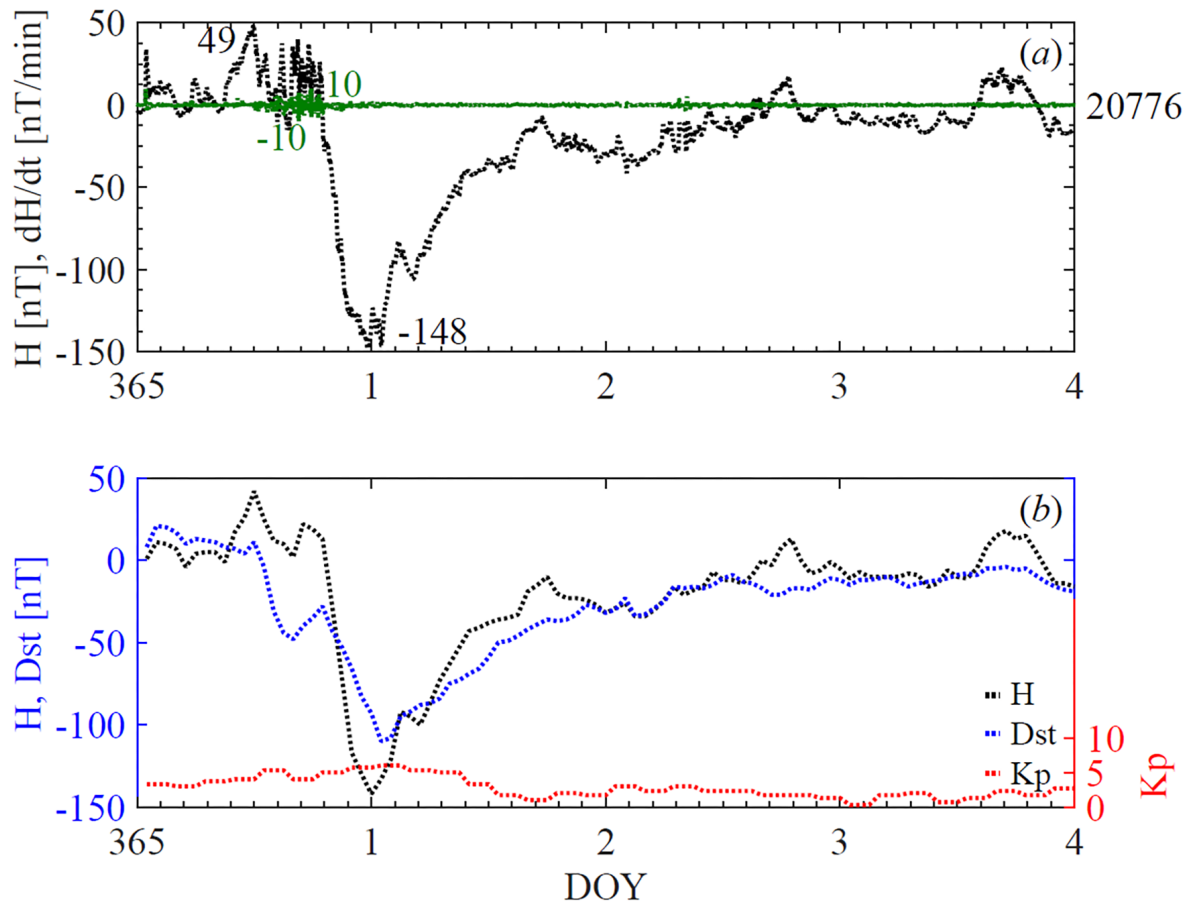


Figure 7. Geomagnetic field variations during the geomagnetic storm on December 12, 2015–January 01, 2016 (15) recorded by SER. The description of this Figure is similar to Fig. 3.

Table 2. Summary of correlation coefficients (R) obtained between Dst index (taken from WDC Kyoto) and H component (recorded by SER) for the phases of each storm studied (columns 3 to 6). In addition, the signs for the difference between their minimum magnitudes, and for its time difference are included in columns 7 and 8, respectively.

Code	Storm	Correlation coefficients between Dst and H				$\Delta = \text{Dst} - \text{H}$	
		R_{initial}	R_{main}	R_{recovery}	R_{storm}	$\Delta_{\text{magnitude}}$	Δ_{time}
I ₁	2015/03/17–2015/03/21	0.970	0.975	0.944	0.951	+	+
I ₂	2015/06/22–2015/06/24	0.957	0.959	0.902	0.902	+	+
I ₃	2015/12/19–2015/12/22	0.838	0.865	0.852	0.855	+	+
I ₄	2014/02/18–2014/02/22	0.917	0.879	0.504	0.717	–	–
I ₅	2015/12/31–2016/01/01	0.808	0.806	0.940	0.860	+	+

DECEMBER 31 (2015) STORM

Figure 7 shows the graphical description of the December 31, 2015–January 02, 2016 storm using the H component of the geomagnetic field recorded by SER at 1 min resolution. In Fig. 7a, successive positive H component values evidence two SSCs measured at ~12:00 UT and ~16:00 UT on December 31 (DOY 365) during the initial phase of this storm. The maximum amplitude of SSC was $H=49$ nT, with a rate $dH/dt \sim 10$ nT/min. The peak of the storm with $H=-148$ nT occurred at ~00:30 UT on January 01, marking the end of its main phase. After this peak, geomagnetic field values increased slowly during its recovery phase. In addition, Fig. 7b shows the H component of the geomagnetic field taken from SER, and the Dst index taken from WDC at 1h resolution. As is observed, a good correlation between Dst index and H component of the geomagnetic field emerges. Here, the SSC peak in the initial phase (DOY 365), and the minimum Dst index value of -110 nT observed at 00:00 UT on January 01 during the main phase are in agreement with those recorded by the H component in SER.

DISCUSSION

The previous section showed that the instrument seems to be working as expected. The SER detected the five geomagnetic storms and showed a good correlation with the Dst index variations reported by WDC. (see Figs. 3 to 7). In terms of H component, the records obtained by SER can characterize all storm phases, such as the higher H values in the initial phase, followed by the dropped ones of the H component during the main phase, and its restitution to normal levels in the recovery phase. Also, the SSC signatures were evidenced with the rates dH/dt , because they are powerful indicators of disturbances in the ring current (Doumbia *et al.*, 2017).

Table 2 shows the correlation coefficient (R) between the hourly Dst index and the geomagnetic field H-component (at 1h resolution) obtained for each storm analyzed (see columns 3 to 6). For total storm disturbance R_{storm} , only storm I₄ shows $R_{\text{storm}} < 0.8$ while all others show R_{storm} from 0.85 to 0.96. When analyzing the R values for the different storm phases, both the initial and main phases present R_{initial} and R_{main} from 0.8 to 0.97, while the recovery phase shows R_{recovery} from 0.5 to 0.94 being the lowest value for storm I₄. In general, the measurements of the H component of the geomagnetic field recorded by SER show minor discrepancies with the storm behavior described by

the Dst index. Note that the Dst index is an average obtained from different stations. The behavior of individual stations is expected to vary with respect to global value, and the local site response is the important one for each region, but also this discrepancy can be associated with phenomena that contribute to the H component variation, such as (1) the magnetopause current, (2) the symmetric ring current, (3) the cross-tail current, and (4) the partial ring current (Maltsev, 2004). To distinguish the action of these magnetospheric currents on the selected storms, we have represented the time at which the minimum Dst value occurs for each storm. Figure 8 shows the graphical representation of the instant of the minimum Dst at UT and magnetic local time (MLT). In this Figure, the Earth is represented from the North Pole as follows: day side-night side, and dawn-dusk sectors, with the UT represented by the inner circle and the MLT by the outer one. To clarify, the MLT in SER at UT noon is 16:00 MLT. As is observed, storms I_1 and I_3 measured the maximum depression of the H component at 18:00 MLT (but on different dates), and as both have an SSC, they developed the initial and main phases in the dusk zone. In the zone between dusk and midnight, storms I_2 and I_5 (at 20:00 and 00:00 MLT, respectively) developed both their initial and main phases, and a few hours

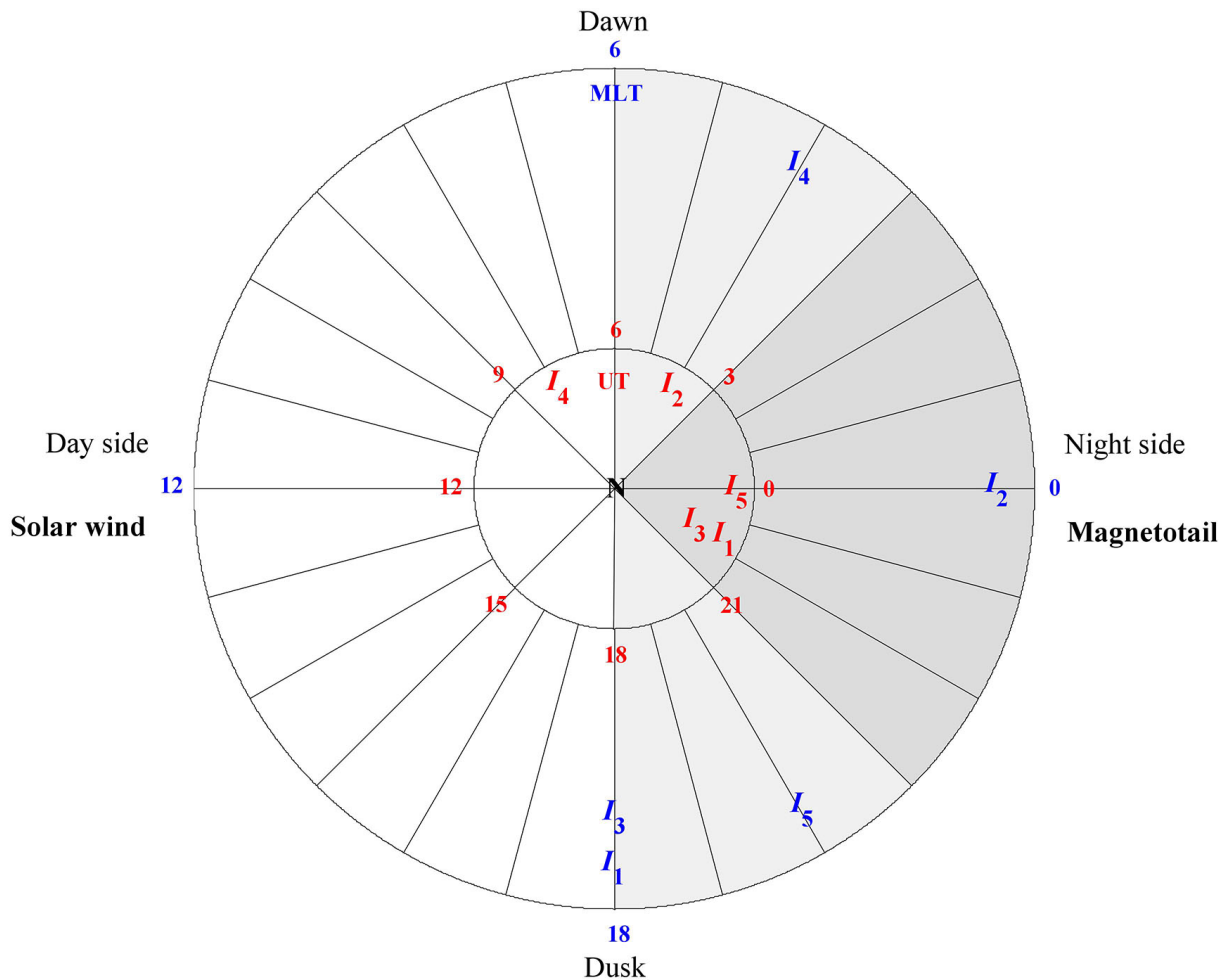


Figure 8. Location of geomagnetic storms studied at the time of their occurrence as a graphical representation of the maximum depression of H component (or the minimum Dst) at UT (the inner circle) and MLT (outer circle). Here, grey sectors represent the night side and white sectors the dayside. Regions of currents are the magnetotail electrojet on the night side, the dawn, the dusk, and the dayside.

later their recovery phase went toward the day side. Storm I_4 developed the initial and main phases in the midnight-dawn zone at 04:00 MLT, and its recovery phase also began more on the day side. Contrasting the analyses in Table 2 and Figure 8, we notice that the observations recorded by SER agree with Li *et al.*, 2011, who researched the distribution of the H depressions with magnetic local times (MLT). They proposed that in the ring current injection that occurs during a geomagnetic storm, the particles are mostly present between dusk and midnight sectors, with drifting toward dusk, and producing a highly asymmetric geomagnetic disturbance with MLT. Then, for the storms analyzed, the partial ring current in the dusk sector is the predominant contributor to the depressions of the H component during the main phase, as the higher R values between the Dst index and H component prove during the initial and main phases of storms I_1 , I_2 , I_3 , and I_5 . Weak H variations affected storm I_4 in the dawn sector, so the storm obtains lower R values during the initial and main phases. For the recovery phase, the dawn-dusk asymmetry of the H component weakens gradually until it disappears when values return to normal.

Besides, to distinguish the action of the ionospheric currents on the selected storms, we have calculated the difference between the minimum magnitudes of Dst index (taken from WDC) and H component in SER, and the time difference at which this minimum magnitude occurs (see Table 2, columns 7 and 8, respectively). Thus, a negative (positive) $\Delta_{\text{magnitude}}$ indicates that the minimum magnitude is a little higher in SER than in the Dst index (or it is greater in the Dst than SER); and a negative (positive) Δ_{time} means that the minimum magnitude appears first in SER and afterward in the Dst index (or first in the Dst index than SER). As is shown, the storms I_1 , I_2 , I_3 , and I_5 (located from dusk till pre-dawn sectors in the night side) exhibit positive values for both differences, so they occur earlier and with greater intensity in SER than in the Dst. These results show that during the ring current injection of these storms, the ions were mostly present in the dusk and pre-midnight sectors (see examples in Li *et al.* 2011). In addition, these storms were located near the magnetotail

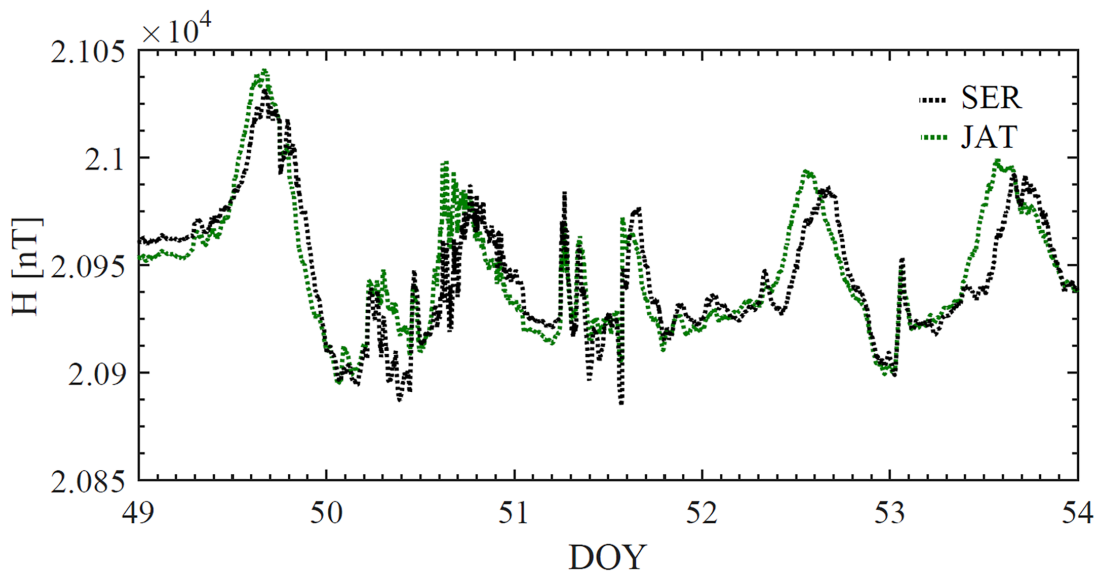


Figure 9. Comparison between the H component data recorded by SER and JAT stations (with geomagnetic latitudes of -16.55° and -12.3° , respectively) during the February 18–22, 2014, storm (I_4). JAT station is located in Brazil (17.9°S , 51.7°W) and is part of the EMBRACE array.

zone just when the electrojet was injected directly into the ring current (see examples in Martínez-Bretón *et al.*, 2016). However, only I_4 (located in the dawn sector) presents negative values in both differences so it happens earlier and with greater intensity in the Dst than SER. This fact can be influenced by a dawn current just in the transition to dayside (Martínez-Bretón *et al.*, 2016), and by the equatorial electrojet, which is very strong during the daytime (Kalegaev *et al.*, 2008). As storm I_4 shows low correlation coefficients (relative to the Dst index), we compare our data with the data recorded by Jataí station JAT, in Brazil, from EMBRACE array (Denardini *et al.*, 2018) to discard any malfunction of our instruments (see Figure 9). This analysis show correlation coefficient values of $R > 0.9$ for all phases of the storm. Note that a similar comparison was made for all storms studied, and for all cases, the correlation coefficient values were more than 0.9. In general, all our data and results are consistent with the strong influence of the magnetospheric/ionospheric current systems over the H component during an intense geomagnetic storm.

On the other hand, Häkkinen *et al.* (2003) investigated the daily and seasonal variability of the H component using time series of magnetometer data taken from official Dst stations. They demonstrated that only ~50% of this variability can be explained by three external drivers of geomagnetic activity, such as the heliographic latitude, the equinoctial effect, and the Russell–McPherron effect. Therefore, they suggested that the other 50% of the daily and seasonal variability could be explained by the distribution of the hemispheric stations. Note that the distribution is key because the hemispheric asymmetry of the geomagnetic field (that is mainly evidenced for the field minimization at the South Atlantic Magnetic Anomaly) can cause N-S amplitude differences without a specific annual pattern and randomly distributed over time (Pinto *et al.*, 1992). Thus, both the installation and management of southern magnetic ground stations such as SER according to modern standards are crucial for monitoring magnetospheric disturbances and other related phenomena.

Also, it should be noted that this work aims to show the measurements of a new geomagnetic station in the South American region and to compare their signatures concerning the global Dst index. However, it must be remembered that each local magnetic signature is unique, and the global index is obtained from the average of some of these. Saiz *et al.* (2021) showed that is possible to miss hazardous space weather disturbances using the global Dst index, and that large negative H peak recorded at any geomagnetic station might disappear in the average of the H-component from the global index observatories. Also, they proposed that the assessment of extreme events should be based on local records instead of the commonly used global indices. For this, the operation of new magnetometers for the South American region is good news to have better regional coverage of space weather events and to understand the particular characteristics of the Chilean region.

Finally, we declare that the geomagnetic field data SER recorded are consistent with the Dst index variations reported, and were obtained according to modern standards for magnetic stations. The University of La Serena's Laboratory for Space and Atmospheric Physics (LAFESAT) has developed quality infrastructure that guarantees SER's correct operation. For interested researchers, SER has recorded geomagnetic field data uninterrupted from late 2013 to now, which are available on the SAMBA website (<http://magnetometers.bc.edu/>). SER constitutes a new in situ tool of a low-latitude ground-based station that can contribute to magnetospheric research.

CONCLUSIONS

We studied five intense geomagnetic storms during the maximum phase of solar cycle 24 by using ground-level magnetic field data reported by the La Serena low-latitude magnetic ground station.

Based on the results and discussions in this study, these main conclusions obtain: (i) Due to the complexities of magnetospheric research, the installation and management of new magnetic ground stations according to modern standards is crucial. In response to development of new in situ tools and ground-based data sets that facilitate these studies, the records generated by the La Serena low-latitude magnetic ground station to describe magnetospheric disturbances and other related phenomena are available; (ii) Results evidence that H component variations measured by the La Serena station are consistent with the Dst index variations reported for each storm analyzed, obtaining correlation coefficient values of up to 0.97 for storms with $Dst < -200$ nT; (iii) The partial ring current in the dusk and night side sectors are the predominant contributor to the depressions of the H component during the main phase of the storms analyzed; (iv) Geomagnetic field values recorded by the La Serena station are useful in studies related to geomagnetic activity and reliable because the University of La Serena's Laboratory for Space and Atmospheric Physics (LAFESAT) has developed quality infrastructure that guarantees correct operation.

ACKNOWLEDGMENTS

The authors thank the support of the Direction of Research and Development of the University of La Serena (DIDULS) through projects PR22135 and PR18141, and the University of La Serena's Laboratory for Space and Atmospheric Physics (LAFESAT) by the instrumental support that enabled the preparation of this paper. Special thanks go to E. Yizengaw, E. Zesta, M. B. Moldwin and the rest of the AMBER and SAMBA team for the data.

REFERENCES

- Agee E.M., Cornett E., Gleason K., 2010, An extended solar cycle 23 with deep minimum transition to cycle 24: assessments and climatic ramifications, *J. Clim.*, 23, 6110–6114.
- Anderson D., Anghel A., Chau J., Veliz O., 2004, Daytime vertical $E \times B$ drift velocities inferred from ground-based magnetometer observations at low latitudes, *Space Weather*, 2, S11001(1)–S11001(9).
- Astafyeva E., Zakharenkova I., Förster M., 2015, Ionospheric response to the 2015 St. Patrick's Day storm: A global multi-instrumental overview, *J. Geophys. Res. Space Phys.*, 120, 9023–9037.
- Atulkar R., Bhardwaj S., Khatarkar P., Bhawre P., Purohit P.K., 2014, Geomagnetic disturbances and its impact on ionospheric critical frequency (f_oF_2) at high, mid and low latitude región, *Am. J. Astron. Astrophys.*, 2, 61–65.
- Baker D.N., Jaynes A.N., Kanekal S.G., Foster J.C., Erickson P.J., Fennell J.F., Blake J.B., Zhao H., Li X., Elkington S.R., Henderson M.G., Reeves G.D., Spence H.E., Kletzing C.A., Wygant J.R., 2016, Highly relativistic radiation belt electron acceleration, transport, and loss: Large solar storm events of March and June 2015, *J. Geophys. Res. Space Phys.*, 121, 6647–6660.
- Bartels J., 1949, The standardized index, K_s , and the planetary index, K_p . *IATME Bull.*, 12b, 97–120.
- Berdichevsky D.B., Richardson I.G., Farrugia J.C., 2016, Comparative study of the December 28, 2015–January 2, 2016 and April 7–11, 1997 Sun-Earth connection events, in: 2016 AGU Fall General Assembly, id. SH13B-2300, AGU, San Francisco, CA, USA.
- Bogdanova Y., Dunlop M., Zhang Q., Perry C., Shen C., 2014, Ring Current Morphology and Properties: Statistic from Cluster, *Geophysical Research Abstracts*, 16, EGU2014-6591.

- Chen P.F., 2011, Coronal mass ejections: models and their observational basis, *Living Rev. Solar Phys.*, 8, 1–92.
- Daglis I.A., Thorne R.M., Baumjohann W., Orsini S., 1999, The Terrestrial Ring Current: Origin, Formation, and Decay, *Rev. Geophys.*, 37, 407–438.
- Denardini C.M., Chen S.S., Resende L.C.A., Moro J., Bilibio A.V., Fagundes P.R., Gende M.A., Cabrera M.A., Bolzan M.J.A., Padilha A.L., Schuch N.J., Hormaechea J.L., Alves L.R., Barbosa Neto P.F., Nogueira P.A.B., Picanço G.A.S., Bertolotto T.O., 2018, The Embrace Magnetometer Network for South America: Network description and its qualification, *Radio Sci.*, 53, 288–302.
- Doumbia V., Boka K., Kouassi N., Grodji O.D.F., Amory-Mazaudier C., Menvielle M., 2017, Induction effects of geomagnetic disturbances in the geo-electric field variations at low latitudes, *Ann. Geophys.*, 35, 39–51.
- Durgonics T., Komjathy A., Verkhoglyadova O., Shume E.B., Benzoni H.H., Mannucci A.J., Butala M.D., Høeg P., Langley R.B., 2017, Multiinstrument observations of a geomagnetic storm and its effects on the Arctic ionosphere: a case study of the 19 February 2014 storm, *Radio Sci.*, 52, 146–165.
- Eddy J.A., 1976, The Maunder minimum, *Science*, 192, 1189–1202.
- Engebretson M., Zesta E., 2017, Ground Magnetometer Array Planning: Report of a Workshop, Augsburg College, Minneapolis, MN, USA.
- Feynman J., Ruzmaikin A., 2011, The Sun's strange behavior: Maunder minimum or Gleissberg cycle?, *Sol. Phys.*, 272, 351–363.
- Ganushkina N.Y., Liemohn M.W., Dubyagin S., 2018, Current systems in the Earth's magnetosphere, *Rev. Geophys.*, 56, 309–332.
- Ghamry E., Lethy A., Arafa-Hamed T., Elaal E.A., 2016, A comprehensive analysis of the geomagnetic storms occurred during 18 February and 2 March 2014, *NRIAG J. Astron. Geophys.*, 5, 263–268.
- Goldstein J., Angelopoulos V., De Pascuale S., Funsten H.O., Kurth W.S., LLera K., McComas D.J., Perez J.D., Reeves, G.D., Spence H.E., Thaller S.A., Valek P.W., Wygant J.R., 2016, Cross-scale observations of the 2015 St. Patrick's Day storm: THEMIS, Van Allen Probes, and TWINS, *J. Geophys. Res. Space Phys.*, 121, 368–392.
- Gonzalez W.D., Joselyn J.A., Kamide Y., Kroehl H.W., Rostoker G., Tsurutani B.T., Vasyliunas V.M., 1994, What is a geomagnetic storm?, *J. Geophys. Res.*, 99, 5771–5792.
- Gopalswamy N., Xie H., Akiyama S., Makela P.A., Yashiro S., 2014, Major solar eruptions and high-energy particle events during solar cycle 24, *Earth Planet Space*, 66, 104(1)–104(15).
- Gopalswamy N., Yashiro S., Michalek G., Xie H., Lepping R.P., Howard R.A., 2005, Solar source of the largest geomagnetic storm of cycle 23, *Geophys. Res. Lett.*, 32, L12S09(1)–L12S09(5).
- Gosling J.T., McComas D.J., Phillips J.L., Bame S.J., 1991, Geomagnetic activity associated with earth passage of interplanetary shock disturbances and coronal mass ejections, *J. Geophys. Res.*, 96, 7831–7839.
- Gromova L.I., Kleimenova N.G., Levitin A.E., Gromov S.V., Dremukhina L.A., Zelinskii, N.R., 2016, Daytime geomagnetic disturbances at high latitudes during a strong magnetic storm of June 21–23, 2015: the storm initial phase, *Geomagn. Aeron.*, 56, 281–292.
- Hairston M., Coley W.R., Stoneback R., 2016, Responses in the polar and equatorial ionosphere to the March 2015 St. Patrick Day storm, *J. Geophys. Res. Space Phys.*, 121, 11213–11234.
- Hao J., Zhang M., 2011, Hemispheric helicity trend for solar cycle 24, *Astrophys. J. Lett.*, 733, L27(1)–L27(6).
- Hapgood M.A., 2011, Towards a scientific understanding of the risk from extreme space weather, *Adv. Space Res.*, 47, 2059–2072.
- Häkkinen L.V.T., Pulkkinen T.I., Pirjola R.J., Nevanlinna H., Tanskanen E.I., Turner N.E., 2003, Seasonal and diurnal variation of geomagnetic activity: revised Dst versus external drivers, *J. Geophys. Res. Space Phys.*, 108, 1060.
- Jacobsen K.S., Andalsvik Y.L., 2016, Overview of the 2015 St. Patrick's day storm and its consequences for RTK and PPP positioning in Norway, *J. Space Weather Space Clim.*, 6, A9(1)–A9(12).

- Joshi N.C., Bankoti N.S., Pande S., Pande B., Pandey K., 2011, Relationship between interplanetary field/plasma parameters with geomagnetic indices and their behavior during intense geomagnetic storms, *New Astron.*, 16, 366–385.
- Kalegaev V., Makarenkov E., 2008, Relative importance of ring and tail currents to Dst under extremely disturbed conditions, *J. Atmos. Sol.-Terr. Phys.*, 70, 519–525.
- Kalegaev V.V., Bakhmina K.Y., Alexeev I.I., Belenkaya E.S., Feldstein Y.I., Ganuskina N.V., 2008, Ring Current Asymmetry during a Magnetic Storm, *Geomagn. Aeron.*, 48, 6, 747–758.
- Kalita B.R., Hazarika R., Kakoti G., Bhuyan P.K., Chakrabarty D., Seemala G.K., Wang K., Sharma S., Yokoyama T., Supnithi P., Komolmis T., Yatini C.Y., Le Huy M., Roy P., 2016, Conjugate hemisphere ionospheric response to the St. Patrick's Day storms of 2013 and 2015 in the 100°E longitude sector, *J. Geophys. Res. Space Phys.*, 121, 1–27.
- Kamide Y., Kusano K., 2013, Is something wrong with the present solar maximum?, *Space Weather*, 11, 140–1411.
- Kamide Y., Kusano K., 2015, No major solar flares but the largest geomagnetic storm in the present solar cycle, *Space Weather*, 13, 365–367.
- Kamide Y., Richmond A.D., Matsushita S., 1981, Estimation of ionospheric electric fields, ionospheric currents, and field-aligned currents from ground magnetic records, *J. Geophys. Res.*, 86, 801–813.
- Keika K.L., Kistler L.M., Brandt P.C., 2013, Energization of O⁺ ions in the Earth's inner magnetosphere and the effects on ring current buildup: A review of previous observations and possible mechanisms, *J. Geophys. Res. Space Phys.*, 118, 7, 4441–4464.
- Le G., 2013, Magnetic Field Observations of the Ring Current in the inner Magnetosphere and Ionosphere. American Geophysical Union, Spring Meeting, abstract SM33A-01.
- Le G., Chi P.J., Strangeway R.J., Russell C.T., Slavin J.A., Takahashi K., Singer H.J., Anderson B.J., Bromund K., Fischer D., Kepko E.L., Magnes W., Nakamura R., Plaschke F., Torbert R.B., 2017, Global observations of magnetospheric high-m poloidal waves during the 22 June 2015 magnetic storm, *Geophys. Res. Lett.*, 44, 3456–3464.
- Li H., Wang C., Kan J.R., 2011, Contribution of the partial ring current to the SYMH index during magnetic storms, *J. Geophys. Res.*, 116, A11222(1)–A11222(12).
- Lingri D., Mavromichalaki H., Belov A., Eroshenko E., Yanke V., Abunin A., Abunina M., 2016, Solar activity parameters and associated Forbush decreases during the minimum between cycles 23 and 24 and the ascending phase of cycle 24, *Solar Phys.*, 291, 1025–1041.
- Liu Y.D., Hu H., Wang R., Yang Z., Zhu B., Liu Y.A., Luhmann J.G., Richardson J.D., 2015, Plasma and magnetic field characteristics of solar coronal mass ejections in relation to geomagnetic storm intensity and variability, *Astrophys. J. Lett.*, 809, L34(1)–L34(6).
- Loewe C.A., Pröls G.W., 1997, Classification and mean behavior of magnetic storms, *J. Geophys. Res.*, 102, 14209–14213.
- Love J.J., 2008, Magnetic monitoring of earth and space, *Phys. Today*, 61, 31–37.
- Love J.J., Chulliat A., 2013, An international network of magnetic observatories, *Eos Trans. AGU*, 94, 373–384.
- Love J.J., Finn C.A., 2011, The USGS Geomagnetism Program and its role in space weather monitoring, *Space Weather*, 9, S07001(1)–S07001(5).
- Love J.J., Rigler E.J., Pulkkinen A., Balch C.C., 2014, Magnetic storms and induction hazards, *Eos Trans. AGU*, 95, 445–446.
- Maltsev Y., 2004, Points of controversy in the study of magnetic storms, *Space Sci. Rev.*, 110, 227–267.
- Mandea M., Korte M., 2011, *Geomagnetic Observations and Models*, Springer, The Netherlands.
- Martínez-Bretón J.L., Mendoza Ortega B., Hernández-Quintero E., 2016, Relationship between the minima of the horizontal magnetic component measured in Mexico and the Dst and SYM-H indices for geomagnetic storms with Dst ≤ -100nT during the descending phase of solar cycle 23, *Geofis. Int.*, 55, 155–164.

- Matzka J., Chulliat A., Mandea M., Finlay C., Qamili E., 2010, Geomagnetic observations for main field studies: from ground to space, *Space Sci. Rev.*, 155, 29–64.
- Matzka J., Stolle C., Yamazaki Y., Bronkalla O., Morschhauser A., 2021, The geomagnetic Kp index and derived indices of geomagnetic activity, *Space Weather*, 19, e2020SW002641.
- Mauquoy D., Geel B., Blaauw M., Plicht J., 2002, Evidence from north-west European bogs shows ‘Little Ice Age’ climatic changes driven by variations in solar activity, *The Holocene*, 12, 1–6.
- McDonald F.B., Webber W.R., Reames D.V., 2010, Unusual time histories of galactic and anomalous cosmic rays at 1 AU over the deep solar minimum of cycle 23/24, *Geophys. Res. Lett.*, 37, L18101(1)–L18101(5).
- Nava B., Rodríguez-Zuluaga J., Alazo-Cuartas K., Kashcheyev A., Migoya-Orué Y., Radicella S. M., Amory-Mazaudier C., Fleury R., 2016, Middle- and low-latitude ionosphere response to 2015 St. Patrick’s Day geomagnetic storm, *J. Geophys. Res. Space Phys.*, 121, 3421–3438.
- Onsager T.G., 2012, Advancing space weather services through international coordination, *Space Weather*, 10, S04004(1)–S04004(4).
- Owens M.J., Lockwood M., Hawkins E., Usoskin I., Jones G.S., Barnard L., Schurer A., Fasullo J., 2017, The Maunder minimum and the Little Ice Age: an update from recent reconstructions and climate simulations, *J. Space Weather Space Clim.*, 7, A33(1)–A33(10).
- Pesnell W., 2014, Predicting solar cycle 24 using a geomagnetic precursor pair, *Sol. Phys.*, 289, 2317–2331.
- Piersanti M., Alberti T., Bemporad A., Berrilli F., Bruno R., Capparell V., Carbone V., Cesaroni C., Consolini G., Cristaldi A., Del Corpo A., Del Moro D., Di Matteo S., Ermolli I., Fineschi S., Giannattasio E., Giorgi F., Giovannelli L., Guglielmino S.L., Laurenza M., Lepreti F., Marcucci M.F., Martucci M., Mergè M., Pezzopane M., Pietropaolo E., Romano P., Sparvoli R., Spogli L., Stangalini M., Vecchio A., Vellante M., Villante U., Zuccarello F., Heilig B., Reda J., Lichtenberger J., 2017, Comprehensive analysis of the geoeffective solar event of 21 June 2015: effects on the magnetosphere, plasmasphere, and ionosphere systems, *Solar Phys.*, 292, 169(1)–169(56).
- Pinto O., Gonzalez W.D., Pinto I.R.C.A., Gonzalez A.L.C., Mendes O., 1992, The South Atlantic Magnetic Anomaly: three decades of research, *J. Atmos. Sol. Terr. Phys.*, 54, 1129–1134.
- Ray S., Roy B., Paul K.S., Goswami S., Oikonomou C., Haralambous H., Chandel B., Paul A., 2017, Study of the effect of March 17-18, 2015 geomagnetic storm on the Indian longitudes using GPS and C/NOFS, *J. Geophys. Res. Space Phys.*, 122, 2551–2563.
- Reiff P.H., Daou A.G., Sazykin S.Y., Nakamura R., Hairston M.R., Coffey V., Chandler M.O., Anderson B.J., Russell C.T., Welling D., Fuselier S.A., Genestreti K.J., 2016, Multispacecraft observations and modeling of the 22/23 June 2015 geomagnetic storm, *Geophys. Res. Lett.*, 43, 7311–7318.
- Richardson I.G., 2013, Geomagnetic activity during the rising phase of solar cycle 24, *J. Space Weather Space Clim.*, 3, A08(1)–A08(11).
- Richmond A.D., Kamide Y., 1988, Mapping electrodynamic features of the high-latitude ionosphere from localized observations: technique, *J. Geophys. Res.*, 93, 5741–5759.
- Russell C.T., Luhmann J.G., Jian L.K., 2010, How unprecedented a solar minimum?, *Rev. Geophys.*, 48, RG2004(1)–RG2004(16).
- Sainz E., Cid C., Guerreo A., 2021, The relevance of local magnetic records when using extreme space weather events as benchmarks, *J. Space Weather Space Clim.*, 11, 35(1)–35(21).
- Salinas A., Toledo-Redondo S., Navarro E.A., Fornieles-Callejón J., Portí J.A., 2016, Solar storm effects during Saint Patrick’s Days in 2013 and 2015 on the Schumann resonances measured by the ELF station at Sierra Nevada (Spain), *J. Geophys. Res. Space Phys.*, 121, 12234–12246.
- Schwabe H., 1844, Sonnen-Beobachtungen im Jahre 1843, *Astron. Nachr.*, 21, 233–236.
- Sugiura M., 1964, Hourly values of equatorial Dst for the IGY, *Ann. Int. Geophys. Year*, 35, 9–45.

- Sugiura M., Kamei T., 1991, Equatorial DST Index 1957–1986, In: Berthelier A. and Menvielle M. (Eds.), *AGA Bull. 40, Int. Serv. Geomagn. Indices Publ Off.*, Saint-Maur-des-Fosses, France.
- Tsurutani B.T., Gonzalez W.D., Tang F., Akasofu S.I., Smith E.J., 1988, Origin of interplanetary southward magnetic fields responsible for major magnetic storms near solar maximum (1978–1979), *J. Geophys. Res.*, 93, 8519–8531.
- Tsurutani B.T., Verkhoglyadova O.P., Mannucci A.J., Lakhina G.S., Huba J.D., 2012, Extreme changes in the dayside ionosphere during a Carrington-type magnetic storm, *J. Space Weather Space Clim.*, 2, A05(1) – A05(7).
- Verkhoglyadova O.P., Tsurutani B.T., Mannucci A.J., Mlynczak M.G., Hunt L.A., Paxton L.J., Komjathy A., 2016, Solar wind driving of ionosphere-thermosphere responses in three storms near St. Patrick's Day in 2012, 2013, and 2015, *J. Geophys. Res. Space Phys.*, 121, 8900–8923.
- Watari S., 2017, Geomagnetic storms of cycle 24 and their solar sources, *Earth Planet Space*, 69, 70(1)–70(8).
- Waters C.L., Gjerloev J.W., Dupont M., Barnes R.J., 2015, Global maps of ground magnetometer data, *J. Geophys. Res. Space Phys.*, 120, 9651–9660.
- Webb D.F., Howard T.A., 2012, Coronal mass ejections: observations, *Living Rev. Solar Phys.*, 9, 1–83.
- Welling D.T., Jordanova V.F., Zaharia G., 2011, The effects of dynamic ionospheric outflow on the ring current. *J. Geophys. Res.*, 116, A00J19.
- White O., Kopp G., Snow M., Tapping K., 2011, The solar cycle 23–24 minimum. A benchmark in solar variability and effects in the heliosphere, *Solar Phys.*, 274, 159–162.
- Williams P.E., Pesnell W.D., 2011, Comparisons of supergranule characteristics during the solar minima of cycles 22/23 and 23/24, *Solar Phys.*, 270, 125–136.
- Wu C.C., Liou K., Lepping R.P., Hutting L., Plunkett S., Howard R.A., Socker D., 2016, The first super geomagnetic storm of solar cycle 24: “The St. Patrick's day event (17 March 2015)”, *Earth Planet Space*, 68, 151(1)–151(12).
- Yao Y., Liu L., Kong J., Zhai C., 2016, Analysis of the global ionospheric disturbances of the March 2015 great storm, *J. Geophys. Res. Space Phys.*, 121, 12157–12170.
- Yizengaw E., Moldwin M.B., Zesta E., Biouele C.M., Damtie B., Mebrahtu A., Rabiou B., Valladares C.F., Stoneback R.A., 2014, The longitudinal variability of equatorial electrojet and vertical drift velocity in the African and American sectors, *Ann. Geophys.*, 32, 231–238.
- Zakharenkova I., Astafyeva E., Cherniak I., 2015, Early morning irregularities detected with spaceborne GPS measurements in the topside ionosphere: A multisatellite case study, *J. Geophys. Res. Space Phys.*, 120, 8817–8834.
- Zakharenkova I., Astafyeva E., Cherniak I., 2016, GPS and GLONASS observations of large-scale traveling ionospheric disturbances during the 2015 St. Patrick's Day storm, *J. Geophys. Res. Space Phys.*, 121, 12138–12156.
- Zolotukhina N., Polekh N., Kurkin V., Rogov D., Romanova E., Chelpanov M., 2017, Ionospheric effects of St. Patrick's storm over Asian Russia: 17–19 March 2015, *J. Geophys. Res. Space Phys.*, 122, 2484–2504.

<https://doi.org/10.22201/igeof.00167169p.2022.61.4.2045>

Identification for a Favorable Area of Groundwater Exploitation Based on Structural and Geoelectrical Data in Fractured Aquifer in Southern Brazil

César Augusto Moreira¹ , Livia Portes Innocenti Helene² 

Received: April 12, 2020; accepted: April 22, 2022; published on-line: October 1, 2022.

RESUMEN

La complejidad estructural inherente a los acuíferos fracturados, que controla la acumulación y el flujo de agua subterránea en zonas restringidas, puede dar lugar a un elevado número de pozos tubulares no productivos. El análisis combinado de las características geomorfológicas y las investigaciones indirectas, como los métodos geofísicos, permite identificar objetivos favorables para la explotación de aguas subterráneas. Este trabajo trata de los estudios estructurales regionales y locales acoplados con datos de tomografía de resistividad eléctrica con el fin de identificar objetivos favorables para la explotación de aguas subterráneas para el consumo urbano en un granito fracturado situado en la ciudad de Caçapava do Sul, en el sur de Brasil. El control estructural se manifiesta en las formas del terreno regional y condiciona claramente la orientación de los drenajes principales. Basándose en este control estructural, se realizaron cuatro líneas paralelas de tomografía de resistividad eléctrica en una zona de interés para la explotación de aguas subterráneas, seguidas de la generación de modelos de inversión 2D y de modelos pseudo 3D. El contacto entre el suelo superficial muy fino y el macizo granítico subyacente determina la existencia de un acuífero libre regional y la probable recarga del acuífero fracturado. En los modelos de inversión 2D se producen variaciones bruscas de resistividad relacionadas con las fracturas verticales localmente reconocidas en el yacimiento, aunque no muestran continuidad lateral (fuera del plano). El análisis de los mapas geofísicos a partir de 40 metros de profundidad permite reconocer tres alineaciones de baja resistividad (alrededor de $500 \Omega m$) dentro de un contexto granítico donde predominan los valores altos (por encima de $15000 \Omega m$). Estas alineaciones muestran un patrón de triple intersección de fracturas reconocido también en las imágenes de satélite, que son altamente favorables para la acumulación y explotación de aguas subterráneas.

PALABRAS CLAVE: acuífero fracturado, análisis estructural, tomografía de resistividad eléctrica, modelización 3D

Editorial responsibility: Roger Almicar González-Herrera

*Corresponding author at moreirac@rc.unesp.br

¹Geology Department, Geosciences and Exact Sciences Institute (IGCE), São Paulo State University (UNESP), São Paulo State, Brazil

ORCID <https://orcid.org/0000-0002-6949-6679>

²São Paulo College of Technology (FATEC), Jauú, Brazil

ABSTRACT

The inherent structural complexity of fractured aquifers, which controls the groundwater accumulation and flow in restricted zones, can lead to a high number of non-productive tube wells. The combined analysis of geomorphological features and indirect investigations like geophysics methods allows the identification of favorable targets for groundwater exploitation. This paper deals with regional and local structural surveys coupled with electrical resistivity tomography data in order to identify favorable targets for groundwater exploitation for urban consumption in a fractured granite located in Caçapava do Sul city, southern Brazil. The structural control is manifested in the regional landforms and clearly conditions the orientation of main drainages. Based on this structural control, four parallel electrical resistivity tomography lines were performed in an area of interest for groundwater exploitation, followed by the generation of 2D inversion models and pseudo 3D models. The contact between the very thin superficial soil and the underlying granite massif determines the existence of a regional free aquifer and the probable recharge of the fractured aquifer. In the 2D inversion models, abrupt variations of resistivity related to locally recognized vertical fractures in the field occur, although they do not show lateral continuity (out of plane). The analysis of the geophysical maps from 40 meters depth allows the recognition of three alignments of low resistivity (around 500 Ω m) within a granite context where high values predominate (above 15000 Ω m). These alignments show a triple fracture intersection pattern also recognized in satellite images, which are highly favorable for groundwater accumulation and exploitation.

KEY WORDS: fractured aquifer, structural analysis, electrical resistivity tomography, 3D modeling

INTRODUCTION

Brazil is a country of continental dimensions, dominated by tropical climate and highly variable rainfall regimes. The collection and distribution of water in Brazil is primarily based on surface sources, such as rivers and lakes. Issues related to the expansion of urban centers in different regions of the country, seasonal events of prolonged drought and the predominance of precarious water infrastructure represent the main causes of shortages or intermittent supply of water to urban centers.

Based on data from 2018, the country has on average 84% of households with access to water and only 53% served by sanitary sewage systems, with a 45% for the case of the southern region of Brazil (SNIS, 2018). Sewage collection and direct river discharge is the predominant form of sanitary sewage in small and medium-sized cities in Brazil, with direct environmental impacts on flora and fauna, as well as restricting its use in response to public supply demands (SNIS, 2018).

The universalization of the public water supply system in Brazil is a reality based on massive public investment and public-private partnerships. However, a question of great relevance is the average loss of 38% of water throughout the distribution system, due to its length and complexity, lack of maintenance, degradation of the system, clandestine connections, among other aspects (SNIS, 2018). In European countries, this average is 15 to 25% and in Japan reaches 8% at most (DIEESE, 2016).

An alternative to the extensive and inefficient public supply networks is the use of independent water collection systems. In regions lacking surface water sources or peripheral to the usual public supply systems, groundwater sources may be a highly practicable technical and economical alternative (Balek, 1989).

Although surface water pollution, the interactions between surface and groundwater in the hyporheic zone, have a great capacity to attenuate this pollution due to the specific geochemical environment

found in these regions, which can translate quality in groundwater even in these areas of recharge of influent streams (Hester *et al.*, 2013). The extraction of groundwater is an alternative that has been increasingly exploited by industries, agriculture and communities far from public water supply networks (Hiscock, 2005; Elgzeli *et al.*, 2013).

Fractured aquifer systems are considered particularly complex, due to the condition of storage and transmission of water throughout the fractured planes. Although recharge occurs mainly from rain-water or from free surficial aquifers. In many cases, the existence of groundwater in fractured zones is not always evident from the surface (McCuen, 1998; Singhal and Gupta, 2010).

The intrinsic structural complexity of fractured aquifer systems frequently results in the predominance of dry wells or with insufficient flows to meet the human demands. In this sense, the identification of favorable sites to groundwater accumulation is the geomorphological interpretation of aerial photographs and satellite images, combined with geological field works and geophysical surveys (Brassington, 2007).

Geophysical methods represent a powerful tool in the study of fractured rock aquifers, in view of their sensitivity to measure physical parameters that change in the presence of water within fractures, wide spatial coverage and versatility in the depths of investigation, as well as a limited time for data acquisition and processing (Telford *et al.* 2004). An essential aspect in the geophysical studies of fractured aquifers is the reduction of uncertainties and the possibility of defining promising targets for water exploitation, and the reduction of costs in drilling (Knödel *et al.*, 2007).

The use of Electrical Resistivity Tomography (ERT) allows two-dimensional underground investigations, which may reveal potential fractured rock aquifers. A particularly challenging paradigm is the adaptation of a geophysical survey method with mathematical formulation based on isotropic and homogeneous media for use in highly anisotropic and heterogeneous media (Rubin and Hubbard, 2005). Even so, studies involving ERT surveys in a crystalline geological environment showed that the method is efficient in this kind of hydrogeological investigation (Okpoli, 2013; Sequeira Gómez & Escolero Fuentes, 2010; Moreira *et al.*, 2016; Moreira *et al.*, 2019).

This work presents and discusses the results obtained by using geological and structural analysis, coupled with ERT surveys for the identification of favorable areas for groundwater extraction in a small village located in southern Brazil, which possess restricted surface water resources. The acquisition of geoelectrical data and the generation of pseudo 3D models from 2D inversion employed in this study, aims to recognize structural alignments at various depths, which represent potential targets for groundwater exploitation.

MATERIAL AND METHODS

GEOLOGY OF THE STUDY AREA

The study area is in a rural property six kilometers north from center of Caçapava do Sul, a municipality located in southern Brazil (Figure 1). This region of the State of Rio Grande do Sul (RS) comprises small size municipalities with population varying between 10,000 and 60,000 inhabitants. Economic activity is based on soybean farming, extensive livestock farming and services.

Basic sanitation services are managed by Corsan (Companhia Riograndense de Saneamento S/A), a state-owned company created in 1965 currently serving 2/3 of the state population or 6 million



Figure 1. Study area location, with disposition of the electrical resistivity tomography lines.

people in 316 municipalities. The urban area of the municipalities under its administration is almost universally served by intermittent supply of drinking water, although it presents under 30% of collection and sanitary sewage. The rural area is predominantly served by surface or groundwater, independent of the public network, which serves only the urban centers.

Geologically, the study area is part of the syntectonic Caçapava do Sul granitic suite, contained in the Ocidental Domain of the Sul-Rio-Grandense Shield (CPRM, 2000). The syntectonic granitoids intruded the metamorphic units of the Ocidental Domain and show mylonitic foliation with NNE orientation.

The Caçapava do Sul granitic suite comprises a dome-like shaped body with 25 km² oriented in the N-S direction, dated 549 Ma, and surrounded by low-grade metamorphic rocks. The contacts of the Caçapava do Sul granitic suite with the metasedimentary rocks of the Vacacaí Metamorphic Complex are generally concordant with the main foliation of the metamorphites (Nardy and Bitencourt, 1989).

This suite is dominantly constituted by monzo and syenogranitic rocks. Granodioritic and tonalitic rocks are less common and occur in the western border of the main intrusive body. Due to the diverse petrographic types of granitoid rocks, the Caçapava do Sul suite has been described by three main lithofacies: biotite granites, leucogranites and transitional granites (CPRM, 2000).

Structural analyzes performed by Bittencourt (1983) in the northern and southeastern regions of the Caçapava granitic suite allowed the recognition of three deformation events. The first event is related to the development of pre-kinematic porphyroblasts with respect to the regional foliation of the host rocks. The second event is associated to the development of the regional foliation, which

also affected the granitoid rocks, and the last deformation event was responsible for the generation of an antiform structure where the Caçapava do Sul granitic suite is lodged. The last two deformation events significantly affected the Caçapava do Sul intrusive suite. Regionally, these events are defined as D3 and D4 deformation phases and are both related to compressive stress during magma cooling, in 549 Ma (Nardi and Bitencourt, 1989).

In the east center of the study area there is a pond which was excavated up to the contact with the granitic rock, with 2m of deep. It is believed that the fractured aquifer system and the pond may be recharged by the free aquifer, since during the dry season it remains with water. Generally, the flows produced by wells are small, and the water, due to the lack of circulation and the type of rock, is, in most cases, salinized (PMSB, 2013). Wells usually have specific capacities below 0.5 m³/h/m, with dry wells also occurring (Machado & Freitas, 2005).

STRUCTURAL AND GEOPHYSICAL SURVEY

Fractures are often detected in aerial photographs because they are recognized by linear changes in topography, drainage, or vegetation patterns, as well as different colors of rocks and soils (Miller and Miller, 1961; Sabins, 1985; 1996). In addition, fractured rocks show signs of weathering and erosion (Knödel *et al.*, 2007).

In the field, the first stage of data acquisition consisted of a preliminary geological reconnaissance, consisting of the identification of rock exposures. This analysis structural work carried out in granite outcrops found in the vicinity of the study area was of paramount importance for defining the main fracture families. At the study site, granite is found with varying degrees of alteration and fracturing, often being covered by fractured sandy lithosol.

The amount and orientation of the electrical tomography profiles was driven by the regional structural data, field structural data and by the availability of accesses to the study area. The acquisition of geophysical data consisted of electrical resistivity readings using the electrical resistivity tomography (ERT) technique in a Wenner-Schlumberger arrangement. This configuration tends to have more sensibility and favor the representation of lateral variations, being more suitable for the identification of conductive (low resistivity) vertical structures or zones (Moreira *et al.*, 2016).

In a crystalline geological environment, as in the case of the study area, the expected hydrogeological profile is one of shallow soil responsible for recharging possible fracture zones. To detail this more superficial zones, 10 m of spacing among electrodes were used in four parallel survey lines oriented in the N282 direction with individual length of 400 m and (Figure 1).

The geophysical equipment used was the Terrameter LS, manufactured by ABEM Instrument (Sweden), which consists of a single automated signal transmission and reception module (based on previous programming), with 250W of power, 1μV resolution and maximum electric current of 2.5A (ABEM, 2012).

The measurements acquired in the field were processed in the Res2Dinv computational program. The results comprise resistivity profiles of distance versus depth presented in logarithmic scale in which the values are inverted, interpolated, and displayed in intervals of colors. This program automatically determines a two-dimensional subsurface model from resistivity obtained in ERT surveys (Griffiths and Barker, 1993).

The 2D model used in the program divides the pseudo-section into rectangular blocks, which will represent the pseudo-section by adjusting the field measurements. This optimization aims to reduce the difference between the apparent resistivity values, calculated and measured in the field, by adjusting the resistivity of the block model, whose difference is expressed by the root mean squared error (RMS), and its product is represented as inversion models (Loke and Barker, 1996).

The two-dimensional inversion numerical data of each section was gathered in a single spreadsheet, which joins the position of the readings along the surveying lines (variable "x"), spacing of the surveying lines (variable "y"), depth modeled by inversion (variable "z") and the electrical resistivity value (variable "R"). This spreadsheet was used in order to generate 3D visualization models, in a routine of basic steps embraced in mineral exploration. In this case, the sampling plan is often defined from statistical, structural and geometrical criteria of mineral accumulations (Moon, 2006).

Geophysical 3D visualization models derived from 2D sections, also known as quasi-3D or pseudo-3D models, provide a very broad understanding of the complexity of geological structures and mineral deposits; but also, present significant results in applied geophysics in contaminated areas, tailing dams and hydrogeology (Moreira *et al.*, 2015; Côrtes *et al.*, 2016; Camarero *et al.*, 2019; Helene *et al.*, 2021).

RESULTS AND DISCUSSION

Initially, the results are based on regional geomorphological lineaments interpreted from satellite images that reveals a similar pattern in both the granitoid rocks and the surrounding metamorphic complex (Figure 2B). The fracture orientations were extracted from satellite imagery and integrated with measurements on rock exposures and assembled in a diagram (Figure 2C), which indicates predominant orientation for N315°, with fracture groups in the N350° and N50° directions with less frequency.

Geophysical fieldwork was driven by previous geological survey in order to identifying rock exposures and geological fractures (Figure 3A and 3B). In a road close to the study area occur outcrops of jointed and fresh porphyritic leucogranites (Figure 3C).

The resistivity models generated from the ERT data are presented in logarithmic scale to allow a comparative analysis among the sections and the range of resistivity values varied from 11 Ωm to 51.851 Ωm RMS below 8%, indicative of low deviation and satisfactory models (Figure 4).

The inversion models are characterized by a superficial layer with resistivity values lower than 100 Ωm with a significant variation of thickness, but limited between the interval of 0m and 40m, which possibly reflects the regolith profile. This wide variation in the thickness of this superficial layer reflects a selective action of weathering processes and alteration of granite rock.

The deeper portions of the profile are related to the ease of rainwater infiltration in fractured zones and consequent hydration of minerals such as feldspars and micas. The shallower portions, which are more resistant to chemical weathering, are constituted by unjointed or moderately jointed rock masses, with predominance of quartz in the rock matrix. Portions of the rock mass with resistivity values lower than 40 Ωm may indicate higher permeability, with accumulation of groundwater and/or rocks enriched in weathered minerals like biotite and feldspars, that locally result in concentrations of clay minerals in fractures. Resistivity values greater than 1.000 Ωm indicate the presence of loose rocky masses and moderately weathered.

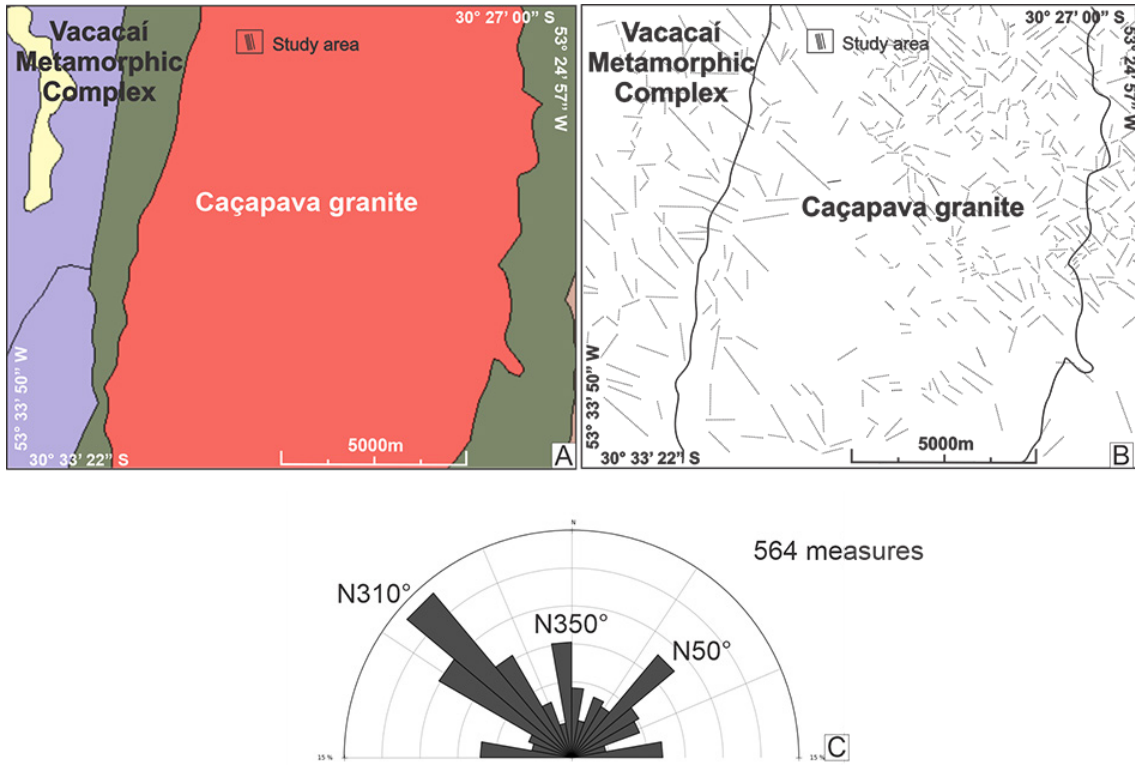


Figure 2. Geological and structural aspects of the study area. 2A) Main regional geological units. 2B) Regional lineaments extracted from satellite images. 2C) Diagram of structural measurements obtained from satellite images and field measurements

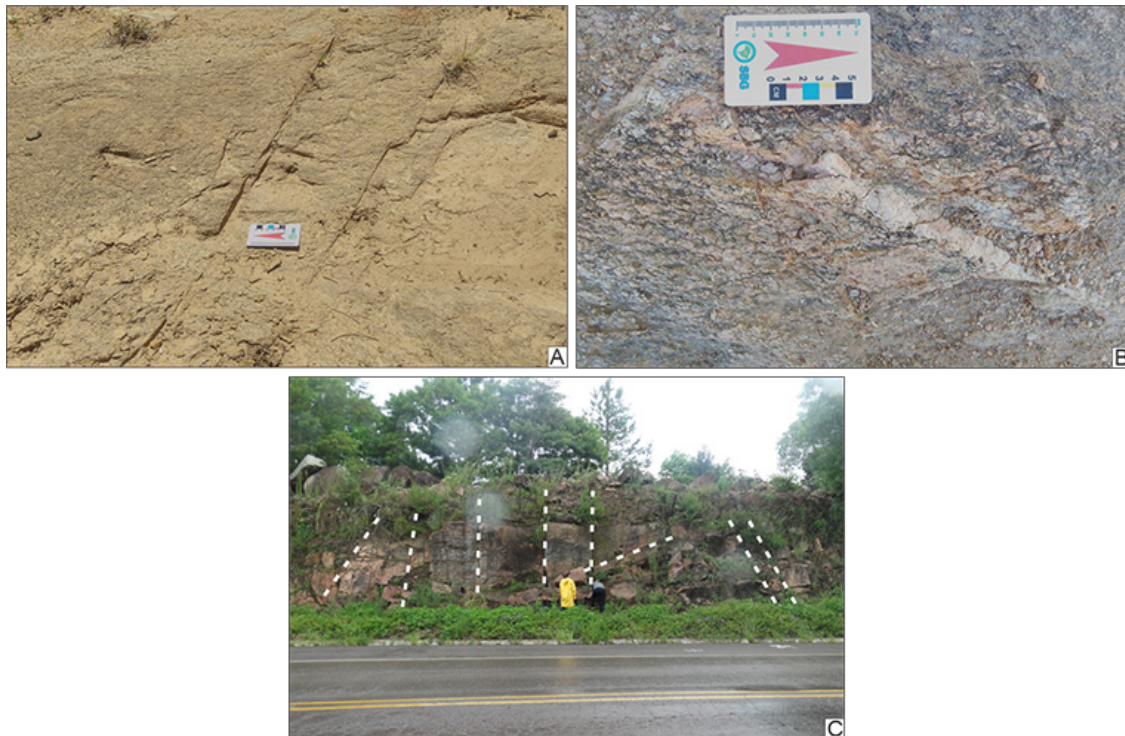


Figure 3. Geological features identified in structural survey: 3A) fractures in sandy saprolite. 3B) fractures in fresh granite. 3C) fractures in granite massif

The Line 3 presents values between 1.000 Ωm and 5.000 Ωm , the smallest range of variation among the set of sections studied. The other sections exhibit values of resistivity predominantly between 1.000 Ωm and 20.000 Ωm , and some portions with extreme values, greater than 50.000 Ωm . This huge variation in resistivity values may be related to variations in the moisture content of the rock-mass. The resistivity values higher than 20.000 Ωm displayed in the profiles were intended to enhance linear features related to fractures and faults (Figure 4).

The orientation and slope of the fractures interpreted in the profiles of Figure 4 are consistent with the structural pattern described during the preliminary geological reconnaissance phase (Figure 2 and 3). Although contained largely within highly resistive zones, except for Line 3, this set of geological fractures possibly presents a connection with the weathering mantle and, consequently, with the free aquifer.

The ERT lines were planned with the objective of identifying linear structures with lateral continuity. However, an analysis of the positions of the fractures projected in the sections reveals independent fractures and limited lateral continuity, which, at first, indicates low favorability for groundwater exploitation, once the connectivity and lateral continuity of the structures is a key factor for groundwater accumulation.

In order to evaluate the lateral continuity and possible connectivity of the fractures recognized in the 2D sections, 3D visualization models were elaborated, and resistivity maps were generated for different depths (Figure 5).

The map referring to the elevation of 395m is characterized by wide diffuse areas with electrical resistivity below 100 Ωm , evidence of accumulation of water in the superficial porous aquifer. The maps of the elevation of 385m to 365m show a reduction of areas of low resistivity and an increase of areas where saprolite rock and granite rock with distinct degrees of chemical weathering may predominate. These maps do not show evidence of linear features like fractures or faults, possibly due to the chemical weathering of the rockmass, which attenuates the contrasts of the geophysical properties, resulting in a homogeneous medium.

From the elevation of 355m, there are indications of a possible linear features that form a triple junction pattern of lineaments oriented in the N104, N205 and N325 directions. This feature is most evident in the maps of the elevation of 345m and 305m (Figure 5).

The integrated analysis of the 2D inversion models and the 3D visualization models (pseudo 3D) allow some considerations. The resistivity pattern found in Line 3 where values below 4.500 Ωm predominates is essentially related to the orientation of this line along a possible saturated geological fracture. This resulted in a relatively homogeneous pattern, distinct from the average values for the granite rock horizon of the other sections that is above 15.000 Ωm and below the elevation of 355m.

The existence of individual fractures in a rockmass with low resistivity does not make it promising for the exploitation of groundwater. Fracture connectivity is a key condition for the storage and transmission of groundwater in fractured rock aquifers. Even in the absence of local superficial evidence, a fracture system, relevant to the groundwater flow, can be manifested on a regional scale, conditioning the relief and the drainage network. Such aspects are usually considered in studies of fractured aquifers (Lee and Farmer 1993; Skinner and Graham 2004; Zouhri and Lutz 2016; Moreira *et al.*, 2017).

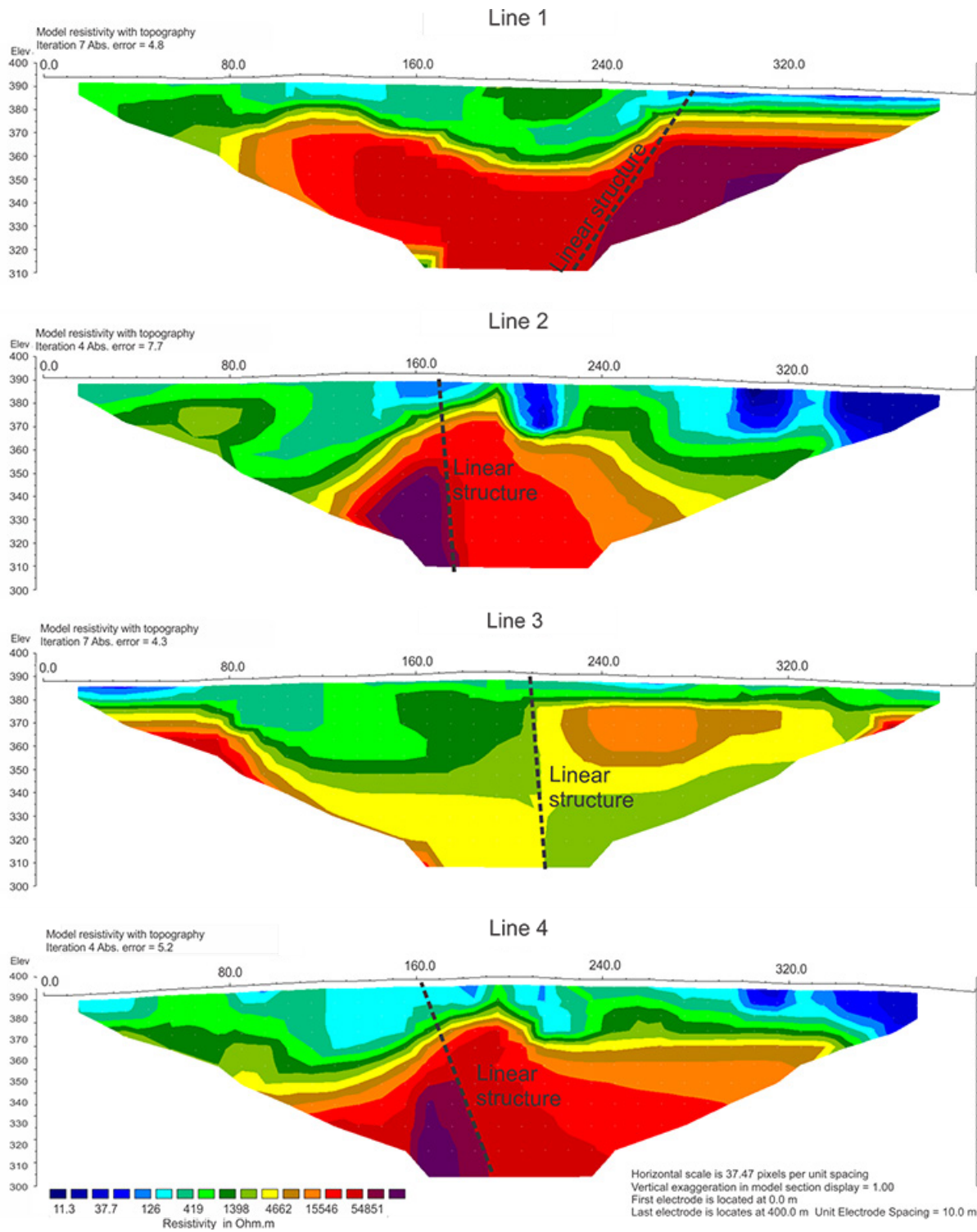


Figure 4. Electrical resistivity inversion models with interpretation of linear features (fractures) related to geological structures.

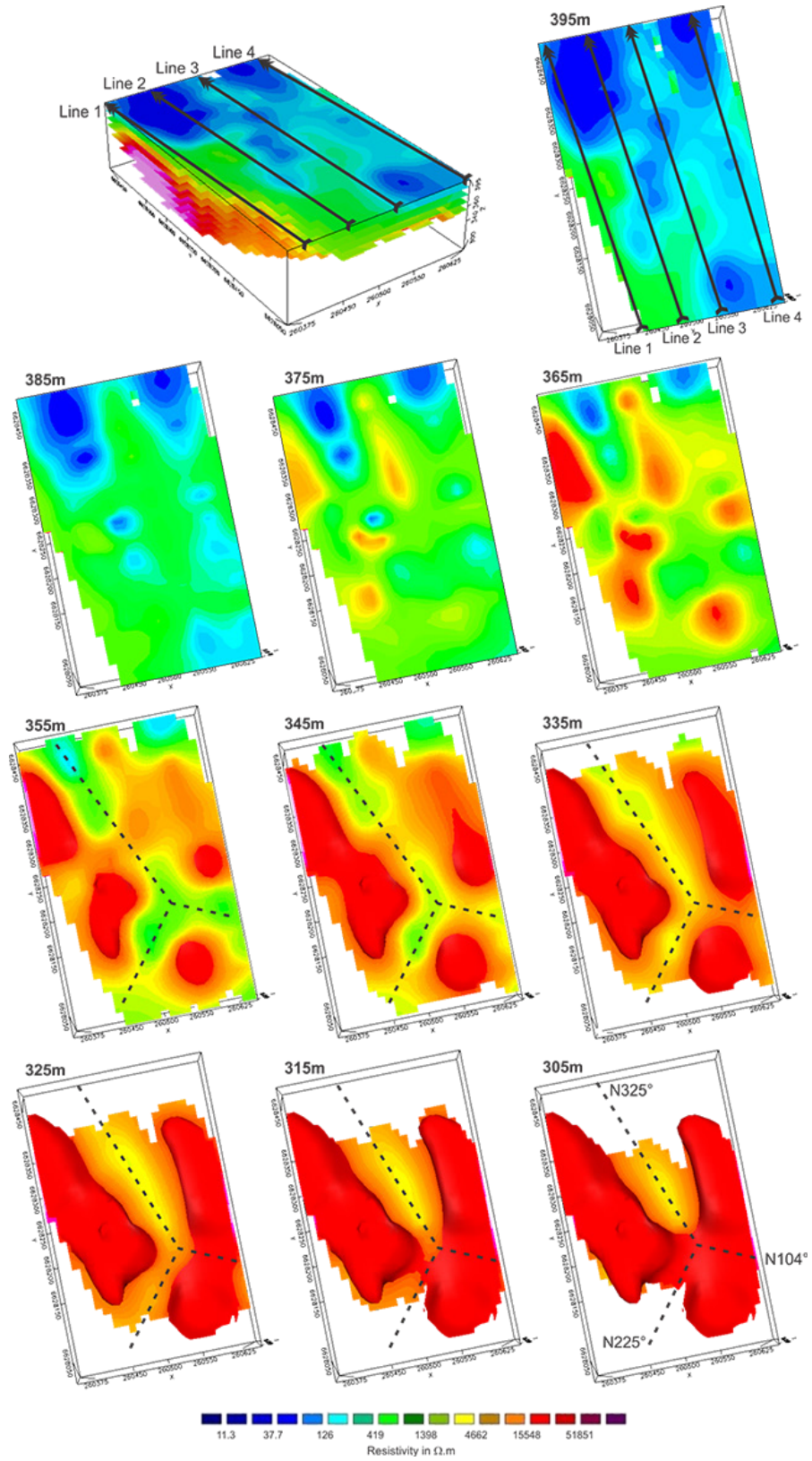


Figure 5. Pseudo 3D model and maps of electrical resistivity sliced for different elevations (in meters above sea level), with interpretation of linear structures (potential fractures).

Figure 6 compares the drainage network pattern in the region of study, with anomalous zones of resistivities in the study area for 60m depth in this study. As it can be seen by the satellite image, there is a high correlation of these drainage patterns at different scales. The area of intersection among the structural alignments represents the most favorable locations for groundwater exploration.

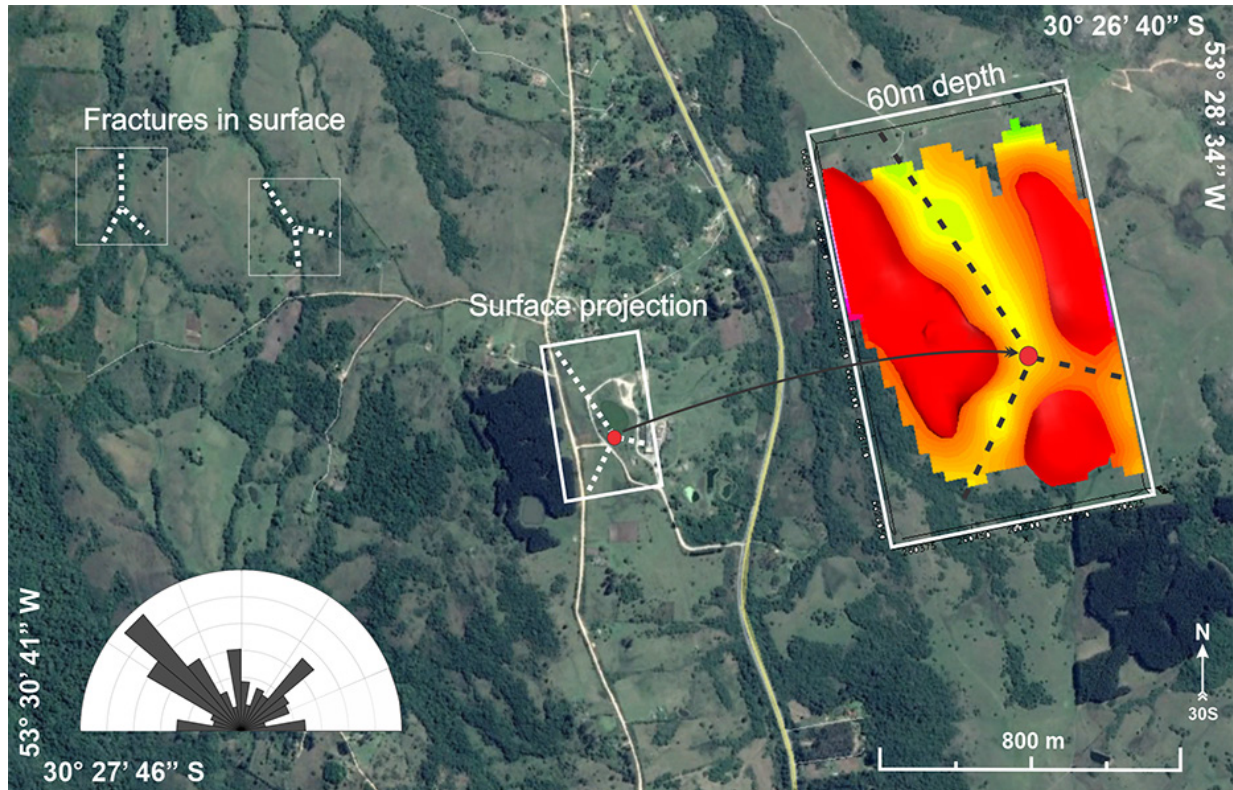


Figure 6. Drainage pattern similar to the triple junction geophysical anomaly recognized in this study, with most favorable area for groundwater exploitation (red dot).

CONCLUSIONS

Geological fractures are essential features for the storage and movement of groundwater throughout rocky masses. The expression of these landforms on the topographic surface is not always evident. The joint analysis of geomorphological and structural aspects both locally and regionally, are essential for the programming of geophysical surveys geared to hydrogeological studies.

The technique of electrical resistivity tomography is particularly relevant in the identification of geological discontinuities that can serve as pathways for the accumulation and movement of groundwater. However, this work revealed a particular case, in which the geological structures identified in the 2D inversion models, similar to those described in rocky exposures, would be, in principle, poorly favorable for hydrogeological purposes due to the apparent lack of connectivity of structures.

The connectivity of the fracture system was clearly highlighted in the pseudo 3D models. Below 40m depth, low resistivity values (about 500 Ωm), aligned in three different well-defined directions, were detected adjacent to high resistivity values ($> 15.000 \Omega\text{m}$), which indicate the presence of saturated fractures. Similar structural features are recognized in the drainage network around the study area to which water springs are associated. The low number of producing wells for groundwater exploitation

in fractured rock aquifers can be substantially increased by integrating traditional geological analysis at different scales and geophysical research tools.

REFERENCES

- ABEM, 2012, Terrameter LS – Instruction Manual, 122p.
- Balek, J., 1989, Groundwater resources assessment – Developments in water Science 38. Elsevier, Praga, 251p.
- Bittencourt, M.F., 1983, Metamorfitos da região de Caçapava do Sul, RS – Geologia e relações com o corpo granítico. Simpósio Sul-Brasileiro de Geologia. *Brazilian Geological Survey*. Porto Alegre, 37-49.
- Brassington, R., 2007, Field Hydrogeology. John Wiley & Sons, Chichester, 279pp.
- Camarero P.L., Moreira C.A., Pereira H.G., 2019, Analysis of the Physical Integrity of Earth Dams from Electrical Resistivity Tomography (ERT) in Brazil. *Pure and Applied Geophysics*, 176, 1-13.
- Côrtes A.R.P., Moreira C.A., Veloso D.I.K., Vieira L.B., Bergonzoni, F.A., 2016, Geoelectrical prospecting for a copper-sulfide mineralization in the Camaquã sedimentary basin, Southern Brazil. *Geofísica Internacional*, 55-3, 107-117.
- CPRM–Companhia de Pesquisas de Recursos Minerais, 2000, Folha Cachoeira do Sul, RS. Escala 1:250.000. CPRM, Brasília.
- DIEESE–Departamento Intersindical de Estatística e Estudos Socioeconômicos, 2016, Visão geral dos serviços de água e esgotamento sanitário no Brasil. Brasília.
- Elgzeli Y.M., Ondovčín T., Zbyněk H., Jiří K., Jiří M., 2013, Impact of heavy groundwater pumping on hydrogeological conditions in Lybia: Past and present development and future prognosis on a regional scale. *Acta Geologica Polonica*, 63, 283-296.
- Griffiths D.H., Barker R.D., 1993, Two-dimensional resistivity imaging and modeling in areas of complex geology. *Journal of Applied Geophysics*, 29, 211-226.
- Hamza S.M., Ahsan A., Daura H.A., Imteaz M.A., Ghazali A.H., Mohammed T.A., 2016, Fractured rock aquifer delineation and assessment using spatial analysis in Kano, Nigeria. *Arabian Journal of Geoscience*, 9, 367.
- Hester E.T., Young K.I., Widdowson M.A., 2013, Mixing of surface and groundwater induced by riverbed dunes: Implications for hyporheic zone definitions and pollutant reactions. *Water Resources Research*, 49, 5221-5237.
- Helene, L. P. I; Moreira, C.A., 2021. Analysis of Leachate Generation Dynamics in a Closed Municipal Solid Waste Landfill by Means of Geophysical Data (DC Resistivity and Self-Potential Methods). *Pure And Applied Geophysics*, v. 2, p. 690-703.
- Hiscock K.M., 2005, Hydrogeology: principles and practice. Blackwell Publishing, Oxford, 405pp.
- Knödel K., Lange G., Voigt H., 2007, Environmental geology: handbook of fields methods and case studies. Springer, Hannover, 1357pp.
- Lee C.H., Farmer I., 1993, Fluid Flow in Discontinuous Rocks. Chapman Hall, London, 170pp.


- Loera H.L., Leal J.A.R., Harris P.D., Gaytan D.E.T., Ruiz V.J.M., Gogichaishvili A., 2015, Geophysical Exploration of Fractured-Media Aquifers at the Mexican Mesa Central: Satellite City, San Luis Potosí, Mexico. *Surveys in Geophysics*, 36, 167–184.
- Loke M.H., Baker R.D., 1996, Rapid least-squares inversion of apparent resistivity pseudosections by quasi-newton method. *Geophysical Prospecting*, 44, 131–152.
- Machado, J. L. F; Freitas, M. A. Projeto mapa hidrogeológico do Rio Grande do Sul: relatório final. Porto Alegre: CPRM, v. 1, 2005.
- McCuen R., 1998, Hydrologic analysis and design. Prentice Hall, Upper Saddle River.
- Miller, V., Miller, C. F., 1961, Photogeology. McGraw-Hill, New York.
- Moreira C.A., Munhoz T., Cavallari F., Helene L.P.I., 2015, Electrical resistivity to detect zones of biogas accumulation in a landfill. *Geofísica Internacional*, 54, 4, 353-362.
- Moreira, C A; Lapola, M. M.; Carrara, A., 2016. Comparative analyzes among electrical resistivity tomography arrays in the characterization of flow structure in free aquifer. *Geofísica Internacional*, v. 55, p. 119-129.
- Moreira C.A; Leandro C.G., Lopes C.T., Ilha L.M., 2017, DC resistivity investigation in a fractured aquifer system contaminated by leachate from an old dump. *Geofísica Internacional*, 56, 4, 229-241.
- Moreira, C A; Helene, L. P. I.; Rosa, F. T. G. ; Hansen, M. A.; Malagutti filho, W.; Dourado, J. C, 2019, Análise comparativa entre arranjos de tomografia elétrica no reconhecimento de estruturas de fluxo em aquífero fraturado em Caçapava do Sul (RS). *Pesquisas em Geociências (Online)*, v. 46, p. e0710.
- Moon C.J., Whateley M.K.G., Evans A.M., 2006, Introduction of mineral exploration. Blackwell Publishing, Malden, 499pp.
- Nardy L.V.S., Bittencourt M.F., 1989, Geologia, petrologia e geoquímica do Complexo Granítico Caçapava do Sul, RS. *Revista Brasileira de Geociências*, 19, 2, 153-169.
- Okpoli, C.C, 2013, Sensitivity and resolution capacity of Electrode configurations. *International Journal of Geophysics*, 2013, 12 p. p.
- PMSB–Prefeitura Municipal de Caçapava do Sul. Plano Municipal de Saneamento Básico. 71p., 2013.
- Rubin Y., Hubbard S.S., 2005, Hydrogeophysics. Springer, Dordrecht, 523pp.
- Sabins, F. F., 1996, Remote sensing–Principles and interpretation. 3rd. edition, Freeman, San Francisco.
- Sequeira Gómez, L. & Escolero Fuentes, O. 2010. The application of electrical methods in exploration for ground water resources in the River Malacatoya sub-basin, Nicaragua. *Geofísica Internacional*, 49: 27-41
- Singhal B.B.S., Gupta R.P., 2010, Applied hydrogeology of fractured rocks. Springer, Berlin, 408pp.
- Skinner D., Graham H., 2004, A comparison of electrical and electromagnetic methods for the detection of hydraulic pathways in a fractured rock aquifer, Clare Valley, South Australia. *Hydrogeology Journal*, 12, 576–590.
- SNIS–Sistema Nacional de Informações sobre Saneamento, 2018, Diagnóstico dos Serviços de Água e Esgotos. Ministério das Cidades, Brasília.

Telford W.M., Geldart L.P., Sheriff R.E., 2004, *Applied Geophysics*. Cambridge University Press, New York, 770pp.

Zouhri L., Lutz P., 2016, Hydrogeophysical characterization of the porous and fractured media (chalk aquifer in the Beauvais, France). *Environ. Earth Science*, 75, 343-351.

<https://doi.org/10.22201/igeof.00167169p.2022.61.4.2113>

Content of Total Organic Carbon Using Random Forest, Borehole Imaging, and Fractal Analysis: A Methodology Applied in the Cretaceous La Luna Formation, South America

Jorge A. Leal F.¹ , Luis H. Ochoa G.¹, Gustavo A. Sarmiento P.¹

Received: September 18, 2020; accepted: August 30, 2022; published on-line: October 1, 2022.

RESUMEN

Esta investigación presenta un enfoque alternativo para calcular el contenido de carbono orgánico total utilizando registros de cable y técnicas de aprendizaje automático; específicamente, imágenes resistivas de pozo, su resistividad promedio y registro de rayos gamma son empleados para entrenar un modelo regresivo. La metodología se aplicó en la Formación La Luna, la cual ha sido reportada como una de las principales rocas generadoras de Colombia y el oeste de Venezuela. El objetivo de este trabajo es enseñar a una máquina como reconocer patrones entre rasgos fractales en imágenes de pozo y su contenido de carbono orgánico total. El aprendizaje automático implementado se basa en técnicas de aprendizaje por conjuntos, en este caso, un conjunto de árboles de decisión conocido como bosques aleatorios. Los datos empleados tienen un total de 960 mediciones de registros, los cuales fueron divididos aleatoriamente en 80% para entrenamiento y 20% para validación. El resultado es equivalente a la curva obtenida con una regresión semilogarítmica del carbono orgánico medido en el núcleo contra valores de registro de densidad. La precisión de este método es suficientemente alta para ser considerada durante evaluaciones petrofísicas, mostrando un error medio cuadrático de 0.44% y un coeficiente de correlación de Pearson de 0.88. La metodología depende de la calidad de la imagen y cualquier anomalía en estos datos aumentará el error. El modelo generado debe ser recalibrado para otras formaciones, pozos horizontales, desviados y cuando se empleen registro de imágenes durante la perforación.

PALABRAS CLAVE: Formación La Luna, carbono orgánico total, imágenes resistivas de pozo, bosque aleatorio, análisis fractal y yacimientos no convencionales.

Editorial responsibility: Claudia Arango-Galván

**Corresponding author at jalealf@unal.edu.co*

*¹Departamento de Geociencias - Universidad Nacional de Colombia, Bogotá
Kr. 30 # 45-03, campus universitario edificio 224 Bogotá, Colombia.*

ABSTRACT

This research presents an alternative approach to computing the content of total organic carbon using wireline logs and machine learning techniques. Specifically, borehole resistivity imaging, its average resistivity, and gamma rays log are employed to train a regression model. The methodology was applied in La Luna Formation, which has been reported as one of the principal source rocks for Colombia and western Venezuela. This work aims to teach a machine how to recognize patterns between fractal features in borehole images and their content of total organic carbon. Implemented machine learning is based on ensemble learning techniques, in this case, an ensemble of decision trees known as random forest. The working data set totalizes 960 wireline log measurements, randomly split into 80% for training and 20% for validation. The outcome is equivalent to the curve obtained using a semi-log regression of organic carbon measured in core against density log values. The accuracy of this method is high enough to be considered during petrophysics evaluations, showing a root-mean-square error of 0.44% and Pearson's correlation coefficient of 0.88. The methodology depends on image quality, and anomalies in these data increase the error. The generated model must be recalibrated for other formations, for horizontal and deviated wells, and when logging while drilling imaging is employed.

KEY WORDS: La Luna Formation, total organic carbon, borehole resistivity imaging, random forest, fractal analysis and unconventional reservoirs.

INTRODUCTION

In the last two decades, unconventional reservoirs have become one of the ultimate frontiers in hydrocarbon exploration. These reservoirs have been mainly developed in the late Cretaceous of North America, and similar geological settings are gradually catching the attention in other petroliferous regions around the world. One of the most critical parameters to be considered during oil shale and gas shale exploitation is the amount of total organic carbon (TOC). TOC is defined as the weight of organic carbon in a unit weight of rock, commonly expressed in weight percentage (wt.%) in borehole logs. Applications of quantifying TOC can range from evaluating source rock petroleum production to kerogen typing (Steiner *et al.*, 2016).

The late Cretaceous La Luna Formation has been reported as a high potential unconventional reservoir in northern South America (Liborius and Slatt, 2014; Ceron *et al.*, 2013). In western Venezuela, this formation is the principal source rock for the prolific Lago de Maracaibo Basin (Escalona and Mann, 2006). In Colombia, several basins such as Catatumbo, Cesar-Rancherías, Middle Magdalena, Guajira, and Guajira Offshore also have La Luna Formation as the main source rock (Gonzalez *et al.*, 2009). Like other organic-rich formations, TOC in La Luna is obtained from lab geochemical tests or it can be estimated from density, acoustic, and resistivity logging.

During unconventional reservoir evaluation, the most common techniques to calculate TOC from borehole logs are the methods proposed by Schmoker (1983) and Passey (1990). Schmoker and Hester (1983) proposed a method based on regression of density logging versus TOC measured in core; the method was applied in the Mississippian and Devonian Bakken Formation in the United States portion of the Williston Basin. Passey's method, also known as ΔLogR technique, employs the overlaying of a scaled porosity log (generally the sonic transit time) on a deep resistivity curve (Passey *et al.*, 1990); the method is applied to assess TOC in both clastic and carbonate environments.

This work aims to provide an alternative procedure to compute TOC contents using wireline-acquired resistivity imaging and total gamma-ray log. To achieve this goal, a predictive model based on random forest algorithm was developed. This model recognizes patterns in binary and grayscale images, likewise in resistivity and gamma-ray data; using these patterns model computes TOC values along the logged sequence. The available data set has a total of 960 log measurements; these data were randomly divided into 768 samples (80%) for training and 192 for validation (20%). The accuracy of final results is evaluated through residual error, Pearson's correlation coefficient, and root-mean-square error.

The random forest, like any other supervised machine algorithm, has been successfully applied to reservoir characterization (Ao *et al.*, 2018, Krasnov *et al.*, 2017, Baraboshkin *et al.*, 2019). Among the innovations presented in this work, is the application of fractal elements to train and feed a random forest model, focusing on how to supply information in the upstream oil and gas industry. Furthermore, once the predictive model is trained, this research presents a new option to calculate accurate TOC contents using only borehole imaging and gamma-ray data, providing additional value to regular borehole image interpretations.

Figure 1 presents the methodology workflow divided into two main stages, known as the training and regression (or prediction) stages. During training of supervised machines, the model utilizes a labeled dataset (independent variables), and it learns from seen results (dependent variable). Said otherwise, supervised learning is a way to use input variables (x) and an output variable (Y) to train an algorithm to learn the mapping function from the input to the output $\{Y = f(X)\}$. The goal is to approximate the best possible mapping function from input data (x) being able to predict the output variables (Y). It is called supervised learning because the process of learning from the training data set can be thought as a teacher supervising the learning process. The correct answers are known; the algorithm iteratively makes predictions on the training data and is corrected by the teacher. Learning stops when the algorithm achieves an acceptable level of performance (Brownlee, 2016). Finally, during the regression stage, the trained model must be able to figure out the dependent variable. In this case, TOC content equivalents to the TOC obtained through a semi-log regression of organic carbon measured in cores against density logging.

GEOLOGICAL SETTING

Bralower and Lorente (2003) reported that La Luna Formation was originally named the La Luna limestone in 1926 after the Quebrada La Luna in the Perijá range. However, this unit was formally called formation in 1937; the formation consists of thin-bedded and laminated dense dark gray to black carbonaceous-bituminous limestone and calcareous shale. The limestone beds vary from a few centimeters to less than a meter in thickness. The unit is particularly characterized by hard black ellipsoidal and discoidal limestone concretions ranging from a few centimeters to almost a meter in diameter (Bralower and Lorente, 2003).

Common lithofacies in core and outcrops include planktonic and benthic bituminous biomicrites with mudstone, wackestone, and packstone fabric. Upwards, La Luna increases the strata phosphatic content and unleashed a silicification process into those beds (Sarmiento *et al.*, 2015). These features arrangement are settled in normal marine conditions, clearly offshore, and in restricted marine environments. The relatively high sea-level event of the Turonian to Santonian in Colombia and

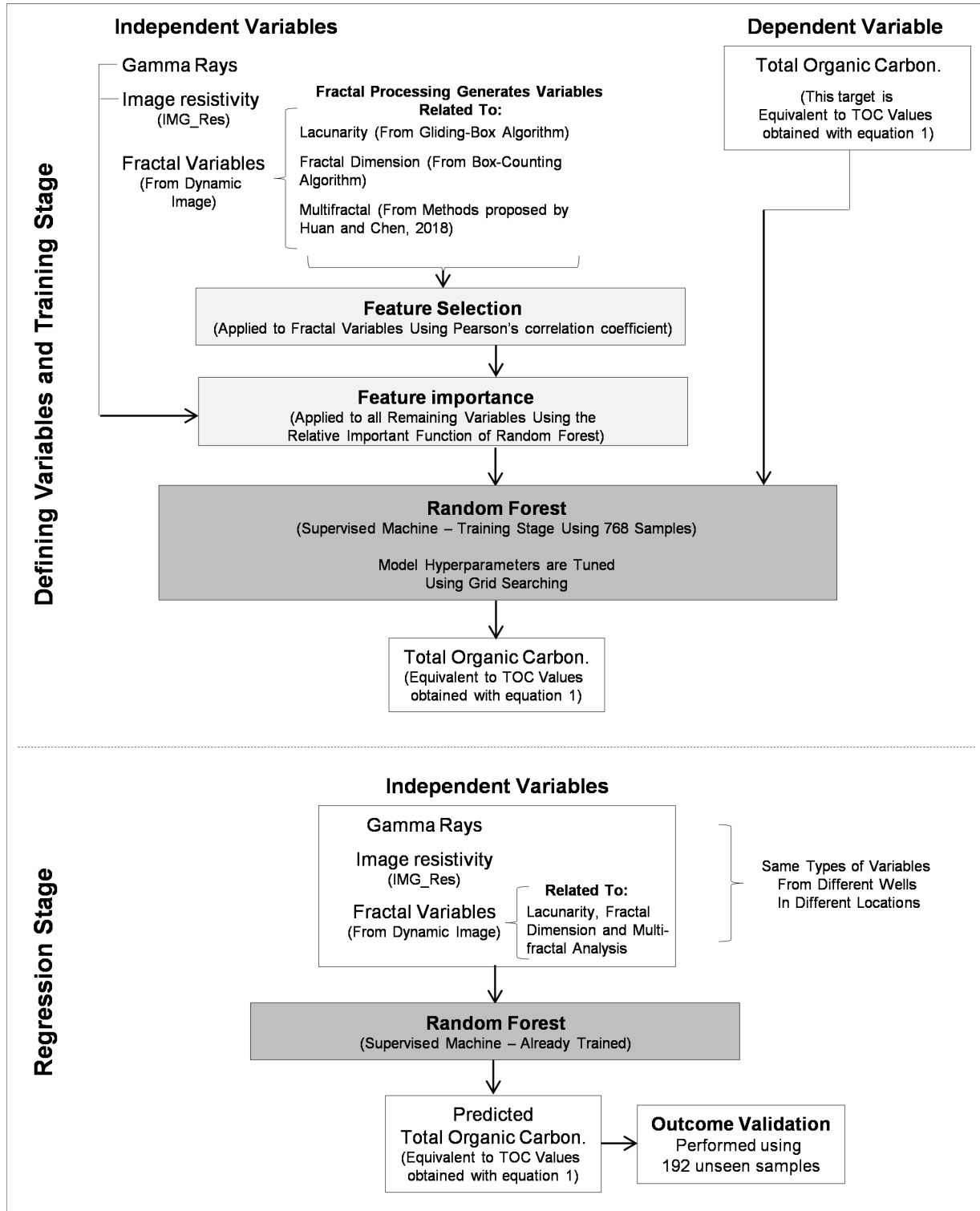


Figure 1. Methodology workflow in training and regression stages

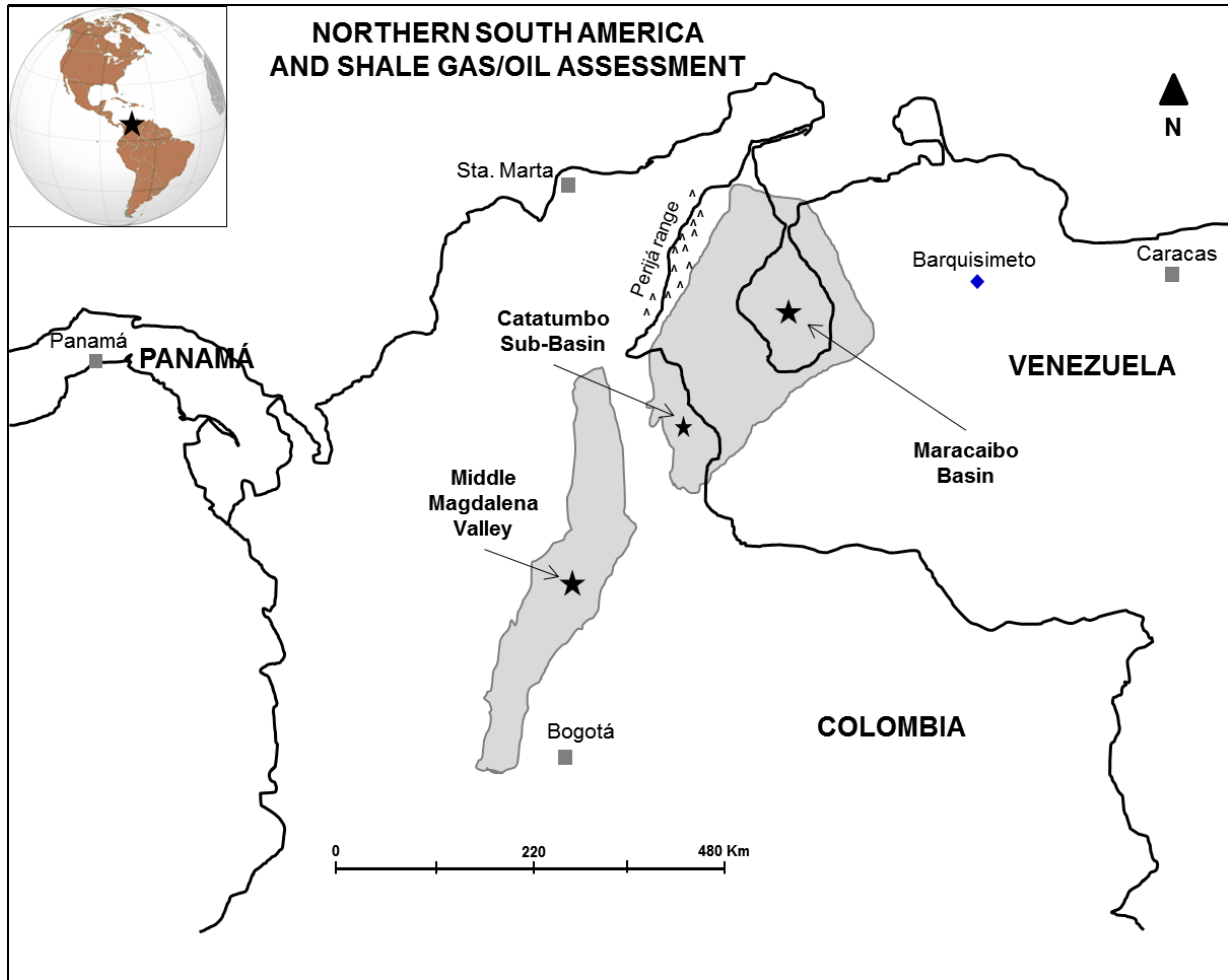


Figure 2. Prospective oil and gas shale plays of northern South America (Modified from EIA, 2015)

Venezuela originated the deposition of large amounts of organic matter contained in the offshore deposits of La Luna Formation (Ceron *et al.*, 2013). The Turonian to Santonian interval of the Cretaceous Colombian basin was deposited during a relatively fast sea level rise (transgressive systems track) and following high sea level or highstand system (Guerrero, 2002).

According to EIA (2015), northern South America has prospective shale gas and shale oil potential within the Cretaceous fossiliferous calcareous mudstone of La Luna Formation, particularly in the Middle Magdalena Valley, and the Maracaibo/Catatumbo basins of Venezuela and Colombia (Figure 2). The organic-rich Cretaceous shale of La Luna Formation averages 5% of TOC, and it sourced much of the conventional oil and gas produced in the Middle Magdalena basin of Colombia and western Venezuela. This formation is similar in age to the Eagle Ford and Niobrara shale plays in the United States (EIA, 2015).

SOURCES AND TYPE OF DATA

RESISTIVITY IMAGING AND AVERAGE PAD RESISTIVITY

The resistivity imaging can be acquired in water or oil-based muds, showing a two-dimensional pseudo image of the wellbore wall. In conductive environments, as in the case of this work, the vertical resolution of image tool is 5 mm, with 80 % of coverage in wells with 21.59 cm of diameter. Borehole imaging is applied for electrofacies classification, structural analysis, fracture characterization, thin layer identification, and direction of main horizontal stresses, among other applications. Typically, two processed images are presented from resistivity normalization, called the dynamic and static images. The dynamic image provides details, allowing recognition of sedimentary structures and classification of textural features; the static image is utilized, but not limited, to highlight resistivity changes usually related to unconformities, fluids contacts, faults, and fractures. Figure 3 shows an example of dynamic and static images in a section with limestone concretions of La Luna Formation.

Image tools are composed of assemblies of pads and electrodes, normally 20 or 24 electrodes per pad. The electrodes measure resistivity simultaneously every 5 mm along the borehole wall; the simple average of these measurements is used as a high-resolution resistivity curve (IMG_Res, Figure 3). This curve is utilized for thin layers analysis and can further be employed for petrophysical evaluations as a shallow resistivity log.

TOTAL GAMMA RAYS (GR)

The resistivity imaging is acquired together with a GR log; this log measures the natural emission of gamma rays from radioactive elements in the formation. In Figure 3, the GR log is presented in track 3 on a linear grid and in API units (American Petroleum Institute). GRs in sedimentary sequences

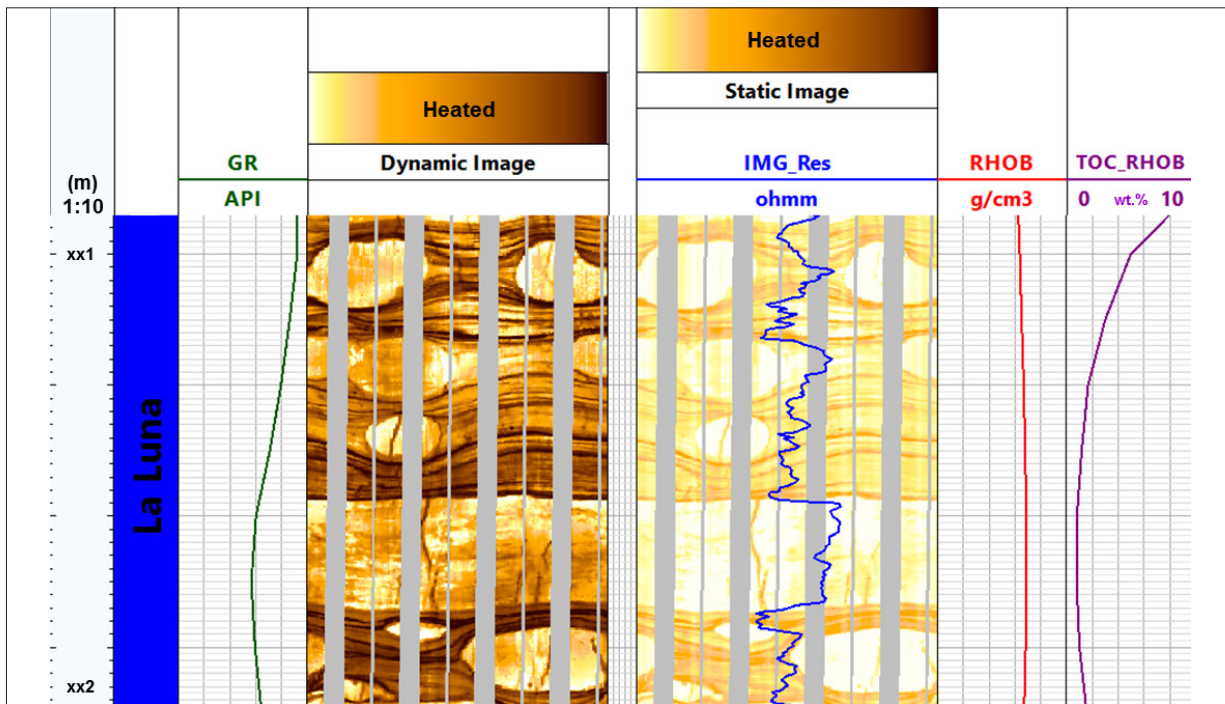


Figure 3. Borehole images (in heated scale), and additional logs employed in this work

are mainly emitted by radioactive elements of the uranium group, thorium group, and potassium. The total GR log gives the radioactivity of the three elements combined (Rider, 2000). Among sedimentary rocks, shales have the strongest radiation, and hence the highest gamma-ray response because of the concentration of radioactive minerals. However, clean sandstone (i.e., with low shale content) might also produce a high gamma-ray response if the sandstone contains potassium feldspars, micas, glauconite, or uranium-rich water (Asquith and Krygowski, 2004). GR log is further applied to identify depth mismatching between logs acquired separately in wells.

BULK DENSITY LOGS

The bulk density (ρ_b or RHOB) is the density of the entire formation as measured by the logging tool in g/cm^3 (Figure 3). This tool has a shallow depth of investigation, and it is held against the borehole during logging to maximize its response. Formation bulk density is a function of rock-matrix density, porosity, and fluid density in the pores; therefore, density log is used to quantify porosity, matrix characterization, and TOC evaluation in unconventional reservoirs. Most of the density tools are comprised of a medium-energy gamma rays source, usually cobalt 60, cesium 137, or in some newer designs, an accelerator-based source (Asquith and Krygowski, 2004).

TARGET OR DEPENDENT VARIABLE

The target or dependent variable refers to the variable to be predicted; in the case of this study this variable is equivalent to the TOC obtained using the equation (1):

$$\text{TOC}_{\text{RHOB}} = 10^{(-15.408 \times \text{RHOB} + 40.569)} \quad (1)$$

Where RHOB represents the bulk density from density logging; equation (1) was found through lab geochemical tests, using a semi-log regression between TOC in core samples against density logging values. TOC in the lab was obtained through oxidation of organic matter in core samples of La Luna Formation. Equation (1) provides a precise procedure when TOC contents need to be known from wireline logs (TOC_RHOB in Figure 3).

FRACTAL PROCESSING

FRACTALS

Benoit Mandelbrot coined the term fractal in 1975, from Latin fractus or irregular. Fractals refer to objects generated by process of repetition, characterized by having details in any observed scale, infinite length, and fractional dimension. Fractal analysis is a well-established scientific method to study natural or artificial objects that have characteristics of repetition in some form (Mandelbrot, 1983). In a statistical sense, fractals are inherent in geology domains like stratigraphy, geochemistry, and fractured rock systems; based on this property some authors have proposed the use of fractals to describe regular patterns in these domains (Schlager, 2004; Park *et al.*, 2010; Sadeghi *et al.*, 2014; Ayad *et al.*, 2019). Additionally, borehole logs represent variations in rock physical properties along the wells, and it has been documented that they can also be described through fractal parameters (Vivas, 1992; Turcotte, 1997; Arizabalo *et al.*, 2006; Leal *et al.*, 2016, Leal *et al.*, 2018).

Like any other image, fractality of a resistivity image can be evaluated through its lacunarity and fractal dimension; both parameters computed after converting the image into binary (black and white). In addition to lacunarity and fractal dimension, multifractal processing of grayscale images can provide further measurements of dimension. From these analyses can be extracted variables or attributes that can later be employed as independent variables to train and feed a machine learning regression model.

LACUNARITY

Lacunarity analysis is a method for describing patterns of spatial dispersion. It can be used with both binary and quantitative data in one, two, and three dimensions. Although originally developed for fractal objects, the method can be used to describe nonfractal and multifractal patterns (Plotnick *et al.*, 1996). Lacunarity can be considered as a measure of the relationship between not filled spaces in images. According to Quan *et al.*, (2014), low lacunarity indicates homogeneous objects; whereas objects of high lacunarity are related to heterogeneous spaces. Allain and Cloitre (1991) proposed a method to compute the lacunarity of binary images using a gliding-box based algorithm, summarized as follows:

- Take an image of side $M \times M$ (e.g., an image of 300 pixels large by 300 pixels width), and place a box of size $r \times r$ in the upper left corner (with $r < M$).
- Count the number of black pixels in the box (box mass).
- Move the box one pixel to the right and calculate the new box mass.
- Repeat this process for all possible boxes over all columns and rows of the image matrix.
- The number of gliding boxes of size r containing P occupied sites is taken as $n(P,r)$, and the total number of gliding boxes of size r is taken as $N(r)$; being M the matrix size in the equation (2):

$$N(r)=(M-r+1)^2 \tag{2}$$

- The gliding-box masses frequency distribution can be converted into a function by dividing the gliding box count by the total number of gliding boxes. As shown the function $Q(P,r)$ in the equation (3):

$$Q(P, r)=\frac{n(P,r)}{N(r)} \tag{3}$$

- The first $Z^{(1)}$ and the second $Z^{(2)}$ moments of this distribution can be calculated employing the equations (4) and (5), respectively:

$$Z^{(1)} = \sum PQ(P,r) \tag{4}$$

$$Z^{(2)} = \sum P^2Q(P,r) \tag{5}$$

- Finally, the lacunarity λ of the image for a gliding box of size $r \times r$ can be computed with the equation (6):

$$\lambda_r = \frac{Z^{(2)}}{(Z^{(1)})^2} \quad (6)$$

FRACTAL DIMENSION

Fractal dimension (FD) is an effective measure for complex objects (Li *et al.*, 2006), representing the space-filling capacity of a pattern. The FD quantifies a subjective feeling about how densely the object occupies the metric space in which it lies (Barnsley, 1993). A method to estimate FD of binary images is the box-counting algorithm; the detailed procedure can be described as follows:

- The study image must be inserted in a box of side r .
- This box should be divided into four boxes with side $r/2$, and the number of boxes covering any part of the figure $N(r)$ must be counted.
- Resulted boxes are divided again into four boxes, and the number of boxes $N(r)$ containing any part of the figure must be recounted.
- The procedure is repeated, counting the number of boxes with some part of the figure.
- Afterward, plot the inverse of box size against the number of boxes with any part of the figure, with the X_j axis equal to $\text{Log}(1/r_j)$ and Y_j axis equal to $\text{Log}(N_j)$.
- Finally, the slope m of the regression is the FD of the image computed with the equation (7):

$$m = \frac{n \sum_1^n X_j Y_j - \left(\sum_1^n X_j\right) \left(\sum_1^n Y_j\right)}{n \sum_1^n X_j^2 - \left(\sum_1^n X_j\right)^2} \quad (7)$$

MULTIFRACTAL ANALYSIS

Multifractal analysis has been recognized as a powerful tool for characterizing textures in images. Several studies have shown the possibilities offered by multifractal analysis in image processing, particularly during classification of complex textures (Harrar and Khider, 2014). In this work multifractal analysis was applied to grayscale images, following the methodology proposed by Huang and Chen (2018). These authors propose to extract a set of features to characterize the image considering global (in the whole image) and local parameters (just in a part of the image). The global parameters provide the capacity dimension, information dimension, and correlation dimension; whereas local parameters provide the singularity exponent and a local fractal dimension, this last in a section of the image.

INDEPENDENT VARIABLES GENERATED BY FRACTAL PROCESSING

The independent variables refer to the required data to train and feed a predictive model; initially, a total of 49 independent variables are available for these tasks. Forty-seven of them are related to fractal variables, and the two remaining are the GR and IMG_Res, respectively. Fractal-related variables were computed using the dynamic image, employing images that represent borehole sections of 0.6 m high and 21.59 cm in diameter; these dimensions are represented with images of 300 pixels

high by 360 pixels width (360° around borehole circumference). Calculations were made on the dynamic image every 300 pixels from bottom to top to create a log per each variable.

Fractal variables were defined according to their relations with lacunarity, fractal dimension, and multifractal analysis. For lacunarity, a group of variables was derived from the frequency distribution produced by calculating lacunarity using different r values. The rest of the lacunarity-related variables were computed using the geometric and statistical descriptions of patterns in scatter plots of lacunarity versus r ; the scatter plots were for both linear and logarithmic scales. The same procedure was applied for FD variables, but in this case, the image size was varied to perform the frequency distribution and scatter plots. To evaluate the spectra of lacunarity, FD, and the geometrical relation between them, a total of 15 values of r and 15 image sizes were experimentally selected. Two important reasons to highlight for this selection:

- As the image size and r value increase, patterns in both scatter plots and frequency distributions are the same; just changes in slope and correlation coefficient (R) of linear patterns are observed.
- The gliding-box and box-counting algorithms are a pixel-by-pixel review of a matrix; consequently, these processes with large gliding boxes or large images are computationally expensive. In other words, it will increase computation time resulting in no practical procedures.

VARIABLES OBTAINED FROM LACUNARITY PROCESSING

- Variable 1: The image sections of 300×360 were transformed into sections of 300×300 (with size in pixels, and using morphologic transformation of image processing techniques). Then, the lacunarity was computed using the gliding-box algorithm (Allain and Cloitre, 1991), with $r = 60$ pixels. This procedure was applied over the dynamic image every 0.6 m along the well.
- Variables 2-10: As shown the Figure 4, these variables represent the statistical description of lacunarity using several r values (r in pixels, Figure 4).
- Variables 11-22: These variables are computed using the scatter plot of Lacunarity vs r . Figure 5A for a log scale (Var. 11-16), and Figure 5B for a linear scale (Var. 17-22).

VARIABLES OBTAINED FROM FD PROCESSING

- Variable 23: As in the case of Variable 1, the image sections were transformed into arrays of 300×300 , and FD was computed using the dynamic image every 0.6 m employing the box-counting algorithm.
- Variables 24-32: This set of variables is related to the statistical measures of FD distribution. The analyzed section of image was resized according to the sizes in Figure 6.
- Variables 33-40: These variables are computed using the scatter plot of FD vs. Image Size. Figure 7A for a log scale (Var. 33 and 34), and Figure 7B for a linear scale (Var. 35-40).
- Variables 41-42: These variables are extracted from the scatter plot of FD vs. Lacunarity, as shown the Figure 8.

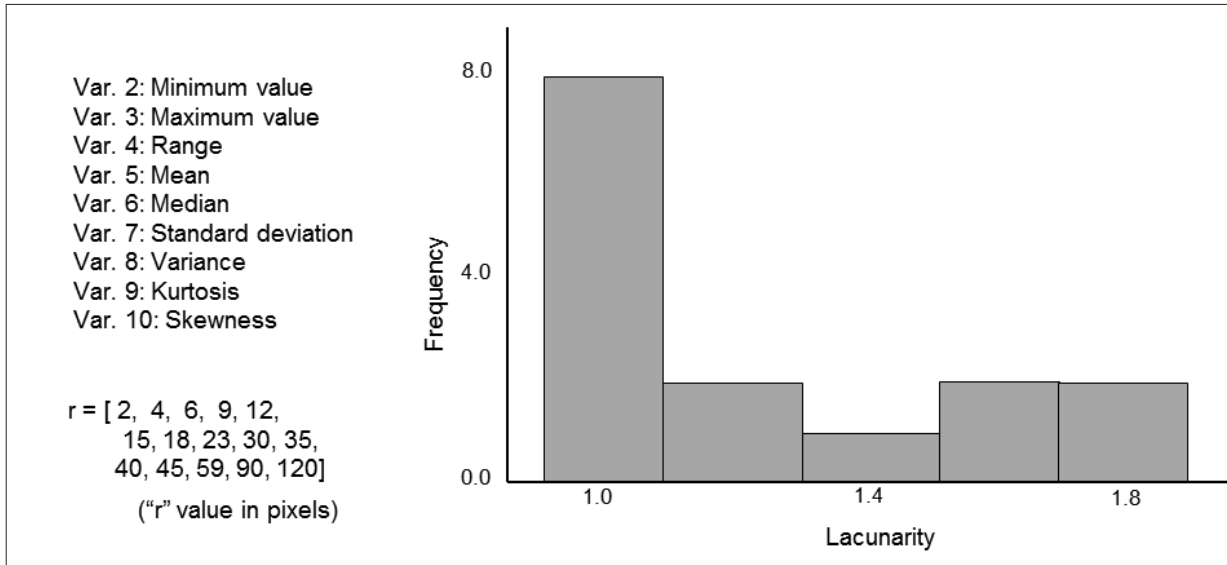


Figure 4. Frequency distribution – Lacunarity

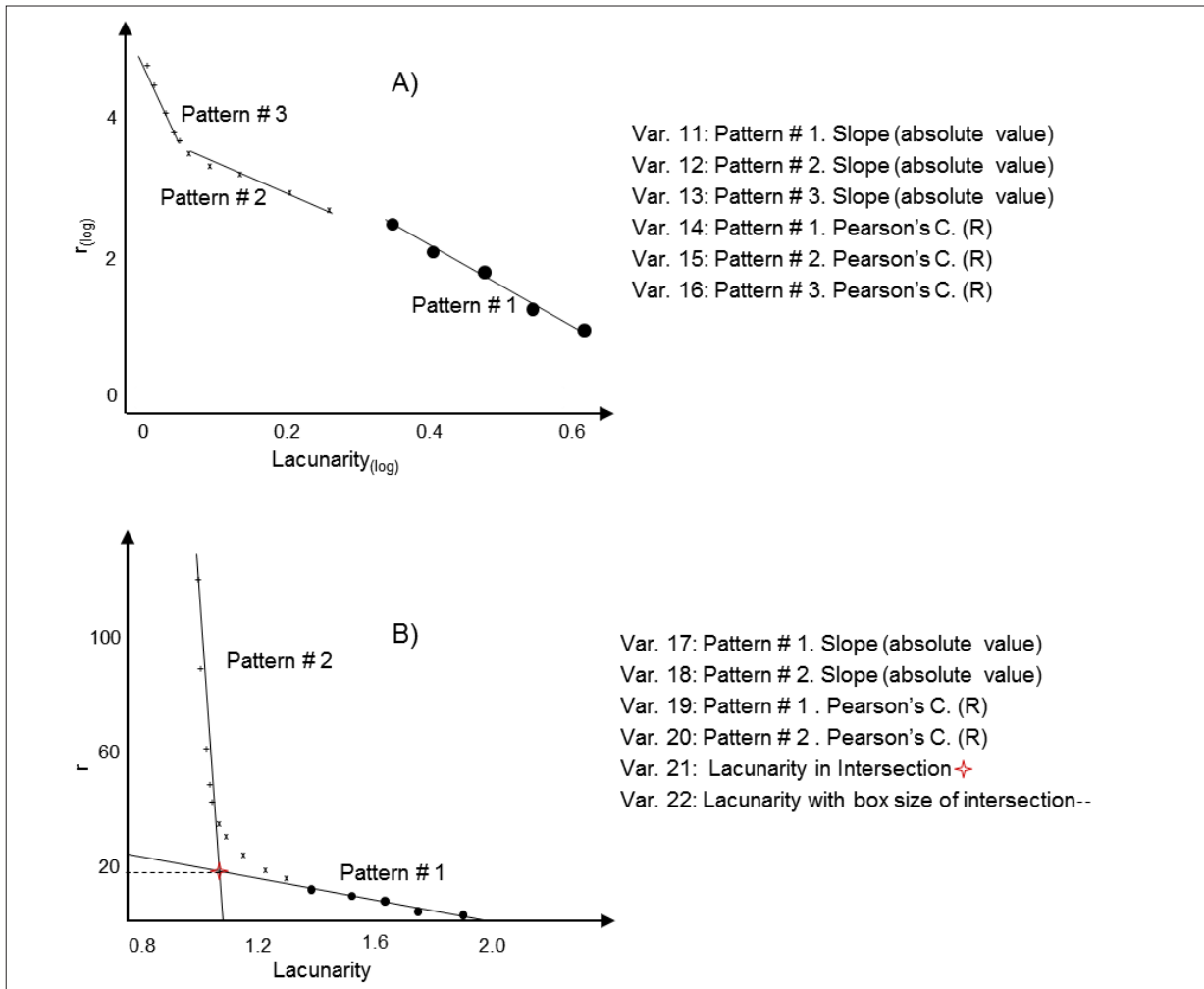


Figure 5. Lacunarity Vs r (Gliding Box Size)

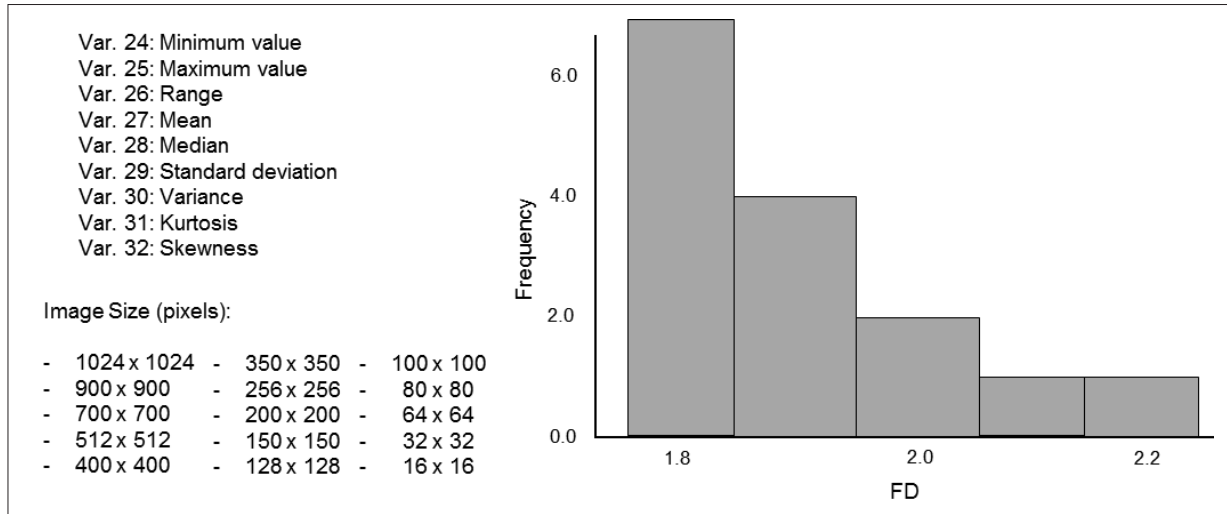


Figure 6. Frequency distribution - Fractal dimension (FD)

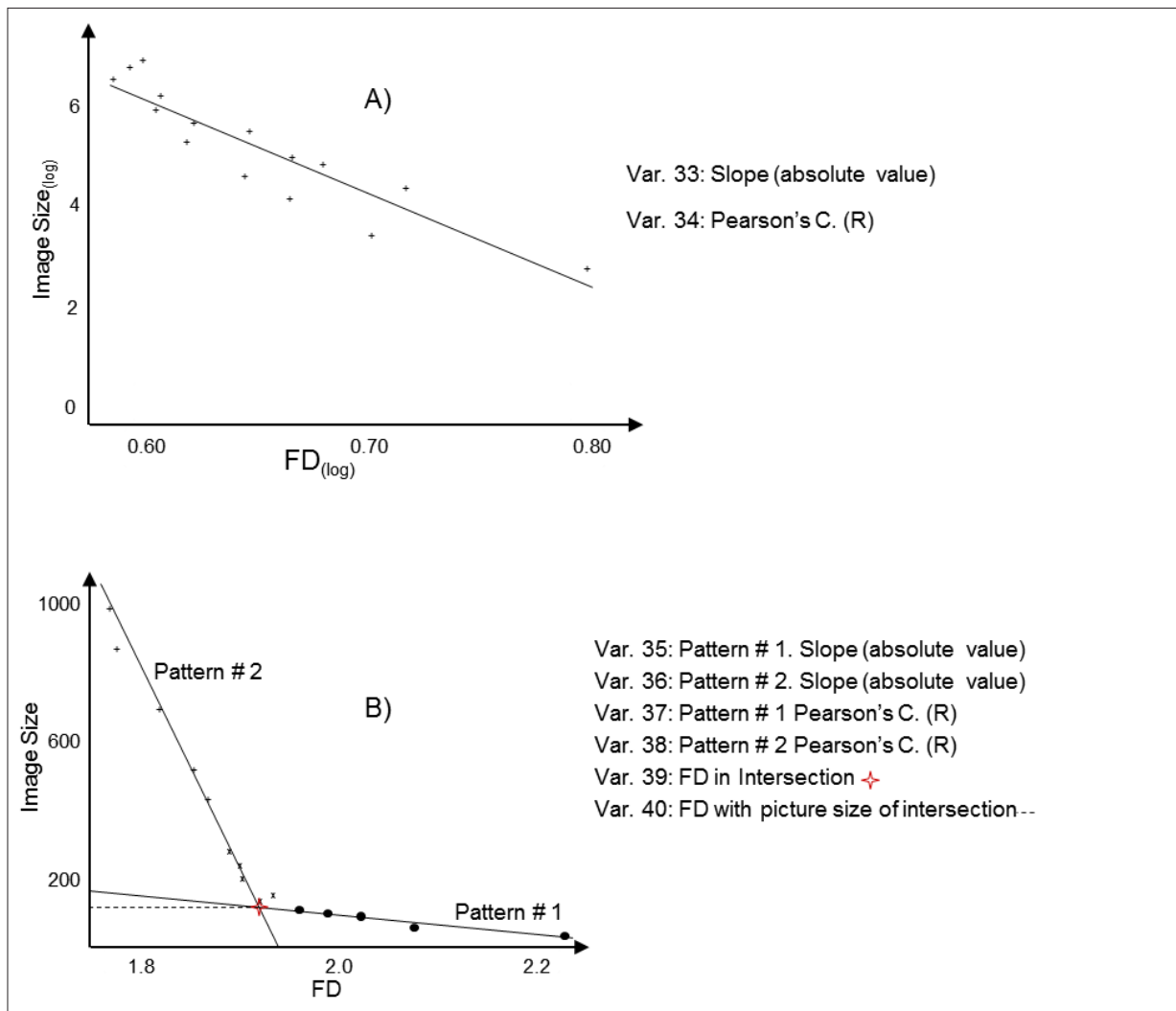


Figure 7. FD Vs Image Size

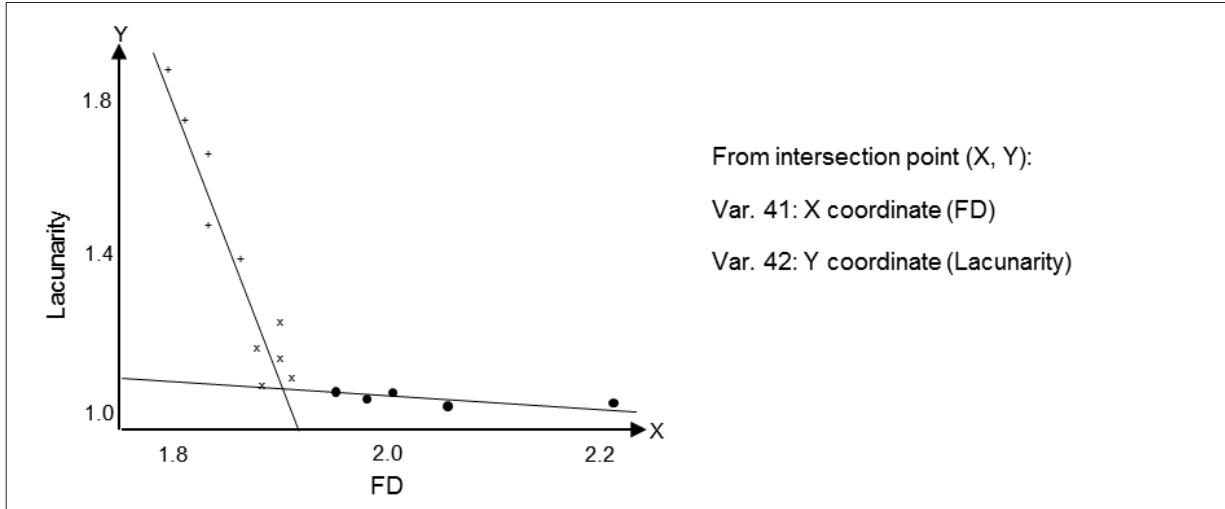


Figure 8. FD Vs Lacunarity

VARIABLES OBTAINED FROM MULTIFRACTAL PROCESSING

To compute variables between 43 and 47, image sections were transformed into arrays of 300×300 (like variables 1 and 23); then, they were converted from the heated scale into grayscale images. Afterward, multifractal variables were calculated every 0.6 m along the well, according to the methodology proposed by Huang and Chen (2018); these variables are described as:

- Variable 43: capacity dimension
- Variable 44: information dimension
- Variable 45: correlation dimension
- Variable 46: singularity exponent
- Variable 47: local fractal dimension

RANDOM FOREST

Random forest (RF) is one of the most powerful algorithms of machine learning available today. The RF is a kind of supervised learning algorithm; it uses labeled data to learn how to classify unlabeled data (Schott, 2019). This method is further categorized as an ensemble learning algorithm, due to it trains a group of decision trees and searches for the best answer among a random subset of features (Geron, 2019). A decision tree consists of just tests on features in the decision nodes, values of features on the branches, and output values on the leaf nodes (Russell and Norvig, 2010); leaf nodes are the answer or solution provided by the algorithm (Figure 9). The RF can be applied for regression and classification problems, and its processing is fast compared with other machine learning techniques; moreover, the algorithm can easily handle outliers and missing data. Common hyperparameters to be tuned in RF are the number of trees, maximum depth, and minimum samples leaf (Figure 9).

Among the RF advantages applicable to this works, and considering we are dealing with just 960 log measurements, is that RF is based on the bagging algorithm and uses ensemble learning. It creates

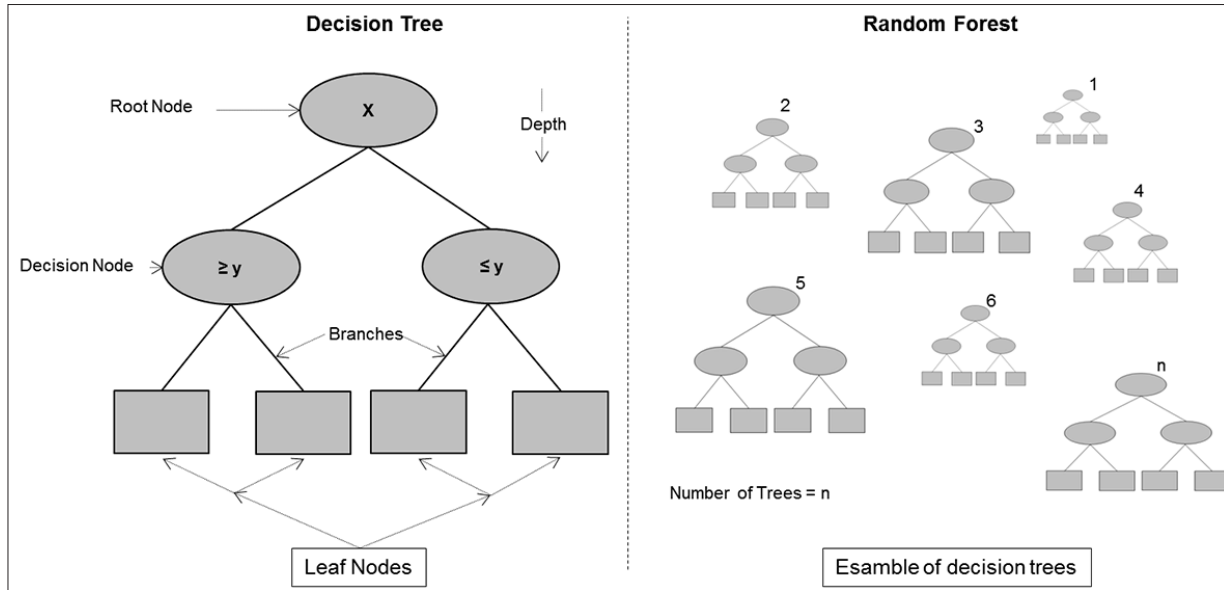


Figure 9. Diagrams of decision tree and random forest

many trees on the subset of the data and combines the output of all the trees. In this way, it reduces the overfitting problem, reduces the variance, and therefore improves the accuracy; even with a low number of samples (Kumar, 2019). Moreover, no feature scaling is required (standardization and normalization) because it uses a rule-based approach instead of distance calculation. As the main drawback, this method requires much computational power and resources during training, as it builds numerous trees to combine their outputs. However, the relatively low number of samples employed in this work helps to cope with this issue.

The accuracy of the RF was measured using Pearson’s correlation coefficient and the root-mean-square error, both metrics after comparing predicted and actual values. Additionally, the distribution of residual error was employed to evaluate performance.

PEARSON’S CORRELATION COEFFICIENT (R)

Pearson’s correlation coefficient (R) measures the strength of linear association between two variables. The coefficient is measured on a scale with no units and can take a value from -1 to +1. If the sign of R is positive, then a positive correlation exists; otherwise, exists a negative correlation (Sedgwick, 2012). Given a pair of random variables (x,y), R is obtained using the equation (8):

$$R_{(x,y)} = \frac{\text{cov}(x,y)}{\sigma_x \sigma_y} \tag{8}$$

Where cov represents covariance, σ_x and σ_y are the standard deviation of x and y, respectively.

ROOT-MEAN-SQUARE ERROR

The root-mean-square error (RMSE) is widely employed to calculate the error in a set of predictions. The metric is sometimes called mean square error or MSE, dropping the root part from the

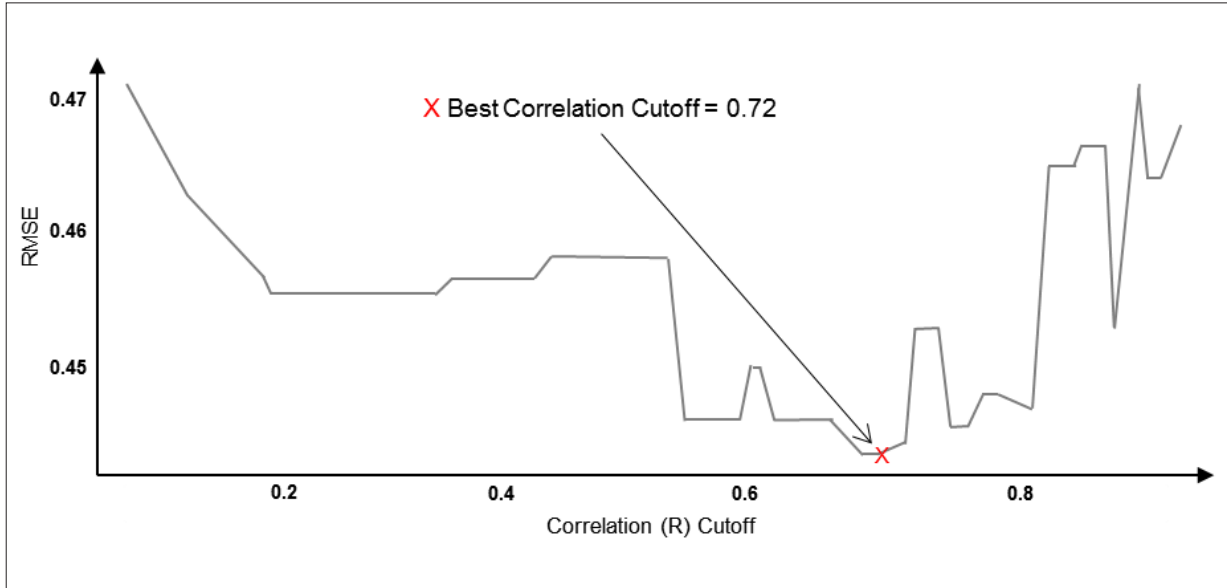


Figure 10. Correlation Cutoff Vs RMSE

calculation and the name. RMSE is calculated as the square root of the mean of the square differences between actual outcomes and predictions. Squaring each error forces the values to be positive, and the square root returns the error metric to the original units for comparison (Brownlee, 2017). The RMSE of predicted values \hat{y}_i , for samples i of dependent variables y_i with n number of observations, is computed with the equation (9):

$$RMSE = \sqrt{\frac{\sum_{i=1}^n (\hat{y}_i - y_i)^2}{n}} \quad (9)$$

FEATURE SELECTION.

Some of the fractal variables may be providing the same kind of information to the predictive model. This duplication can increase the processing time because of high dimensionality. R is used to know the linear relationship between variables or how similar two features are; therefore, when two variables have a high correlation, one of them can be dropped from the model. In order to perform correlation analysis between variables, a cutoff must be established, and following randomly remove one of the variables with a high correlation above this cutoff.

A total of 99 RF models were executed, ranging R from 0.1 to 0.99 and removing a variable every iteration. The RMSE of each result was plotted against R, showing that the lowest RMSE corresponds to a cutoff of 0.72 (Figure 10); by applying this procedure, 32 independent variables were removed.

FEATURE IMPORTANCE.

Another quality of RF is that it makes it easier to measure the relative importance of each variable concerning the target (Geron, 2019). RF performs feature selection when it splits nodes on the most important variables. In this study, feature importance is used to decrease even more the number of

independent variables and keep only the most relevant features. Extra variables can decrease performance, because they may confuse the model by giving it irrelevant data (Koehrsen, 2018).

The feature importance function was first executed to know the ranking of the remaining independent variables. Following, 16 RF models were tested to select the set of variables that produce the lowest RMSE. The less important variable was removed in each iteration, in a similar way that previous feature selection processing; after this procedure, only one variable was removed. Table 1 shows a summary and brief description of the remaining features according to their relative importance. These variables will be the input to the final RF regression model.

RESULTS AND DISCUSSION

After the feature importance review, the doughnut chart in Figure 11 shows the relative importance and amount of information gain provided by each variable to the predictive model. The inner ring shows the percentage of information provided for each fractal analysis; the gamma-ray and average pad resistivity are presented as a whole group in this ring. The outer ring graphically depicts the information provided for each independent variable according to their relation to lacunarity, fractal dimension, and multifractal processing; additionally, this ring shows information provided for the gamma rays and average pad resistivity separately. The exact values of information gain for each variable are presented in the table next to the doughnut chart.

In decision trees, information gain is based on the decrease in entropy after the data set is split on a node; in other words, information gain due to a feature summed across all the levels of decision tree determines its feature importance. This can also be seen from the fact that at every node splitting is done on the feature which maximizes information gain (Singh, 2019). In accordance with Figure 10, the most important independent variable is the gamma rays log (63.3%); this is an expected

Table 1. Summary and description of final independent variables

No.	Selected Variables	Description
1	GR	GR log acquired along with borehole imaging
2	Var. 43	Capacity dimension (Multifractal Analysis)
3	Var. 11	Slope - Pattern # 1 in Figure 5A
4	Var. 9	Kurtosis of lacunarity distribution (Figure 4)
5	IMG_Res	Average resistivity curve computed with pads of image tool
6	Var. 47	Local fractal dimension (Multifractal Analysis)
7	Var. 44	Information dimension (Multifractal Analysis)
8	Var. 15	R - Pattern # 2 in Figure 5A
9	Var. 1	Lacunarity of dynamic image each 0.6 m (r = 60 x 60 pixels)
10	Var. 23	FD of dynamic image each 0.6 m
11	Var. 38	R – Patter # 2 in Figure 7B
12	Var. 40	Fractal dimension using picture size of intersection (Figure 7B)
13	Var. 25	FD maximum value (Figure 6)
14	Var. 33	Slope in Figure 7A
15	Var. 13	Slope - Pattern # 3 in Figure 5A
16	Var. 20	R – Patter # 2 in Figure 5B

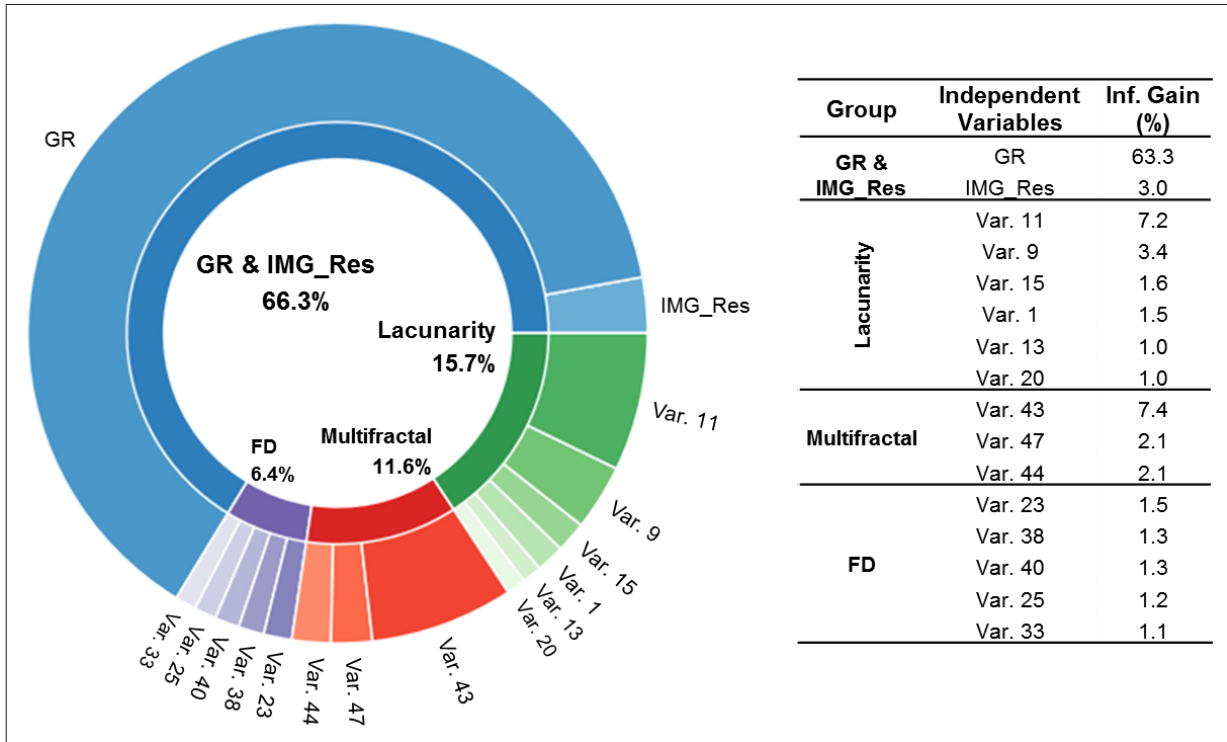


Figure 11. Importance and information gain provided for each independent variable

result and makes geological sense because of the high uranium content in the organic matter of La Luna Formation. The following set of variables is related to lacunarity processing, which is providing 15.7% of information to the regression model.

When a section of a borehole image is binarized, the lacunarity measures relationships between high resistivity spaces in that section of the image. As was seen in the description of La Luna Formation, concretions and calcareous beds are common high resistivity features of this unit; such features appear as white spaces after the image is converted into black and white for lacunarity processing. Another fact to highlight is the amount of hydrocarbon and organic matter in these rocks; organic-rich lithologies produce light tones when borehole imaging is presented using a heated scale. Therefore, image sections in this material will be increasing the number of white pixels after binarization. These statements explain why lacunarity processing plays an important role in pattern recognition in La Luna Formation. Figure 12A shows a linear trend confirming this interpretation; in this example the micronormal resistivity log (MNRL) was compared against the variable 11 (the most important lacunarity variable).

On the other hand, multifractal analysis is employed in this work to identify patterns in the transition from white to black or vice versa; being the capacity dimension the most important variable of this set (Var 43 with 7.4% of information gain). The capacity dimension is part of the global parameters used to describe spatial complexity, reflecting features from an overall perspective (Huang and Chen, 2018). This dimension is likewise computed using the box-counting algorithm, but in this case, the intercept is fixed to zero to avoid values greater than 2 (abnormal values). The capacity dimension is bound to be greater than the information dimension and both greater than the correlation dimension; in this work, that condition is accomplished along all logged sections. The main observations to point out about the capacity and information dimensions are the linear trends

presented in Figures 12B-12C. Negative slopes in these figures suggest that multifractal parameters are complementing the information provided by lacunarity in a contrary direction, in other terms, they are related to conductivity. Multifractal parameters are describing patterns in not-resistive shelly sections or other conductive structures in the borehole image.

Finally, similar to multifractal parameters, the FD processes are related to conductive features; Figure 12D shows a negative slope supporting this interpretation. Likewise, this is an expected result because FD was computed using the box-counting algorithm, but without fixing the intercept to zero. It is important to notice that information provided by FD processes is not duplicating the information provided by multifractal variables. According to feature selection processing, these groups of variables are statistically different; the main reason is that FD was computed using binary images instead of grayscale images as in the case of multifractal processing.

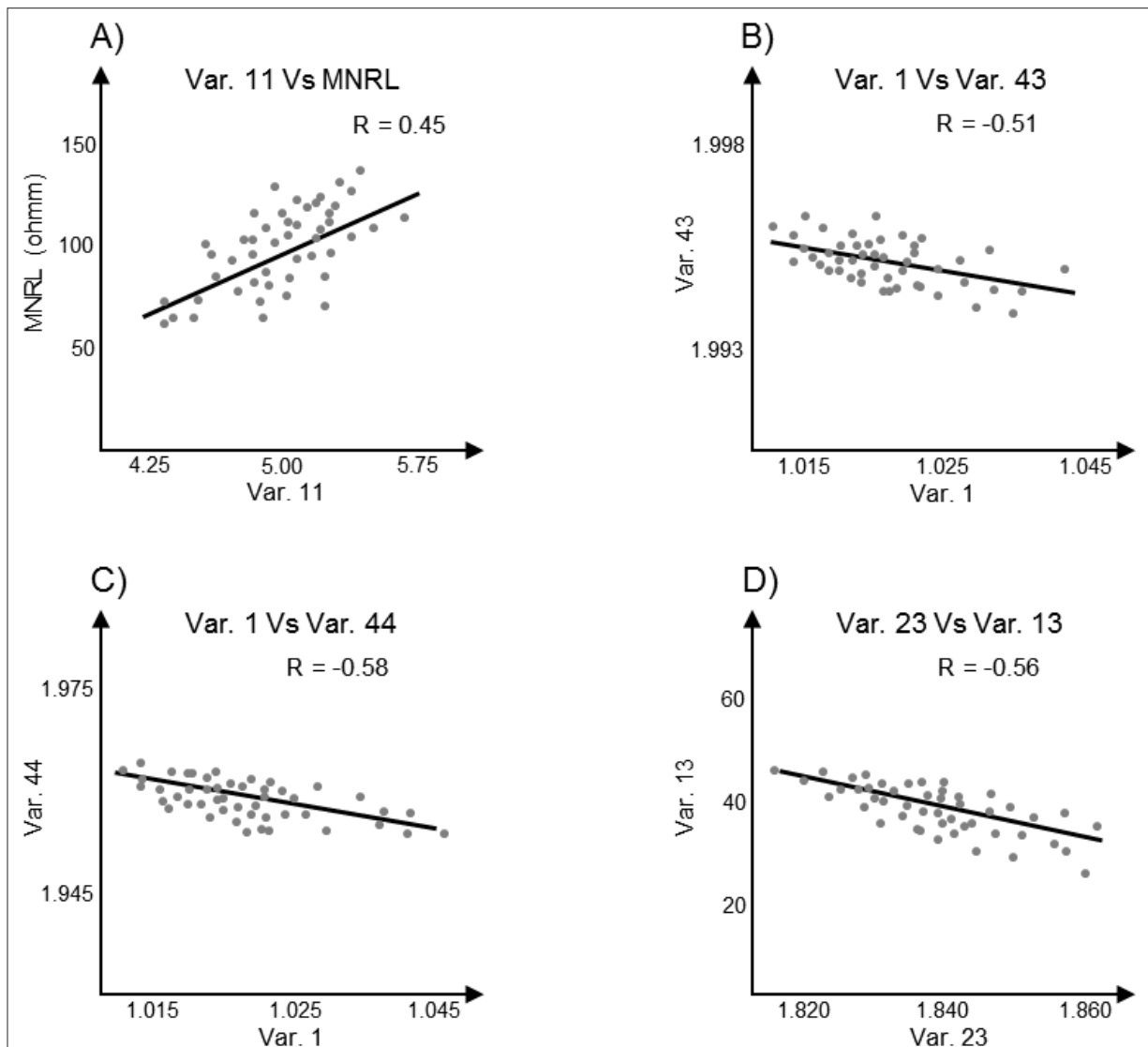


Figure 12. A) Shows a linear trend between Var. 11 (related to lacunarity) and a micronormal resistivity log (MNRL). B), C), and D) likewise show linear trends between several high-ranked independent variables related to conductivity in borehole imaging.

Once all required independent variables are identified, the hyperparameters for the RF predictor must be established. In this study, the model hyperparameters were tuned using a grid-searching approach. Grid-searching is the process of scanning the data to configure optimal hyperparameters for a given model. Grid-searching builds a model on each hyperparameter combination provided and stores a model for each combination (Lutins, 2017). The grid-searching shows an optimal hyperparameters combination of 140 trees with a maximum depth of 35 levels and minimum samples leaf of 1. Lastly, with the optimal hyperparameters already established, the RF model was executed using the test data set, composed of 192 unseen samples. The final performance showed an R of 0.88 and RMSE of 0.44 %, as indicated by the regression in Figure 13A.

According to the central limit theorem, the residual error of a regression model must follow a normal distribution with constant variance and zero means (Martin *et al.*, 2017). The residual error pro-

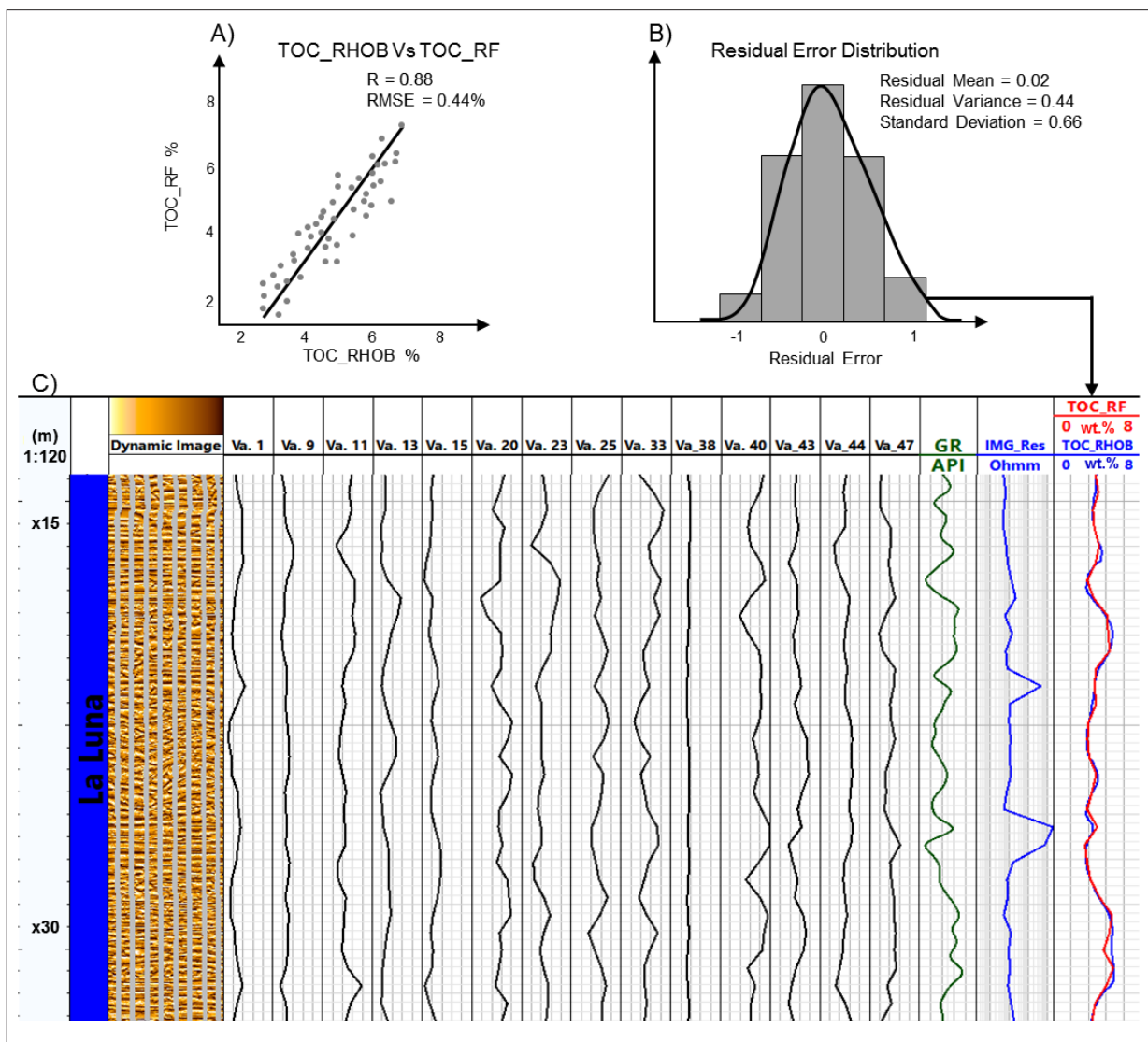


Figure 13. A) Scatter plot (TOC_RHOB Vs. TOC_RF); B) residual error distribution, and C) example of a composite log with borehole dynamic imaging, the RF input variables, and comparison between the final result (TOC_RF) and actual TOC data (TOC_RHOB).

duced by the RF model in this work presents a normal distribution as shown the Figure 13B, with a mean of 0.02 and a variance of 0.44 (equivalent to RMSE). Figure 13C shows a graphic example of input variables, dynamic image, and TOC curves (TOC_RF from the regression model and TOC_RHOB from the density log).

In order to compare the outcome of this works with other methods commonly applied to compute TOC using borehole logs, the standard deviation value is utilized. Schmoker and Hester (1983) reported an average standard deviation of 2.7 wt.% in 266 analyzed samples; these samples come from the upper and lower member of the Bakken Formation in the Williston Basin of North America. In another hand, Passey *et al.* (1990) reported an average standard deviation of 1.2 wt.% in 112 analyzed samples, coming from six wells drilled in organic-rich lithologies in clastic and carbonate environments. Figure 13B presents a lower standard deviation compared with these works (0.66 wt.%), which can be interpreted as less dispersion in the final results. This finding along with the R and RMSE previously explained confirms that this result can be employed during TOC evaluation in La Luna Formation.

CONCLUSIONS

The methodology presented in this research provides an alternative to evaluating TOC content soon after the image log is acquired. Only a dynamic normalized image, the total gamma rays, average pad resistivity, and fractal variables derived from image pixels are required for the entire processing. This RF predictor presents RMSE less than 0.5%, about the TOC obtained through the equation (1); furthermore, this procedure shows a lower standard deviation compared with the most common methods applied when TOC content needs to be assessed from borehole logs.

The performance of this method is sensitive to image quality, and therefore quality control of imaging data is recommended. Wireline imaging tools are based on several kinds of pad/flap configurations, and their proper operability will depend on the pad's contact with the formation. In this sense, irregular borehole sections (e.g., with breakout or washout) will produce poor-quality images, which increases the RMSE of estimated values.

The presented model was developed for vertical wells, using resistivity imaging acquired with wireline in water-based mud. Thus, the model must be recalibrated in case it is used in oil-based mud environments, in deviated or horizontal wells, and when logging while drilling imaging is employed. Further calibrations are required when it is utilized in other unconventional plays different from La Luna Formation; once recalibrated, its results can be used for choosing candidates in hydraulic fracturing programs.

The methodology presented in this work demonstrates that accurate numerical values can be decoded from the intensity of pixels in a set of images. Further research in this field is recommended; this procedure might be applied to estimate any other petrophysics attribute, such as porosity, permeability, resistivity, and saturations, among other variables.

ACKNOWLEDGMENT

The authors would like to thank Universidad Nacional de Colombia for supporting this research.

REFERENCES

- Allain, C., Cloitre, M., 1991, Characterizing the lacunarity of random and deterministic fractal sets. *Physical Review A*, 44(6), 3552–3553. <https://doi.org/10.1103/PhysRevA.44.3552>
- Arizabalo, R., Oleschko, K., Gabor, K., Lozada, M., Castrejón, R., Ronquillo, G., 2006, Lacunarity of geophysical well logs in the Cantarell oil field, Gulf of Mexico. *Geofísica Internacional*, 45(2), 99-105.
- Asquith, G., Krygowski, D., 2004, Basic well log analysis, second edition. The American Association of Petroleum Geologist, Tulsa, 31pp.
- Ao, Y., Li, H., Zhu, L., Ali, S., Yang, Z., 2018, Logging lithology discrimination in the prototype similarity space with random forest. *IEEE Geoscience and Remote Sensing Letters*, 16(5), 687-691. [10.1109/LGRS.2018.2882123](https://doi.org/10.1109/LGRS.2018.2882123).
- Ayad, A., Amrani, M., Bakkali, S., 2019, Quantification of the disturbances of phosphate series using the box-counting method on geoelectrical images (Sidi Chennane, Morocco). *International Journal of Geophysics*, 2019(12), 1-12. <https://doi.org/10.1155/2019/2565430>
- Baraboshkin, E., Ismailova, L., Orlov, D., Zhukovskaya, E., Kalmykov, G., Khotylev, O., Baraboshkin, E.Y., Koroteev, D., 2019, Deep convolutions for in-depth automated rock typing. *Computer and Geosciences*, 135(1), 1-24. <https://doi.org/10.1016/j.cageo.2019.104330>
- Barnsley, M., 1993, Fractals Everywhere, second edition. Morgan Kaufmann, Atlanta, 171pp.
- Bralower, T., Lorente, M., 2003, Paleogeography and stratigraphy of the La Luna Formation and related cretaceous anoxic depositional systems. *PALAIOS* 2003(18), 301-304. [10.1669/0883-1351\(2003\)018<0301:PASOTL>2.0.CO;2](https://doi.org/10.1669/0883-1351(2003)018<0301:PASOTL>2.0.CO;2)
- Brownlee, J., 2016, What is a Confusion Matrix in Machine Learning. Machine Learning Mastery, 18 November 2016, <https://machinelearningmastery.com/confusion-matrix-machine-learning/> (accessed 6 June 2020).
- Brownlee, J., 2017, How to use metrics for deep learning with keras in python. Machine Learning Mastery, 9 August 2017, <https://machinelearningmastery.com/custom-metrics-deep-learning-keras-python/> (accessed 6 June 2020).
- Ceron, M., Walls, J., Diaz, E., 2013, Comparison of reservoir quality from La Luna, Gacheta and Eagle Ford shale formations using digital rock physics. Paper Presented at AAPG International Conference and Exhibition, Cartagena, Colombia, 8-11 September.
- EIA., 2015. Technical recoverable shale oil and shale gas resources: Northern South America. U.S. Department of Energy, Washington, 9pp.
- Escalona, A., Mann, P., 2006, An overview of the petroleum system of Maracaibo Basin. *AAPG Bulletin*, 90(4), 657–678. <https://doi.org/10.1306/10140505038>
- Geron, A., 2019, Hands-on machine learning with Scikit-Learn, Keras, and TensorFlow, second edition. O'Reilly Media Inc., Sebastopol, 177pp.
- González, M., Umaña, R., Guevara, L., Vásquez, M., 2009, Informe Ejecutivo Evaluación del Potencial Hidrocarbúfero de las Cuencas Colombianas. Agencia Nacional de Hidrocarburos, Bogotá, 5pp.

- Guerrero, J., 2002, A proposal on the classification of systems tracts: Application to the allostratigraphy and sequence stratigraphy of the Cretaceous Colombian Basin, Part 2: Barremian to Maastrichtian. *Geología Colombiana*, (27), 27-49.
- Harrar, K., Khider, M., 2014, Texture analysis using multifractal spectrum. *International Journal of Modeling and Optimization*, 4(4), 336-34. 10.7763/IJMO.2014.V4.396
- Huang, L., Chen, Y., 2018, A comparison between two ols-based approaches to estimating urban multifractal parameters. *World Scientific*, 26(1), 1-17. <https://doi.org/10.1142/S0218348X18500196>
- Koehrsen, W., 2018, Improving the Random Forest in Python Part 1. Towards Data Science, 6 January 2018. <https://towardsdatascience.com/improving-random-forest-in-python-part-1-893916666cd> (accessed 10 January 2020).
- Krasnov, F., Glavnov, N., Sitnikov, A., 2017, Application of multidimensional interpolation and random forest regression to enhanced oil recovery modeling, in 13th Central & Eastern European Software Engineering Conference, Russia, 2-4 October. <https://doi.org/10.1145/3166094.3166096>
- Kumar, N., 2019, Advantages and Disadvantages of Random Forest Algorithm in Machine Learning. The Professionals Point, 23 February 2019, <http://theprofessionalspoint.blogspot.com/2019/02/advantages-and-disadvantages-of-random.html#:~:text=Random%20Forest%20is%20based%20on,and%20therefore%20improves%20the%20accuracy.> (accessed 30 May 2022).
- Leal, J., Ochoa, L., Contreras, C., 2018, Automatic identification of calcareous lithologies using support vector machines, borehole logs and fractal dimension of borehole electrical imaging. *Earth Sciences Research Journal*, 22(2), 75-82. <https://doi.org/10.15446/esrj.v22n2.68320>
- Leal, J., Ochoa, L., Garcia, G., 2016, Identification of natural fractures using resistive image logs, fractal dimension and support vector machines. *Ingeniería e Investigación*, 36(3), 125-132. <https://doi.org/10.15446/ing.investig.v36n3.56198>
- Li, J., Sun, C., Du, Q., 2006, A new box-counting method for estimation of image fractal dimension. *International Conference on Image Processing*, 2006, 3029-3032. DOI: 10.1109/ICIP.2006.313005.
- Liborius, A., Slatt, R., 2014, Geological characterization of La Luna Formation as an unconventional resource in Lago De Maracaibo Basin, Venezuela, in 4th Unconventional Resources Technology Conference, The United States Of America, 25-27 August. <https://doi.org/10.15530/urtec-2016-2461968>
- Lutins, E., 2017, Grid searching in machine learning: Quick explanation and python implementation. Medium, 5 September 2017, <https://medium.com/@elutins/grid-searching-in-machine-learning-quick-explanation-and-python-implementation-550552200596> (accessed 5 June 2020).
- Mandelbrot, B., 1983, The Fractal Geometry of Nature, second edition. W. H. Freeman and Company, New York, 14pp.
- Martin, J., Ruiz de Adana, D., Asuero, A., 2017, Fitting models to data: Residual analysis, a primer. *Intech*, 7(1), 133-140. <https://doi.org/10.5772/68049>
- Park, S., Kim, Y., Ryoo, C. Sanderson, D., 2010, Fractal analysis of the evolution of a fracture network in a granite outcrop, SE Korea. *Geosciences Journal*, 14(1), 201-215. <https://doi.org/10.1007/s12303-010-0019-z>

- Passey, Q., Creaney, S., Kulla, J., Moretti, F., Stroud J., 1990, A practical model for organic richness from porosity and resistivity logs. *AAPG Bulletin*, 74(12), 1777-1794.
- Plotnick, R., Garner, R., Hargrove, W., Prestegard, K., Perlmutter, M., 1996, Lacunarity analysis: A general technique for the analysis of spatial patterns. *Physical Review E*, 53(5461), 5461-5468. <https://doi.org/10.1103/PhysRevE.53.5461>
- Quan, Y., Xu, Y., Sun, Y., Luo, Y., 2014, Lacunarity analysis on image patterns for texture classification, in 2014 IEEE Conference on Computer Vision and Pattern Recognition, The United States Of America, 23-28 June. DOI: 10.1109/CVPR.2014.28
- Rider, M., 2000, The geological interpretation of well logs, second edition. Rider – French Consulting Ltd., Sutherland, 67pp.
- Russell, S., Norvig, P., 2010, Artificial intelligence a modern approach, third edition. Prentice Hall, Upper Saddle River, 697pp.
- Sadeghi, B., Madeni, N., Carranza, E., 2014, Combination of geostatistical simulation and fractal modeling for mineral resource classification. *Journal of Geochemical Exploration*, 149(10), 59-73. <http://dx.doi.org/10.1016/j.gexplo.2014.11.007>
- Sarmiento, G., Puentes, J., Sierra, C., 2015, Estratigrafía y petrofacies de la formación La Luna en el sinclinal de Nuevo Mundo, Valle Medio del Magdalena. *Geología Norandina*, 12(4), 21-40.
- Schlager, W., 2004, Fractal nature of stratigraphic sequences. *GeoScience World*, 32(3), 185-188. <https://doi.org/10.1130/G20253.1>
- Schmoker, J., Hester, T., 1983, Organic carbon in Bakken Formation, United States portion of Williston Basin. *AAPG Bulletin*, 67(12), 2165–2174. <https://doi.org/10.1306/AD460931-16F7-11D7-8645000102C1865D>
- Schott, M., 2019, Random forest algorithm for machine learning. Medium, 25 April 2019, <https://medium.com/capital-one-tech/random-forest-algorithm-for-machine-learning-c4b2c8cc9feb> (accessed 10 April 2020).
- Sedgwick, P., 2012, Pearson's correlation coefficient. *In Endgames*, 345(5), 1-2. <https://doi.org/10.1136/bmj.e5407>
- Singh, V., 2019, Model-based feature importance. Towards data sciences, 3 January 2019, <https://towardsdatascience.com/model-based-feature-importance-d4f6fb2ad403> (accessed 31 July 2020).
- Steiner, S., Ahsan, S., Raina, I., Dasgupta, S., Lis, G., 2016, Interpreting total organic carbon TOC in source rock oil plays, in 2016 SPE Abu Dhabi International Petroleum Exhibition & Conference, The United Arab Emirates, 7-10 November. <https://doi.org/10.2118/183050-MS>
- Turcotte, D., 1997, Fractal and chaos in geology and geophysics, second edition. Cambridge University, Cambridge, 166pp.
- Vivas, M., 1992, A techniques for inter well description by applying geostatistic and fractal geometry methods to well logs and core data. Doctoral dissertation, University of Oklahoma, 16pp.

<https://doi.org/10.22201/igeof.00167169p.2022.61.4.2203>

Modelling of Residual Gravity Data due to a Near Surface Dyke Structure Using Damped SVD and Marquardt Inverse Methods

Ata Eshaghzadeh^{1*} , Alireza Hajian²

Received: December 8, 2021; accepted: August 16, 2022; published on-line: October 1, 2022.

RESUMEN

En este artículo, se describen dos métodos de modelado inverso basados en la descomposición de valor singular amortiguado (DSVD) como inversor lineal y el algoritmo de optimización de Marquardt como inversor no lineal. El SVD amortiguado resuelve los problemas mal planteados y especifica directamente la contribución de la densidad de la superficie inferior. La inversión de Marquardt estima los parámetros del modelo. La eficiencia de ambos métodos se investiga utilizando los datos de gravedad sintéticos, con y sin ruido aleatorio, según se obtengan los resultados aceptables. Los enfoques introducidos se emplean para la interpretación de un conjunto de datos de gravedad real de Irán. La masa causante de la gravedad en el área de estudio son casi el depósito magmático con un alto porcentaje de dióxido de manganeso donde han penetrado dentro de las fracturas y aproximadamente se han formado las estructuras tabulares. Las estructuras invertidas de ambos métodos son casi correspondientes. El ancho, la extensión y la profundidad evaluados hasta la parte superior e inferior de la estructura enterrada mediante la técnica SVD amortiguada son 15 m, 22 m, 7.5 m y 25 m, respectivamente, y según el algoritmo de Marquardt son 15.8 m, 20.3 m, 9.4 m y 21.9 m, respectivamente. La fuente simulada tiene una tendencia NW-SE con una caída de 38,04 grados.

PALABRAS CLAVE: descomposición amortiguada en valor singular, gravedad y Marquardt

Editorial responsibility: Juan García-Abdeslem

**Corresponding author at eshagh@ut.ac.ir*

¹Department of Geology, Faculty of Sciences, University of Isfahan, Isfahan, Iran

²Department of physics, Najafabad Branch, Islamic Azad University, Najafabad, Iran

ABSTRACT

In this paper, two inverse modeling methods based on the damped singular value decomposition (DSVD) as a linear inverter and Marquardt optimization algorithm as a nonlinear inverter are described. The damped SVD solve the ill-posed problems and specify the subsurface density contribution directly. The Marquardt inversion estimate the model parameters. The efficiency of the both methods is investigated using the synthetic gravity data, with and without random noise, as the acceptable results attained. The introduced approaches are employed for the interpretation of a real gravity data set from Iran. The gravity causative mass in the study area are almost the magmatic deposit with a high percent of the Manganese dioxide where there have penetrated inside of the fractures and have approximately formed the tabular structures. The inverted structures from the both methods are almost corresponding. The evaluated width, extension and depth to the top and bottom for the buried structure via the damped SVD technique are 15 m, 22 m, 7.5 m and 25 m, respectively and by the Marquardt's algorithm are 15.8 m, 20.3 m, 9.4 m and 21.9 m, respectively. The simulated source has a trend NW-SE with a dip of 38.04 degree.

KEY WORDS: damped singular value decomposition (DSVD), gravity and Marquardt

INTRODUCTION

Gravity investigation plays an important role in geological studies and has been used widely over the years for modeling buried geological structures and deposit, especially in mineral reconnaissance projects. The non-uniqueness in the linear inverse problem of gravity, i.e., the existence of a large variety of distribution of subsurface density distribution models that generate a similar gravity effect on measurement plane, makes one to hesitate on the reliability of solution (Skeels, 1947; Parker, 1972). In order to obtain a correct unique solution and to decrease the ambiguities, various researchers have been proposed different algorithms to increase the amount of extracted information from inversion for simulating the geometry of a density distribution related to a known gravity anomaly, such that the proposed model be geologically realistic.

Tsuboi (1983) introduced a simple but effective approach based on the equivalent stratum technique to estimate 3D topography of a density interface. Oldenburg (1974) proved that the Parker's expression could be applied in order to specify the geometry of the density interface from its gravity anomaly. The geological maps and petrophysical data from rock samples were used to constraint the model parameters to realistic values (Farquharson *et al.*, 2008; Williams, 2008; Heincke *et al.*, 2010; Lelièvre *et al.*, 2012; Tschirhart *et al.*, 2013, 2017). Kamm *et al.* (2015) used the petrophysical information conduct a joint inversion of gravity and magnetic data. Ialongo *et al.* (2014) show that there are invariant models in the inversion of gravity and magnetic fields and their derivatives.

Using a joint inversion of multiple data sets can also diminish the nonuniqueness of the inverse problem. examples of joint inversion of gravity and magnetic data are given by, e.g., Zeyen and Pous (1993), Gallardo and Meju (2003), and Pilkington (2006) using deterministic inversion techniques and by Bosch and McGaughey (2001), Bosch *et al.* (2006) and Shamsipour *et al.* (2012) using stochastic methods. Shamsipour *et al.* (2010, 2011, 2012) proposed geostatistical techniques of cokriging and conditional simulation for the separate three-dimensional inversion of gravity and magnetic data respectively, including geological constraints.

One way to eliminate the inherent ambiguity is to propose a geologically sound geometry as the source of the anomalous body with a known density as the start point of the inversion of gravity

anomalies (Chakravarthi and Sundararajan, 2004). Although simple models may not be geologically realistic, they usually are sufficient to analyze sources of many isolated anomalies (Abdelrahman and El-Araby, 1993). The interpretation of a given anomaly aims essentially to estimate the parameters such as shape, depth, radius, thickness and so on. Thus, in this case it is dealt with nonlinear inverse modeling. The many of the proposed nonlinear techniques are based on an initial guess of the geological structure parameters, 1) in the case of least-squares minimization approaches (Gupta, 1983; Lines and Treitel, 1984; Abdelrahman, 1990; Abdelrahman *et al.*, 1991; Asfahani and Tlas, 2007, 2008) 2) different neural networks (Eslam *et al.*, 2001; Osman *et al.*, 2006 and 2007; Al-garni *et al.*, 2013; Eshaghzadeh and Kalantari, 2015; Eshaghzadeh and Hajian, 2018); 3) Continual least squares methods (Abdelrahman and Sharafeldin 1996; Abdelrahman *et al.* 2001, 2001a, 2001b; Essa 2012, 2013); 4) effective quantitative interpretations using the least-squares method based on the analytical expression of simple moving average residual gravity anomalies (Gupta, 1983; Abdelrahman *et al.* 2003, 2007, 2015). Appraisal of the depth and shape of a buried structure from the observed gravity and gravity data is widely used in exploration operations, in methods based on the Fourier transform (Odegard and Berg, 1965; Sharma and Geldart, 1968); Mellin transform (Mohan *et al.* 1986); Walsh transforms techniques (Shaw and Agarwal, 1990); ratio techniques (Hammer, 1977; Abdelrahman *et al.*, 1989; Cooper, 2012; Eshaghzadeh, 2017).

Dyke is a sheet-like geological structure generated from intrusive igneous rock while cut through the strata. Dyke structure has different slopes, thicknesses and lateral dimension extent. Structures that have a higher density contrast than that of their encasing formation as are easily detectable in the residual gravity field maps. Because of existence the important minerals in the igneous rock, such as chromite, magnetite and so on, these tabular structures are among the very considerable exploratory targets in geophysical investigations, especially when based on potential fields methods.

By searching many papers related to our subject it can be found that their focus is on determining the parameters of dyke-like gravity sources (Bastani and Pedersen 2001; Abdelrahman and Essa 2007; Abdelrahman *et al.* 2003, Asfahani and Tlas 2007; Tlas and Asfahani 2011a, b; Cooper 2012, 2014, 2015; Abdelrahman *et al.* 2015) while it can be stated that dyke non-linear inverse modeling from gravity data less has been investigated. Ateya and Takemoto (2002) proposed a gravity inversion modeling across a 2-D dike-like structure. A fast simulated annealing global optimization technique has been proposed by Biswas (2016) to the interpretation of gravity and gravity anomaly over thin sheet-type structure. Biswas *et al.* (2017) also applied a nonlinear optimization method for the determination of dyke-type source parameters based on the calculation of first order horizontal and vertical derivatives of the gravity and gravity anomalies. Peace *et al.* (2018) employed the full tensor gravimetry (FTG) data for 3-D subsurface models of the Budgetell Harbour Stock and associated dykes, Newfoundland, Canada. Abdelfattah *et al.* (2021) performed an integrated analysis based on gravity and seismological data with focusing on the HL seismogenic and volcanic zone in the western shield of Saudi Arabia, which has a complex structure comprises dykes, recent volcanic eruptions, and fault segments of various orientations.

For first one, in this study, we employ the linear inverse modeling technique based on the damped singular value decomposition (DSVD) and using a depth weighting parameter as resolution enhancer and a two-norm (also known as the L2 norm or least squares) as stopping criteria in inversion algorithms. SVD constitutes a famous and numerically stable method for analyzing the underdetermined problems, i.e. ill-condition matrices, and is a standard technique for small inverse problems.

We also develop the Marquardt’s algorithm (1963) for inverting the 2-D observed gravity anomaly due to finite dyke-shape model in order to evaluate the depth to top, height (the depth to bottom is estimated), width and slope of buried structure. We exemplify the capability of the both methods by a theoretical model with and without a random noise. Finally, these inversion techniques are employed for the interpretation of the real gravity data from Iran.

COMPUTING THE KERNEL MATRIX

For inverting the gravity data for calculating a 2D density distribution, it is necessary that the sub-surface be divided in order to calculate the gravity effect of the obtained density distribution at the surface. For a 2D model, as shown in Figure 1, the gravity effect of all the rectangular blocks at the observation point i , is given by:

$$g_i = \sum_{j=1}^M P_{ij} d_j, \quad i = 1, \dots, N \tag{1}$$

where M and N denote the number of blocks and the number of observations, respectively, d_j is the density of the j^{th} block and P_{ij} is matrix of geometric element or kernel matrix which presenting the influence of the j^{th} block on the i^{th} gravity value. In order to calculate the kernel matrix P_{ij} , the gravity response of the 2D prism is based on the equation developed by Last and Kubik (1983):

$$P_{ij} = 2G \begin{bmatrix} \left(x_1 - x_j + \frac{d}{2} \right) \log \left(\frac{r_2 r_3}{r_1 r_4} \right) + d \log \left(\frac{r_4}{r_3} \right) - \\ \left(z_j + \frac{h}{2} \right) (\theta_4 - \theta_2) + \left(z_j - \frac{h}{2} \right) (\theta_3 - \theta_1) \end{bmatrix} \tag{2}$$

where

$$r_1^2 = \left(z_j - \frac{h}{2} \right)^2 + \left(x_1 - x_j + \frac{d}{2} \right)^2$$

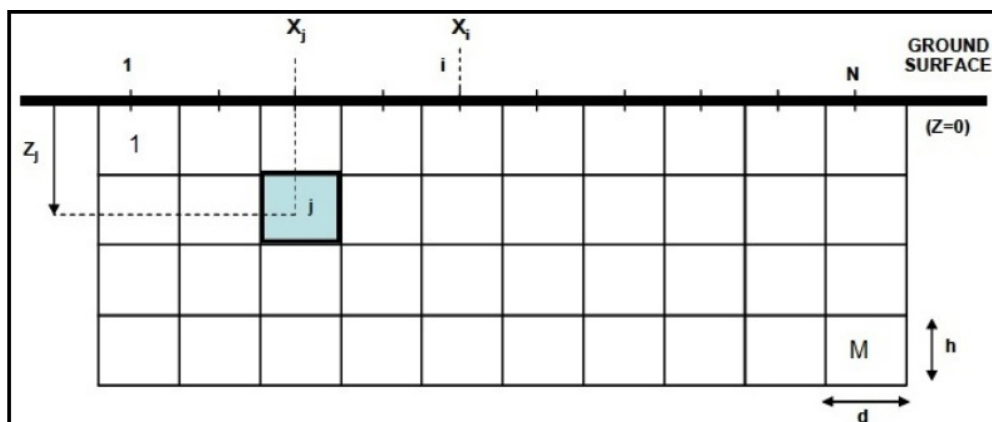


Figure 1. A 2-D schematic view of the inversion domain divided into several blocks as the gravity stations are located at the center of the blocks at the ground surface.

$$r_2^2 = \left(z_j - \frac{h}{2}\right)^2 + \left(x_1 - x_j + \frac{d}{2}\right)^2$$

$$r_3^2 = \left(z_j - \frac{h}{2}\right)^2 + \left(x_1 - x_j + \frac{d}{2}\right)^2$$

$$r_4^2 = \left(z_j - \frac{h}{2}\right)^2 + \left(x_1 - x_j + \frac{d}{2}\right)^2$$

and

$$\theta_1 = \tan^{-1} \left(x_i - x_j + \frac{d}{2}\right) / \left(z_j - \frac{h}{2}\right),$$

$$\theta_2 = \tan^{-1} \left(x_i - x_j + \frac{d}{2}\right) / \left(z_j - \frac{h}{2}\right),$$

$$\theta_3 = \tan^{-1} \left(x_i - x_j + \frac{d}{2}\right) / \left(z_j - \frac{h}{2}\right),$$

$$\theta_4 = \tan^{-1} \left(x_i - x_j + \frac{d}{2}\right) / \left(z_j - \frac{h}{2}\right),$$

Here G is the gravitational constant, d and h are the width and height of each block.

LINEAR INVERSION METHODOLOGY

In most of the inverse modeling cases, we deal with the underdetermined problems, i.e. the number of unknowns is much greater than the number of observed data. For a general underdetermined system of linear equations, i.e. $d=Pf$ where d is the column vector of the observed gravity field data, f is the column vector of the unknown, i.e. density, and P is the kernel rectangular matrix, the minimum norm solution is defined as the model that fits the data exactly which is given by (Menke, 1984):

$$f=P^T(PP^T)^{-1}d \tag{3}$$

we can solve the inversion problem using the standard damped least-squares method, as:

$$f=(P^TP+\gamma I)^{-1}P^Td \tag{4}$$

where γ is the damping parameter or regularization parameter, I is an identity matrix and the superscript T denotes the matrix transposition. The solution of equation (4) can be estimated by minimizing the following Tikhonov cost function:

$$S = \arg \min \{ \|d - Pf\|^2 + \gamma \|f\|^2 \}, \tag{5}$$

Analyzing this expression can be realized that the duty of the damping is minimizing the first term of equation (5) values to finding the model that gives the best fit to the data to Minimize the last

term values to obtain the model with the smallest norm. The choice of γ is usually determined by trial-and-error.

In order to stabilize the inversion, the singular value decomposition (SVD) technique is usually employed. The equation for singular value decomposition of matrix $P_{n \times m}$ is the following:

$$P = USV^T, \tag{6}$$

where S is an $n \times m$ left eigenvector matrix, U is an $n \times n$ diagonal matrix. The elements of $U_{n \times n}$ are only nonzero on the diagonal, and are called the singular values. V^T is also an $m \times m$ right eigenvector matrix and T stands for transpose. Note that $VV^T = V^T V = I_m$ and $UU^T = U^T U = I_n$. The singular values of matrix $P_{n \times m}$ are the positive entries of $U_{n \times n}$ which are distributed in decreasing order along its main diagonal and are equal to positive square roots of the eigenvalues (s_i) of the covariance matrices $P^T P$ & PP^T . P^{-1} and P^T are also, respectively:

$$P^{-1} = (USV^T)^{-1} = U^T S^{-1} V, \tag{7}$$

$$P^T = VSU^T, \tag{8}$$

Therefore, we can rewrite the equation 3 as:

$$(P^{-1}P)^{-1} P^T d = VS^{-2} V^T VSU^T d = VS^{-1} U^T d, \tag{9}$$

The singular value decomposition of matrix $P_{n \times m}$ can be also written as follows:

$$P = \sum_{i=1}^r u_i s_i v_i^T \tag{10}$$

where r is the rank of matrix $P_{n \times m}$, u_i is the i -th eigenvector of covariance matrix PP^T , v_i is the i -th eigenvector of covariance matrix $P^T P$, s_i is the i -th singular value of matrix $P_{n \times m}$ as $s_1 \geq s_2 \geq \dots \geq s_r > 0$, and is an $n \times m$ matrix of unitary rank called the i -th eigenimage of matrix $P_{n \times m}$.

On the basis of equation (10), the damped least-squares solution (equation 4) can be rewritten as the damped SVD, we will have:

$$f = \sum_{i=1}^r k_i \frac{u_i^T d}{s_i} v_i, \tag{11}$$

Here k_i is filter factor defined as

$$k_i = \frac{s_i}{(s_i + \gamma)}, \tag{12}$$

Usually, in the first iteration, the regularization parameter is considered to be a large positive value as at each iteration the damping factor is multiplied by a factor less than unity so that the least-

squares method reaches near a solution (Meju, 1994). According to Arnason and Hersir (1988) the damping factor is determined as follows:

$$\gamma = s_R \Delta d^{\frac{1}{R}}, \quad (13)$$

Where R is the iteration number for the damping factor at any iteration, s is the eigenvalue parameter and the term Δd is given by

$$\Delta d_r = \frac{(d_{r-1} - d_r)}{d_{r-1}}, \quad (14)$$

Where, d_{r-1} is the gravity misfit value obtained at previous iteration and d_r is the misfit computed at the current iteration. For $s_i \gg \gamma$, $k_i \approx 1$, thus it is clear that the components are little influenced by the damping factor and for $s_i \ll \gamma$, $k_i \approx 0$.

In inverting gravity data due to a causative mass, the evaluated density distribution related to a buried structure tend to concentrate near the surface. For nullifying the natural decay of the kernels and maximizing the depth resolution, a depth weighting function is included in the problem. Li and Oldenburg (1998) suggested to employ a depth weighting function such as:

$$w_z = \frac{1}{(z + z_0)} \quad (15)$$

where z is the depth of the layers and z_0 depends on the cell size of the model and the observation height of the gravity data.

In this paper, we employ the two-norm ($L2$ norm) as a criterion for stopping the iteration process in the inversion algorithms. The $L2$ norm has the form:

$$L2 \text{ norm: } \|e\|_2 = \left[\sum_k |e_k|^2 \right]^{1/2} \quad (16)$$

Where the e is the difference between the observed gravity data and inverted gravity data due to the evaluated model from the density distribution at each iteration. The best form of the under surface density distribution is obtained when the $L2$ norm in an iteration achieve the value less than the pre-defined value which in this case the iteration is terminated. Otherwise, the lowest amount estimated by the $L2$ norm during inversion process is considered as the best inverted under surface density distribution.

SYNTHETIC MODEL ANALYSIS WITH DAMPED SVD

Figure 2(a) shows the gravity response due to the assumed model shown in Figure 2(b) where the sub-surface ground has been partitioned into 15×10 prisms with the respective dimensions of $10 \text{ m} \times 5 \text{ m}$. As is shown in Figure 2(b), the 2D model include 6 prisms whose density contrast is 1000 kg/m^3 . The gravity effect corresponding to the resulting inverted causative body (Figure 2c), is displayed in Figure 2(a). This inverted model that is exactly similar to the original causative body, was obtained at 5th iteration, where the $L2$ norm as the stopping criterion attain the smallest amount.

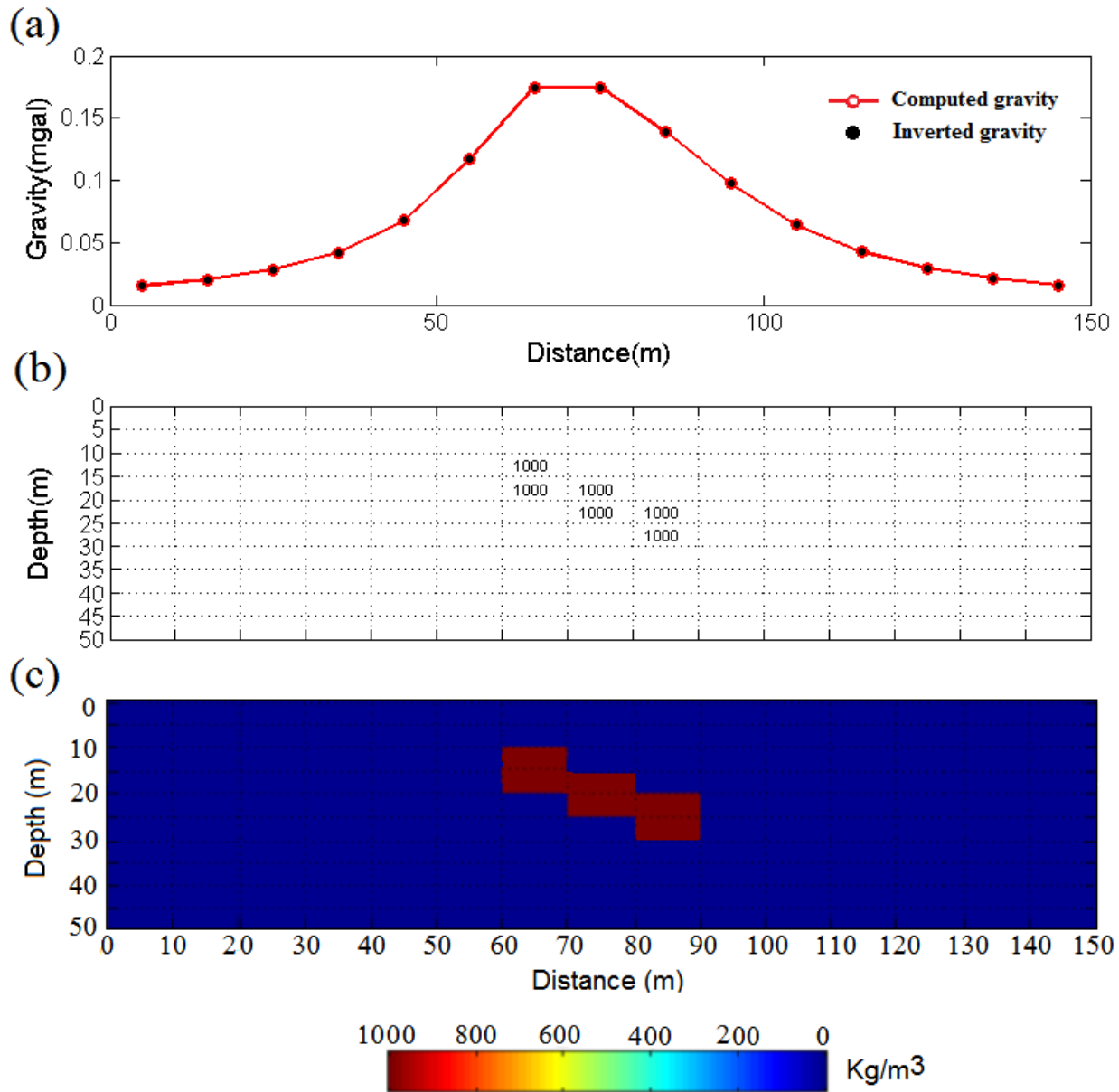


Figure 2. a) Computed and inverted gravity due to b) first assumed synthetic model and c) inverted model, respectively.

For testing the stability and sensitivity of the inversion method, we divided the subsurface inversion domain, Figure 2(b) into 75×25 blocks of dimension $2 \text{ m} \times 2 \text{ m}$ (Figure 3). Therefore, the whole domain is $150 \text{ m} \times 50 \text{ m}$ and the total number of blocks is $M=1875$.

Figure 4 shows the inferred density distribution from inverse modeling. The effect of error has been studied by adding 5% of random noise to the gravity response of the model shown in Figure 3. The inversion result is presented in Figure 5. These inverted models, i.e. figures 4 and 5, accrue at 7th and 10th iterations, respectively. Since, the inverted structures in both cases, with and without noise, are close to that of the assumed model, it can be concluded that the damped SVD inversion provides satisfactory results.

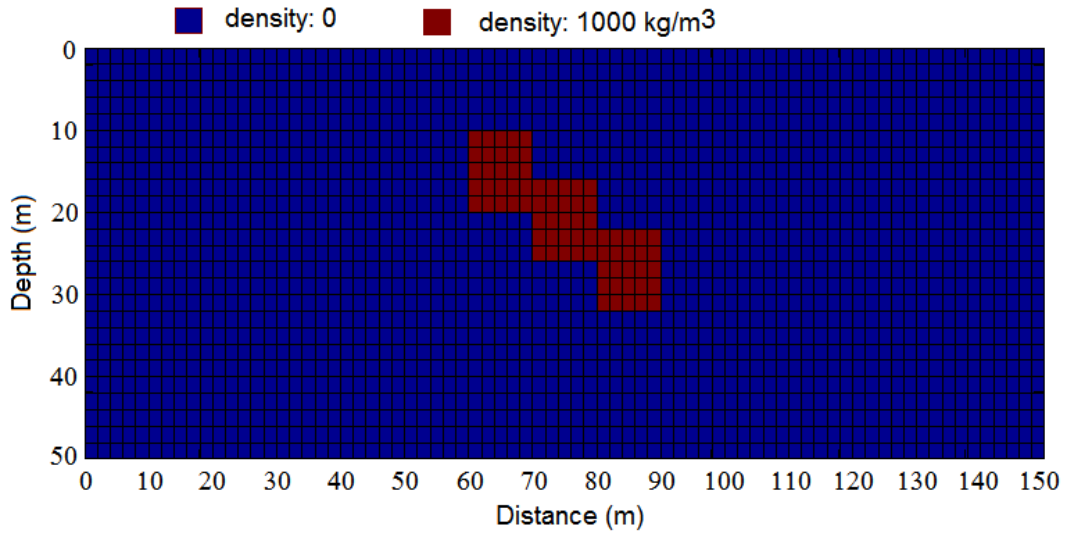


Figure 3. Second assumed density model in the inversion domain, which is constituted by 75×25 blocks with dimension $2 \text{ m} \times 2 \text{ m}$.

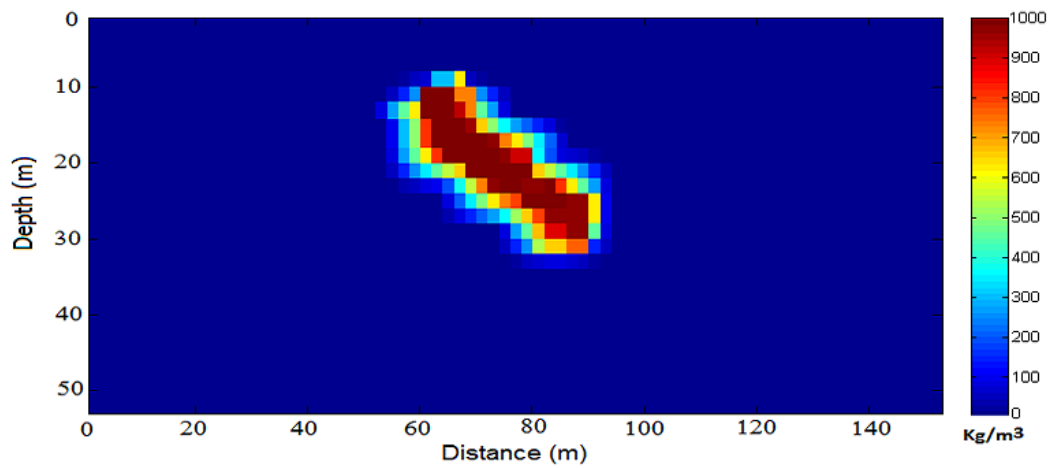


Figure 4. The obtained density distribution from inverting the gravity response of the second assumed model

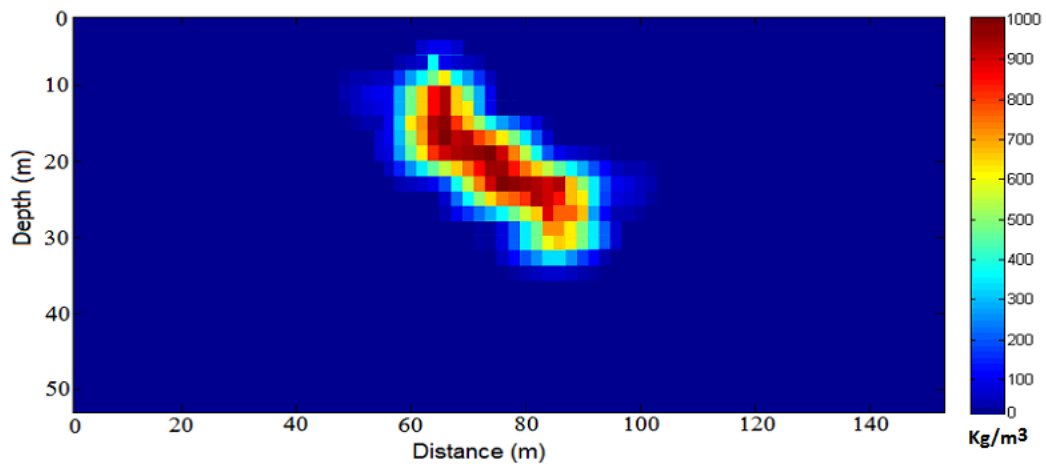


Figure 5. The obtained density distribution from inverting the gravity response of the second assumed model as corrupted with 5% random noise

GRAVITY OF DYKE MODEL

The gravity effects $g(i)$ of a finite dyke-like structure at a point $x(i)$ along a profile perpendicular to its strike direction which runs across the center of the target (Figure 6), is given in Telford and Geldart (1976) as

$$\begin{aligned}
 g(i) = 2G\rho w \frac{1}{2} \sin \theta \log & \frac{\left\{ (z + H \sin \theta)^2 + (x(i) + H \cos \theta)^2 + Y^2 \right\}^{\frac{1}{2}} - Y}{(z + H \sin \theta)^2 + (x(i) + H \cos \theta)^2 + Y^{\frac{1}{2}} + Y} \\
 & \times \frac{\left(x(i)^2 + z^2 + Y^2 \right)^{\frac{1}{2}} + Y}{\left(x(i)^2 + z^2 + Y^2 \right)^{\frac{1}{2}} - Y} \\
 - \cos \theta \tan^{-1} & \frac{Y(z \sin \theta + H + x(i) \cos \theta)}{\left\{ (z + H \sin \theta)^2 + (x(i) + H \cos \theta)^2 + Y^2 \right\}^{\frac{1}{2}} (x(i) \sin \theta - z \cos \theta)} \\
 + \cos \theta \tan^{-1} & \frac{Y(z \sin \theta + H + x(i) \cos \theta)}{\left\{ x(i)^2 + z^2 + Y^2 \right\}^{\frac{1}{2}} (x(i) \sin \theta - z \cos \theta)}
 \end{aligned} \tag{17}$$

Where the G is the gravitational constant, ρ is the density contrast, w is the thickness, θ is the dip angle of the dyke considered anticlockwise from horizontal, z is the depth to the top, $2Y$ is the strike length of the dyke and H is the dipping extent of the buried dyke.

NONLINEAR INVERSION METHODOLOGY

The inversion of gravity anomalies is implicitly a mathematical process, aimed at fitting the computed gravity anomalies to the observed ones in the least-squares approach and then estimating the four parameters namely the depth to top (z), width (thickness) (w), dip (slope) θ and dipping extent (height) (H). The process of the inversion begins by computing the theoretical gravity anomaly of the assumed simple geometry using equation (17). The difference between the observed gravity $g_{obs}(x_i)$, and calculated gravity anomaly of an initial assumed model $g_{cal}(x_i)$, can be estimated by a misfit function, J (Chakravarthi and Sundararajan, 2007), as

$$J = \sum_{i=1}^N \left[g_{obs}(x_i) - g_{cal}(x_i) \right]^2 \tag{18}$$

N is the number of observed gravity data. We have employed the Marquardt's algorithm (1963) given by Chakravarthi and Sundararajan (2006a) for minimizing the misfit function until the normal equations can be solved for overall modifications of the four unknown structural parameters, as

$$\sum_{i=1}^N \sum_{k=1}^4 \frac{\partial g(x_i)}{\partial a_j} \frac{\partial g(x_i)}{\partial a_k} (1 + \delta \lambda) da_k = \sum_{i=1}^N \left[g_{obs}(x_i) - g_{cal}(x_i) \right] \frac{\partial g(x_i)}{\partial a_j}, \text{ for } j = 1, \dots, 4 \tag{19}$$

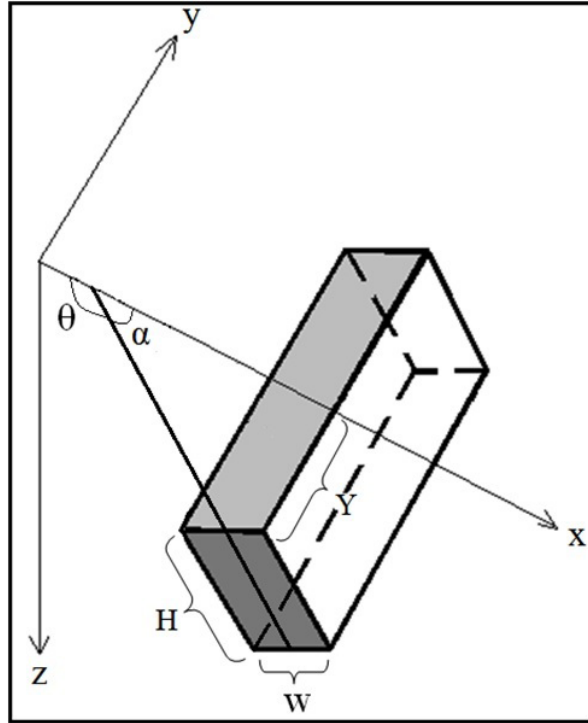


Figure 6. Geometry of a 3D dipping tabular target

where d_{a_k} , $k=1, 2, 3$ and 4 are applied to the four model parameters of the sheet-like geometry structure. Partial derivatives required in the above system of equation (19) are calculated by a numerical approach using Matlab. Also,

$$\delta = \begin{cases} 1 & \text{for } k = j, \\ 0 & \text{for } k \neq j, \end{cases}$$

and λ is the damping factor. The advancements, d_{a_k} , $k=1, 2, 3$ and 4 evaluated from equation (19) are then added to or subtracted from the available parameters estimated from last iteration and the process repeats until the misfit, J , in equation (18) descends below a predetermined allowable error or the damping factor obtains a large value which is greater than predefined amount or the repetition continues until the end of the considered number for iterations (Chakravarthi and Sundararajan, 2008).

SYNTHETIC MODEL ANALYSIS WITH MARQUARDT INVERSION

Figure 7(a) show the observed and calculated gravity anomalies due to the initial and assumed models which are shown in figure 7(b). The considered values for the density contrast is $\rho=1000 \text{ kg/m}^3$ and semi-length of the dyke strike is $Y=50 \text{ m}$, values that during inversion remain constant. The selected values for the parameters which improve during inversion, i.e. depth to top, width, dip and height for the initial model are 20 m , 15 m , 60° clockwise from the horizontal toward the right (i.e. α in Figure 1 or 120° anticlockwise from the horizontal (θ)) and 60 m , respectively and for the assumed model are 15 m , 12 m , 54° clockwise from the horizontal (i.e. α in Figure 6 or 36° from the vertical to the right) and 51 m , respectively.

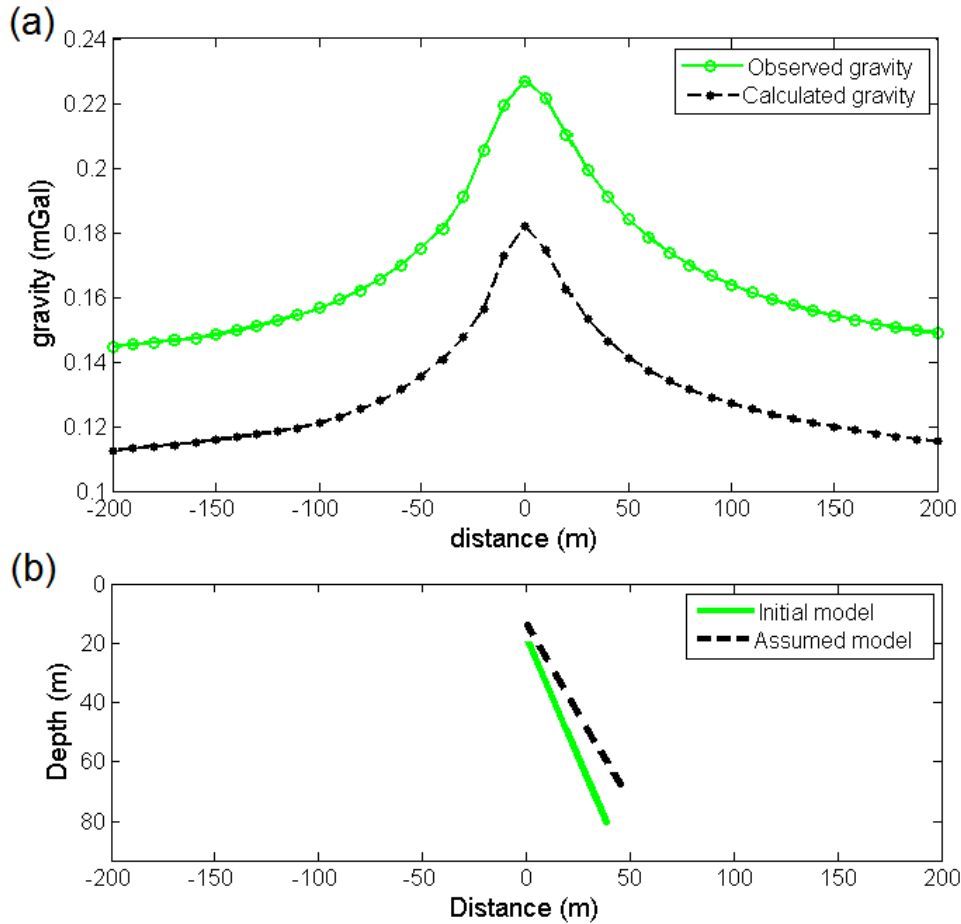


Figure 7. a) The observed and calculated gravity anomalies along a profile due to b) the initial ($z=20$ m, $w=15$ m, $\alpha=60$ degree and $H= 60$ m) and assumed ($z=15$ m, $w=12$ m, $\alpha=54$ degree and $H= 51$ m) models with a density contrast of 1000 kg/m^3

The predefined values for misfit function, J , iteration number and maximum damping factor (λ) are 10^{-4} mGal, 100 and 14, respectively. The initial damping factor is given as 0.5.

The misfit, J , reduces intensely from its initial value of 0.214 mGal at the first iteration to 0.000073 mGal at the end of the 6th iteration and then incrementally reaches 45×10^{-7} mGal at the 10th iteration (Figure 8e). Because the misfit, J , obtained at the 10th iteration was smaller than the allowable error value, the iteration process is ceases and therefore the optimum estimates for the depth, width, dip and height (dipping extend) are corresponding to the evaluated quantity at 9th iteration of the inverse modeling.

Figures 8(a), 8(b), 8(c) and 8(d) shows the variations of the model parameters, i.e. z , w , α and H versus the iteration number. The conclusive obtained parameters values are $z=19.98$ m, $w=15$ m, $\alpha=60.01$ degree and $H=59.97$ m.

Figure 9(a) exhibits the inverted gravity anomaly from the resulted model parameters which is shown in Figure 9(b). The percentage of error in the determination of the depth, width, dip and height parameters are 0.1, zero, about 0.017 m and 0.05, respectively. The considered parameters values and numerical results for the synthetic gravity data are tabulated in Tables 1.

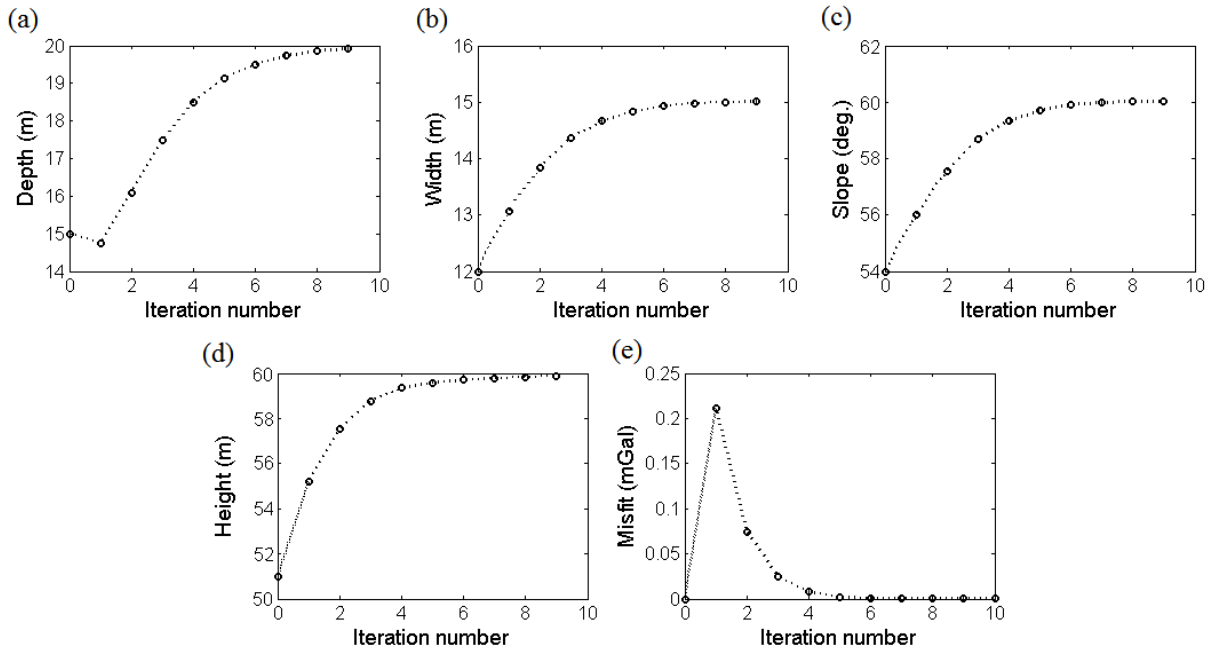


Figure 8. The variations of a) depth b) width c) dip d) height and e) misfit function versus iteration number for synthetic gravity data in figure 2.

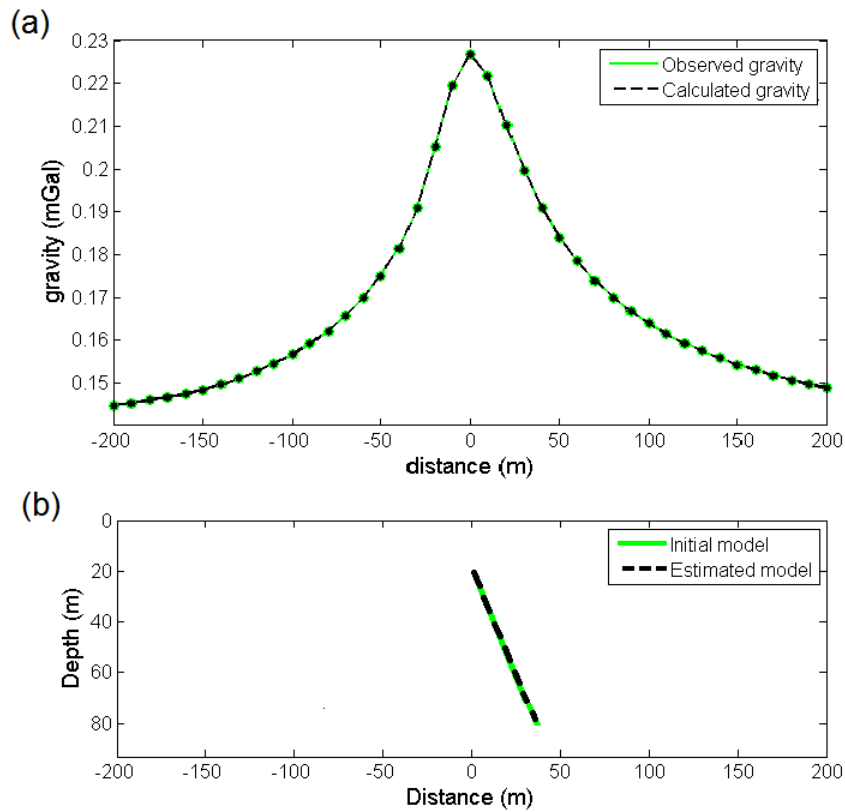


Figure 9. a) The observed and calculated gravity anomalies along a profile due to b) the initial ($z=20$ m, $w=15$ m, $\alpha=60$ degree and $H=60$ m) and estimated ($z=19.98$ m, $w=12$ m, $\alpha=60.01$ degree and $H= 59.97$ m) models with a density contrast of 1000 kg/m^3

Table 1. Numerical results obtained from the Marquardt inversion of the synthetic gravity data

Parameter	Depth (m)	Width (m)	Dip α (degree)	Height (m)
Initial	20	15	60	60
Assumed	15	12	54	51
Estimated	19.98	15	60.01	59.97
Error %	0.1	0	0.017	0.05
Iteration	9			
Misfit (mGal)	62×10^{-7}			

The effect of error has been evaluated by adding 10% random noise to the gravity response of the initial dyke model (Figure 7a) using the following expression:

$$g_{nois}(x_i) = g_{obs}(x_i) [1 + (RAN(i) - 0.5) \times 0.1] \tag{20}$$

where $g_{nois}(x_i)$ is the noise corrupted synthetic data at x_i , and RND (i) is a pseudorandom number whose range is between 0 to 1. The observed gravity data with added 10% random noise is shown in Figure 10(a). Furthermore, the initial and assumed models are shown in Figure 10(b). The considered values for the depth to top, width, dip and height parameters of the assumed model are given as 22 m, 13 m, 63° clockwise from the horizontal toward the right (i.e. $\alpha = 63^\circ$) and 63 m, respectively.

In noisy data case, the assigned values for misfit function, J , iteration and maximum damping factor (λ) are set as in the free-noise data case. The initial damping factor also is determined as 0.2.

The misfit, J , reduces quickly from its initial value of 0.0493 mGal at the first iteration to 0.0024 mGal at the end of the 5th iteration and then incrementally attains 0.0057 mGal after the 16th iteration (Figure 11e). The iteration finished at the 16th iteration where the damping factor value exceeded from the predefined value and reached a value of 24.62. The final values of the evaluated depth to top, width, dip and height at the 15th iteration are $z=19.9$ m, $w=14.7$ m, $\alpha=62.08$ degree and $H=61.5$ m, respectively (Figures 11a to 11d). The percentage of error in the estimation of the depth to top, width, dip and height are 0.1, 2, about 3.67 and 2.5, respectively.

Figure 12(a) shows the inverted gravity anomaly calculated from the inverted model parameters which is shown in Figure 12(b). The theoretical parameters and inferred values for the noise corrupted synthetic gravity data have been summarized in Table 2.

To investigate the solutions constancy and performance of the Marquardt inversion, two different initial and assumed dyke models were assumed to analyze the gravity anomalies related to them with and without a random noise of 10% (Table 3 and 4). The estimated structural parameters are almost correspond to the initial ones.

REAL GRAVITY ANALYSIS

Real gravity data are from the Zereshlu Mining Camp, situated in the west of Mianeh, East Azerbaijan Province, Iran. The main mineral in this area is Manganese which exists mostly in the form of vein deposit or sheet-like structure with the origin of the hydrothermal.

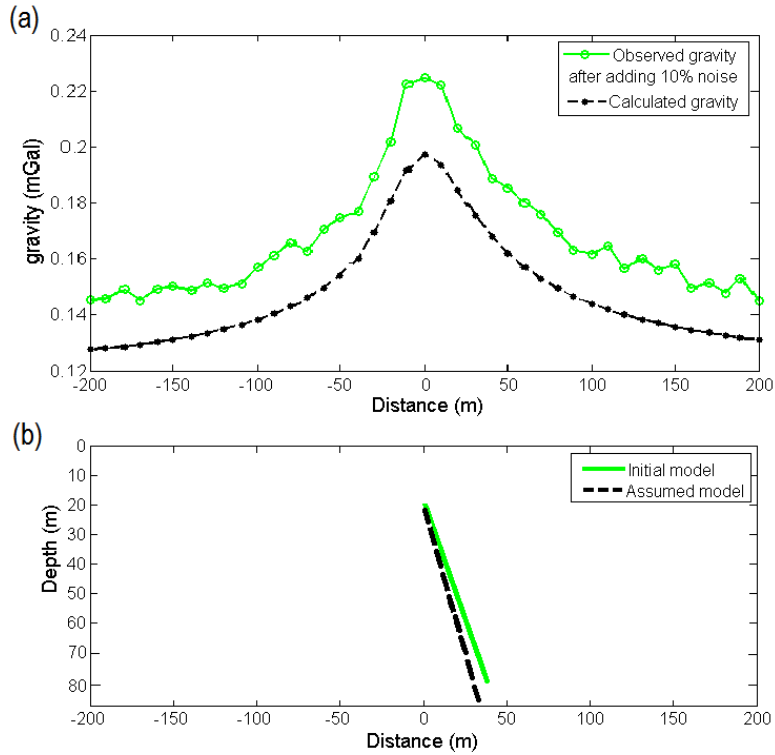


Figure 10. a) The observed gravity anomaly with a added random noise of 10% and calculated gravity anomaly along a profile due to b) the initial ($z=20$ m, $w=15$ m, $\alpha=60$ degree and $H= 60$ m) and assumed ($z=22$ m, $w=13$ m, $\alpha=63$ degree and $H= 63$ m) models with a density contrast of 1000 kg/m^3

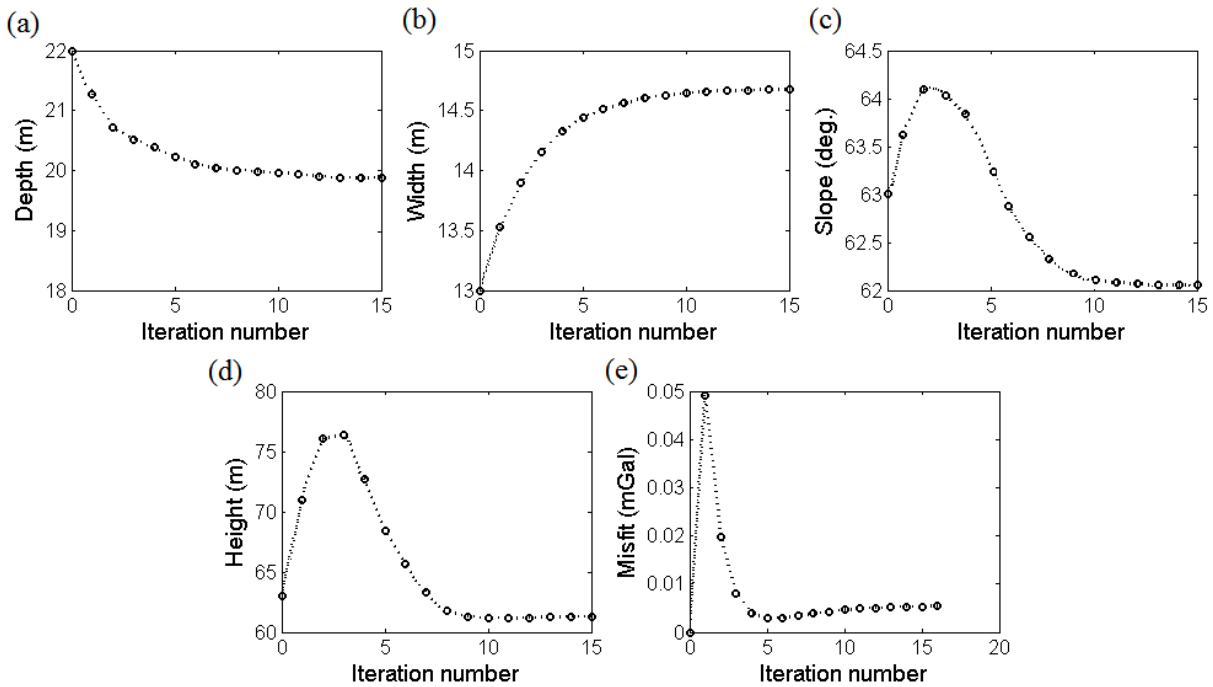


Figure 11. Variations of a) depth b) width c) dip d) height and e) misfit function versus iteration number for 10% noise corrupted synthetic gravity data shown in figure 5.

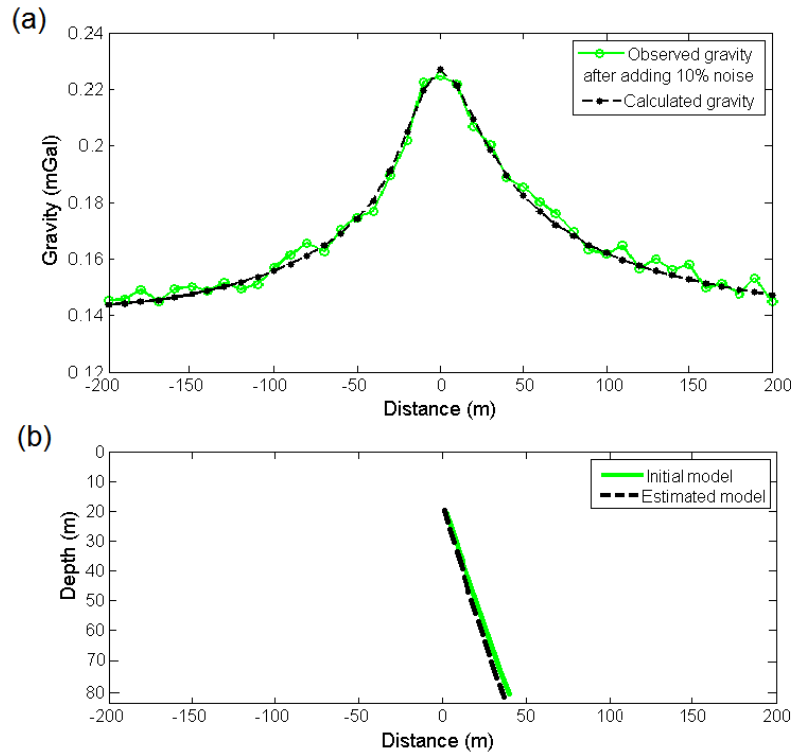


Figure 12. a) The observed gravity anomaly with a added random noise of 10% and calculated gravity anomaly along a profile due to b) the initial ($z=20$ m, $w=15$ m, $\alpha=60$ degree and $H= 60$ m) and estimated ($z=19.9$ m, $w=14.7$ m, $\alpha=62.08$ degree and $H= 61.5$ m) models with a density contrast of 1000 kg/m^3

Table 2. Numerical results obtained from the Marquardt inversion of the noise corrupted synthetic gravity data

Parameter	Depth (m)	Width (m)	Dip α (degree)	Height (m)
Initial	20	15	60	60
Assumed	22	13	63	63
Estimated	19.9	14.7	62.08	61.5
Error %	0.1	2	3.67	2.5
Iteration	15			
Misfit (mGal)	0.0053			

Table 3. Inverted parameters from analysis of free-noise gravity anomalies for different models

Parameter	With 10% random noise							
	Model 1				Model 2			
	Depth (m)	Dip (deg)	Width (m)	Height (m)	Depth (m)	Dip (deg)	Width (m)	Height (m)
Initial	25	50	12	45	40	110	20	65
Assumed	30	60	16	40	32	100	14	58
Estimated	25.01	49.97	11.99	45.02	39.97	110.1	20.02	65.03
Error %	0.04	0.06	0.083	0.044	0.075	0.091	0.1	0.046
Misfit (nT)	0.00000072				0.00000094			
Lambda λ	2.4×10^{-12}				5.7×10^{-23}			
Iteration	12				18			

Table 4. Inverted parameters from analysis of 10% noise-corrupted gravity anomalies for different models

Parameter	With 10% random noise							
	Model 1				Model 2			
	Depth (m)	Dip (deg)	Width (m)	Height (m)	Depth (m)	Dip (deg)	Width (m)	Height (m)
Initial	25	50	12	45	40	110	20	65
Assumed	30	60	16	40	32	100	14	58
Estimated	25.2	50.3	11.85	45.13	38.84	112.6	19.6	66.8
Error %	0.04	0.06	0.083	0.044	2.9	2.36	2	2.77
Misfit (nT)	0.000086				0.078			
Lambda λ	7.1×10^{-18}				32.8			
Iteration	19				23			

Figure 13 exhibits the geological map of the region around the Zereshlu mine. The gravity measurement region is indicated by a black circle. The predominant rocks in the region under investigation are the conglomerate, sandstone and silt. As well as, in this region there are the layers of the basalt, andesite and altered andesite with ferrous oxide. These rocks are considered as the host rocks of the manganese dioxide mineral which is thought to have filled the major faults and fractures. The net density of manganese dioxide is 4.75 gr/cm^3 and the average density of the basalt and andesite are about 2.9 gr/cm^3 and 2.6 gr/cm^3 , respectively. When the ferrous oxide and manganese dioxide are dispersed in the basalt and andesite, therefore, the density of the host rock and that of the target, can consider between 3.2 gr/cm^3 to 3.5 gr/cm^3 . The background density of the study area is about 2.6 gr/cm^3 , thus the density contrast between the body causative of gravity anomalies, i.e. the host rocks, and background domain range between 0.6 gr/cm^3 to 0.9 gr/cm^3 (on average 0.75 gr/cm^3).

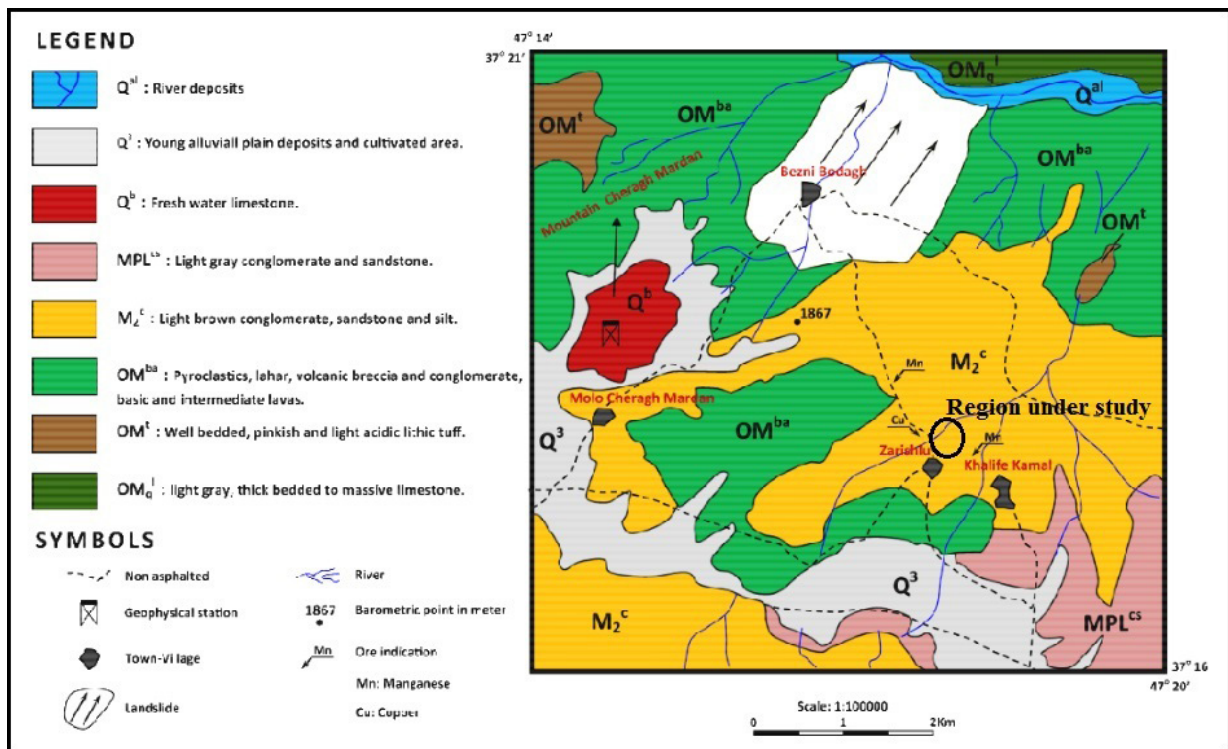


Figure 13. The geological map of the region under investigation

The gravity survey district in zone 38, stretches the UTM coordinate from 704410 m to 704555 m East and from 4130820 m to 4131000 m North. The Bouguer gravity anomaly map of the study area is shown in Figure 14. After removing the effect of regional gravity field from the Bouguer gravity anomaly, the residual gravity anomalies map is achieved (Figure 15). The linear gravity anomalies whose values are positive indicate the sources that are rich in the Manganese. The gravity sampling was performed at 33 points with an interval of 1.03 m along the 34 m profile AA', which runs across the dyke-like structure in the W-E direction (Figure 15). We apply the variations of the residual gravity field at the observed points over the profile AA' for reconstructing the buried structure.

For inverting the real gravity data (Figure 17a) using the damped SVD technique, the underground study domain was divided into $33 \times 17 = 561$ rectangular prisms with respective dimensions of 1.5×2.5 m. Figure 16 shows the density distribution that resulted from the linear inversion. The blocks whose densities are between 3.2 gr.cm^3 to 3.5 gr/cm^3 foreshow the manganese deposit body.

Inversion of the observed gravity data (Figure 17a) using the Marquardt inversion technique, we assume an initial model whose parameters values are given as $z=8$ m, $w=17$ m, $\alpha=38$ degree and $H=19$ m (Figure 17c). The calculated gravity due to the assumed model is shown in Figure 17(a). Moreover, the assigned values for misfit (J), iteration and damping factor (λ) are 0.0005 nmGal, 50 and 15, respectively.

The changes of each parameter and misfit against the iteration number during the inversion process are shown in Figures 18(a) to 18(d). The algorithm performed 10 iterations, before it ceased, since

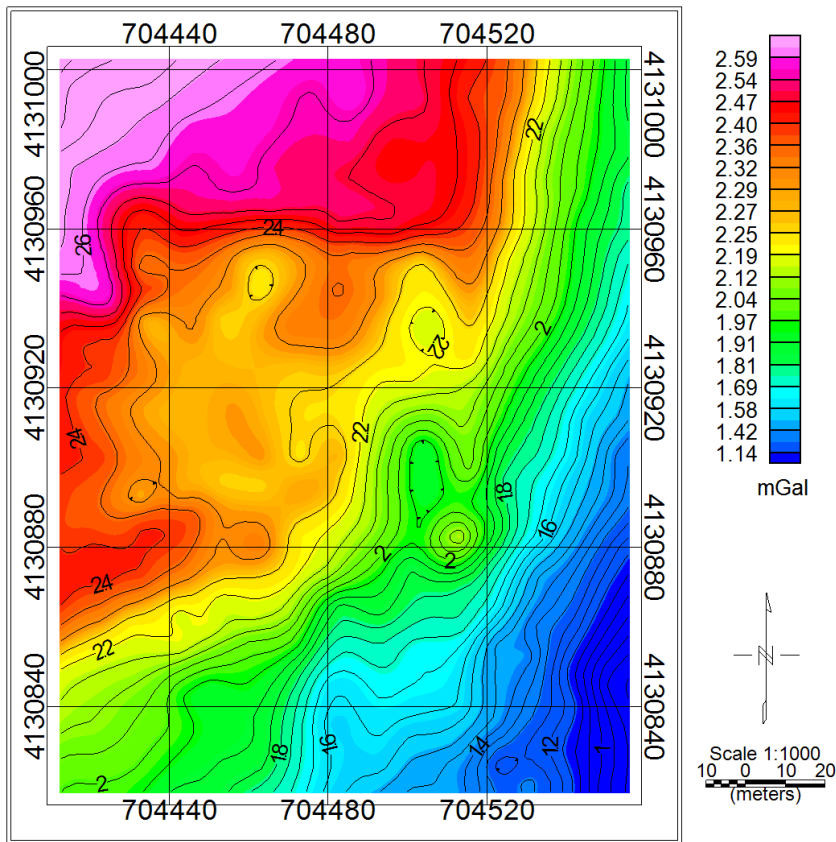


Figure 14. The Bouguer gravity anomaly map of the study district

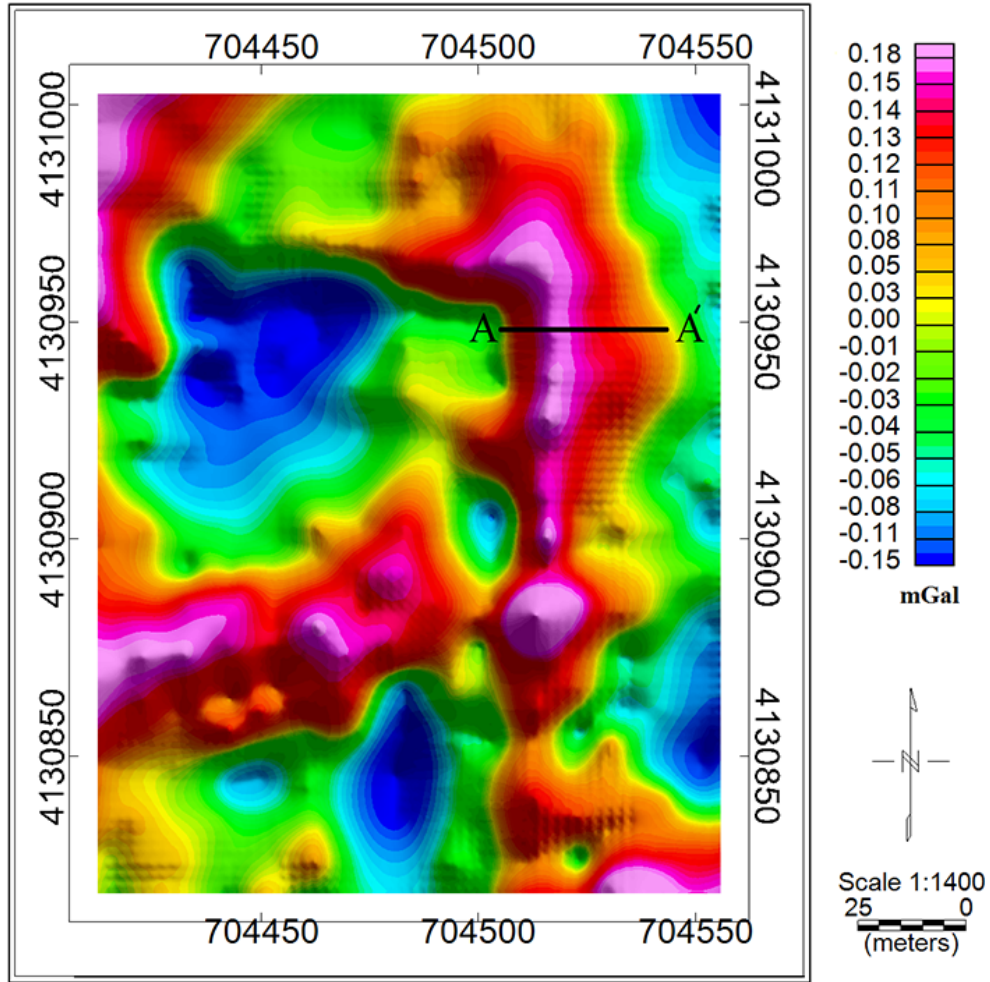


Figure 15. The residual gravity anomalies map of the study district. The profile AA' is specified in W-E direction.

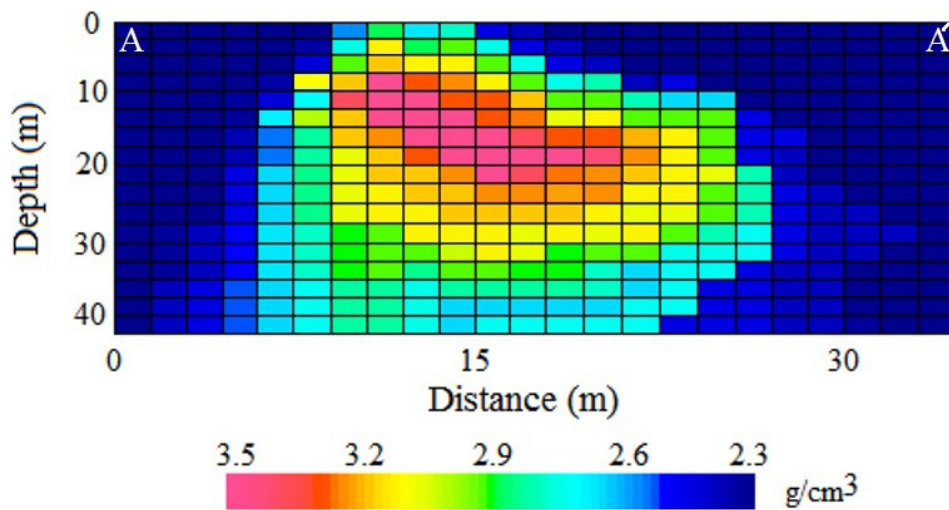


Figure 16. The inverted density distribution by inverting the real gravity data using damped SVD.

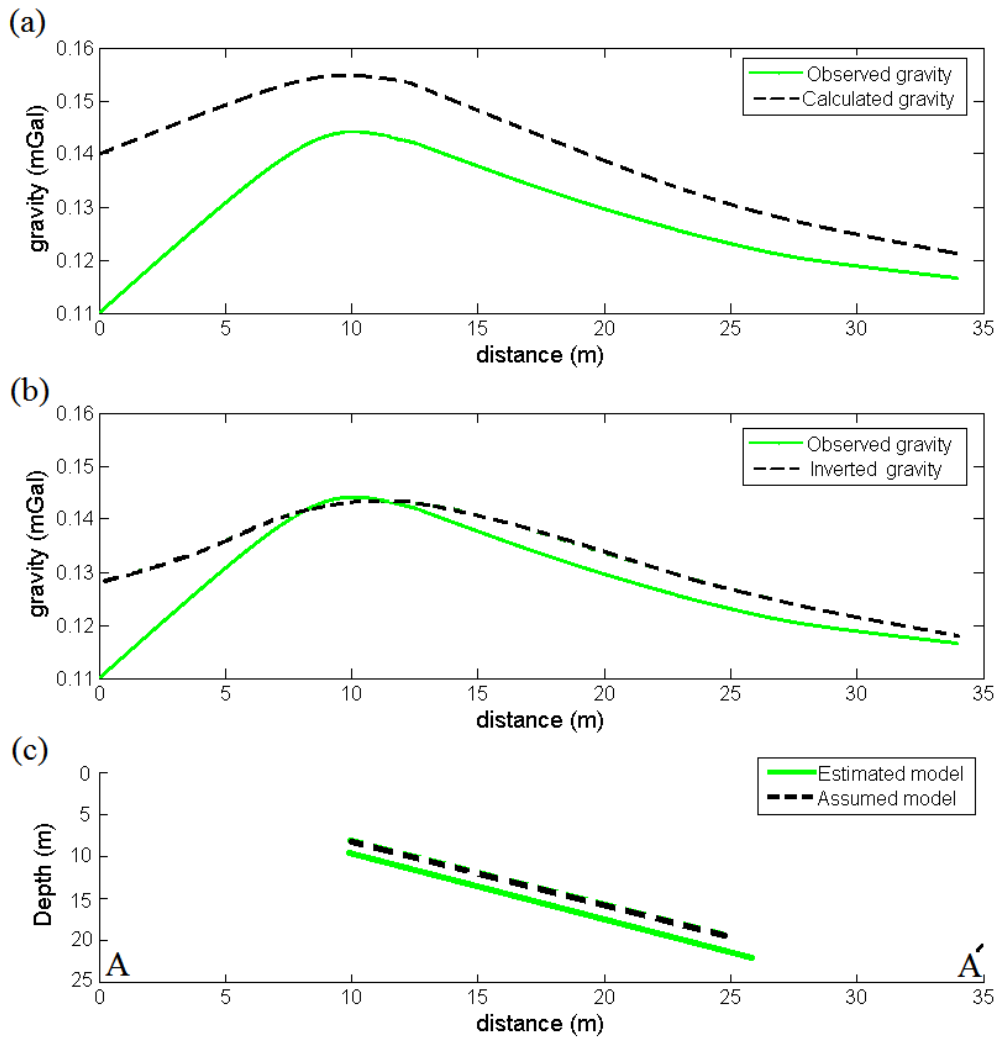


Figure 17. A) The observed gravity along the profile AA' and calculated gravity due to the assumed model, b) Inferred gravity from estimated structure, c) The assumed model and estimated model obtained by the Marquardt inversion.

Table 5. The initial parameters values and final parameters values from interpretation of the real gravity data

Parameter	Depth (m)	Width (m)	Dip α (deg)	Height (m)
Assumed	8	17	38	19
Estimated	9.4	15.8	38.04	20.3
Final Misfit (mGal)	0.00122			
Final Lambda λ	24.68			
Iteration	10			

at the end of this iteration number, the damping factor reached a value greater than the predefined value (see Table 5).

The misfit function variations versus the iteration number (Figure 18e) show a fast decrease from its first value of 0.00015 mGal to its value at the 3th iteration and then increase continually until 10th iteration whose value is 0.000127 mGal. The depth and height parameters increase steadily from its initial value to their final values at the 10th iteration whose values are 9.4 m and 20.3 m, respectively (Figures 18a and 18d). The width parameter decreases significantly until 6th iteration and then gradually achieved 15.8 m at the 10th iteration (Figure 18b). The dip parameter reduces from its initial value to its value at the 3th iteration and then increased rapidly until 10th iteration where it was obtained a value of 38.04 degree towards the east (Figure 18c). The resulted tabular model is delineated in Figure 17 (c). The gravity response estimated from the inferred parameters for the dyke-like structure (Figure 17c) is shown in Figure 17(b). The inverted structural parameters are given in Table 5.

DISCUSSION AND CONCLUSIONS

In this paper, we have introduced two inverse modeling methods, based on the damped singular value decomposition (DSVD) as a linear inversion and the Marquardt optimization algorithm as a nonlinear inversion. The Marquardt optimization algorithm has been developed for interpreting the gravity data due to a dyke-like structure. The validation and performance of the both approaches

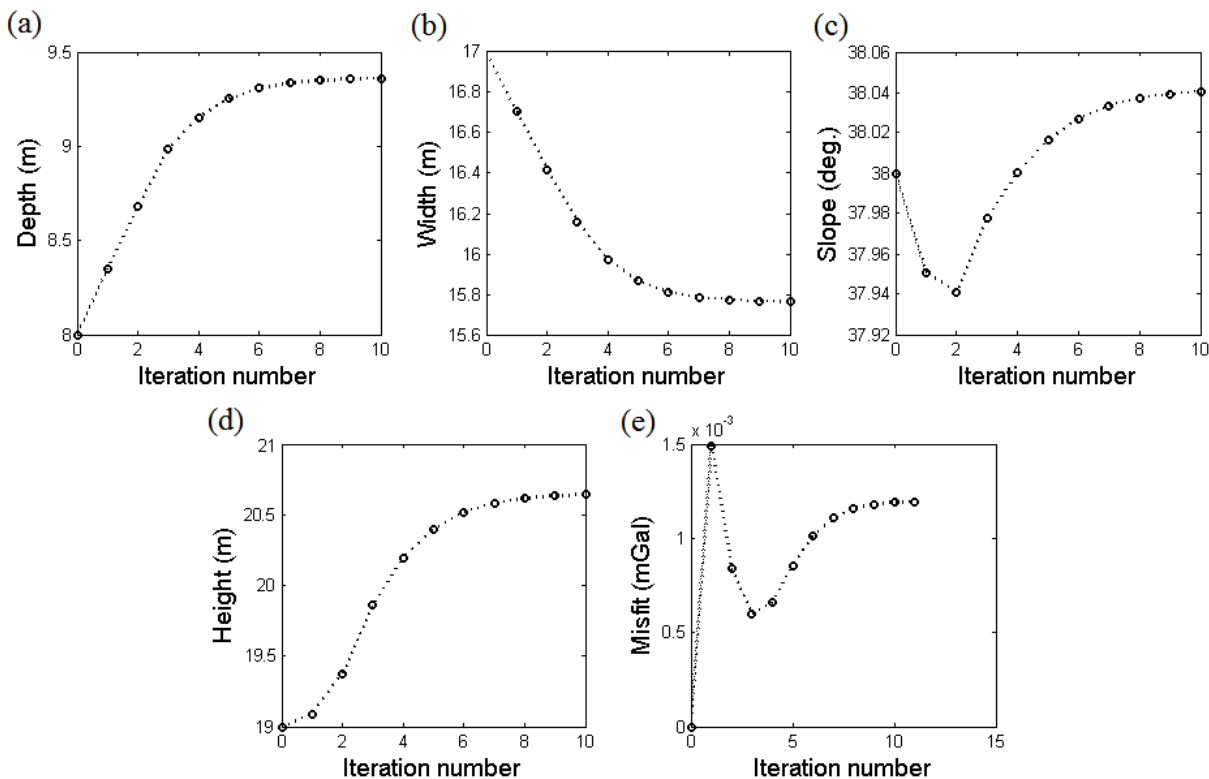


Figure 18. The variations of a) depth b) width c) dip d) height and e) misfit function versus iteration number for the real gravity data.

were evaluated using the theoretical gravity data, with and without random noise. The inverted models obtained from the analysis of the synthetic gravity data via the both methods are exactly similar to the initial ones. The Marquardt inversion shows an acceptable convergence for the various assumed parameters. We employed the both methods for inverting the real gravity data due to a near surface sheet-like structure from Iran. In the resulted density distribution by the damped SVD inversion, the adjacent blocks with a density bigger than 3.2 gr/cm^3 , demonstrate the geometry of the Manganese ore deposit. Considering to inverted density distribution, the depth to the top and bottom of the simulated structure with a direction of NW-SE, are about 7.5 m and 25 m, respectively. Moreover, the average amount of width and extension of the interpreted structure are given about 15 m and 22 m, respectively. As the distribution density resulted from the damped SVD inversion demonstrate a subsurface dyke-like structure, therefore, we can apply the Marquardt optimization algorithm for analyzing the gravity data. The inferred parameters using the Marquardt inversion of the real gravity data demonstrate a dyke-like structure with a width of 15.8 m, a dip of 38.04 degree and a height (extension) of 20.3 m where the depth to the top and bottom are 9.4 m and 21.9 m, respectively.

The comparison of the parameters values of the inverted structures from the damped SVD inversion and the Marquardt optimization method shows a close affinity between them. Therefore, using from the both inversion methods can be a helpful and advantageous strategy in the accurate interpretation of the gravity data.

REFERENCES

- Abdelfattah A.K., Jallouli C., Fnais M., Qaysi S., Alzahrani H., Mogren S., 2021, The key role of conjugate fault system in importing earthquakes into the eastern flank of the Red Sea. *Earth, Planets and Space*, 73, 178.
- Abdelrahman E.M., 1990, Discussion on "A least-squares approach to depth determination from gravity data" by O. P. Gupta. *Geophysics*, 55, 376-378.
- Abdelrahman E.M., Abo-Ezz E.R., Essa K.S., El-Araby T.M., Soliman K.S., 2007, A new least-squares minimization approach to depth and shape determination from magnetic data. *Geophysical Prospecting*, 55, 433-446.
- Abdelrahman E.M., Bayoumi A.I., Abdelhady Y.E., Gobashy M.M., El-Araby H.M., 1989, Gravity interpretation using correlation factors between successive least-squares residual anomalies. *Geophysics*, 54, 1614-1621.
- Abdelrahman E.M., Bayoumi A.I., El-Araby H.M., 1991, A least-squares minimization approach to invert gravity data. *Geophysics*, 56, 115-118.
- Abdelrahman E.M., El-Araby H.M., 1993, Shape and depth solutions from gravity using correlation factors between successive least-squares residuals. *Geophysics*, 59, 1785-1791.
- Abdelrahman E.M., El-Araby H.M., El-Araby T.M., Abo-Ezz E.R., 2001a, Three least squares minimization approaches to depth, shape, and amplitude coefficient determination from gravity data. *Geophysics*, 66, 1105-9.
- Abdelrahman E.M., El-Araby T.M., 1993, A least-squares minimization approach to depth determination from moving average residual gravity anomalies. *Geophysics*, 58, 1779-1784.

- Abdelrahman E.M., El-Araby T.M., El-Araby H.M., Abo-Ezz E.R., 2001b, A new method for shape and depth determinations from gravity data. *Geophysics*, 66, 1774–1778.
- Abdelrahman E.M., El-Araby T.M., Essa K.S., 2003, Shape and depth solutions from third moving average residual gravity anomalies using window curves method. *Kuwait J. Sci. Eng.*, 30, 95–108.
- Abdelrahman E.M., Essa K.S., 2005, Magnetic interpretation using a least-squares curves method. *Geophysics*, 70, L23–L30.
- Abdelrahman E.M., Essa K.S., 2015, A new method for depth and shape determinations from magnetic data. *Pure and Applied Geophysics*, 172, 439–460.
- Abdelrahman E.M., Essa K.S., El-Araby T.M., Abo-Ezz E.R., 2015, Depth and shape solutions from second moving average residual magnetic anomalies. *Exploration Geophysics*, 47(1) 58–66.
- Abdelrahman E.M., Sharafeldin S.M., 1996, An iterative least-squares approach to depth determination from residual magnetic anomalies due to thin dikes. *Journal of Applied Geophysics*, 34, 213–220.
- Al-Garni M.A., 2013, Inversion of residual gravity anomalies using neural network. *Arab. J. Geosci.*, 6, 1509–1516.
- Arnason K., Hersir G.P., 1988, One dimensional inversion of Schlumberger resistivity soundings. Computer Program, Description and User's Guide: The United Nations University, Geothermal Training, Report 8, 59 pp.
- Asfahani J., and Tlas M., 2008, An automatic method of direct interpretation of residual gravity anomaly profiles due to spheres and cylinders. *Pure and Applied Geophysics*, 165(5), 981–994.
- Asfahani J., Tlas M., 2007, A robust nonlinear inversion for the interpretation of magnetic anomalies caused by faults, thin dikes and sphere like structure using stochastic algorithms. *Pure and Applied Geophysics*, 164, 2023–2042.
- Ateya I.L., Takemoto, S., 2002, Gravity inversion modeling across a 2-D dike-like structure-A Case Study. *Earth Planets Space*, 54, 791–796.
- Bastani M., Pedersen L.B., 2001, Automatic interpretation of magnetic dike parameters using the analytical signal technique. *Geophysics*, 66, 551–561.
- Biswas A., 2016. Interpretation of gravity and magnetic anomaly over thin sheet-type structure using very fast simulated annealing global optimization technique. *Modeling Earth Systems and Environment*, 2(1), 30.
- Biswas A., Parija M.P., Kumar S., 2017, Global nonlinear optimization for the interpretation of source parameters from total gradient of gravity and magnetic anomalies caused by thin dyke. *Annals of Geophysics*, 60, 2, G0218.
- Bosch M., McGaughey J., 2001, Joint inversion of gravity and magnetic data under lithological constraints. *The Leading Edge*, 20, 877–881.
- Bosch M., Meza R., Jiménez R., Hönig A., 2006, Joint gravity and magnetic inversion in 3D using Monte Carlo methods. *Geophysics*, 71(4), G153–G156.
- Chakravarthi V., Sundararajan N., 2004, Ridge regression algorithm for gravity inversion of fault structures with variable density. *Geophysics*, 69, 1394–1404.

- Chakravarthi V., Sundararajan N., 2006a, Gravity anomalies of multiple prismatic structures with depth-dependent density – A Marquardt inversion. *Pure and Applied Geophysics*, 163, 229–242.
- Chakravarthi V., Sundararajan N., 2007, Marquardt optimization of gravity anomalies of anticlinal and synclinal structures with prescribed depth-dependent density. *Geophysical Prospecting*, 55, 571–587.
- Chakravarthi V., Sundararajan N., 2008, TODGINV—A code for optimization of gravity anomalies due to anticlinal and synclinal structures with parabolic density contrast. *Computers & Geosciences*, 34, 955–966.
- Cooper G.R.J., 2012, The semi-automatic interpretation of magnetic dyke anomalies. *Computers & Geosciences*, 44, 95–99.
- Cooper G.R.J., 2014, The automatic determination of the location and depth of contacts and dykes from aeromagnetic data. *Pure and Applied Geophysics*, 171, 2417–2423.
- Cooper G.R.J., 2015, Using the analytic signal amplitude to determine the location and depth of thin dikes from magnetic data. *Geophysics*, 80, J1–J6.
- Eshaghzadeh A., 2017, Depth Estimation Using the Tilt Angle of Gravity Field due to the Semi-Infinite Vertical Cylindrical Source. *Journal of Geological Research*, Article ID 3513272, 7 pages.
- Eshaghzadeh A., Hajian A., 2018, 2-D inverse modeling of residual gravity anomalies from Simple geometric shapes using Modular Feed-forward Neural Network. *Annals of Geophysics*, 61,1, SE115.
- Eshaghzadeh A., Kalantary R.A., 2015, Anticlinal Structure Modeling with Feed Forward Neural Networks for Residual Gravity Anomaly Profile. 8th congress of the Balkan Geophysical Society, doi: 10.3997/2214-4609.201414210.
- Eslam E., Salem A., Ushijima K., 2001, Detection of cavities and tunnels from gravity data using a neural network. *Explor. Geophys.*, 32, 204–208.
- Essa K.S., 2007, A simple formula for shape and depth determination from residual gravity anomalies. *Acta Geophysica*, 55(2), 182–190.
- Essa K.S., 2012, A fast interpretation method for inverse modelling of residual gravity anomalies caused by simple geometry. *Journal of Geological Research*, Article ID 327037.
- Essa K.S., 2013, New fast least-squares algorithm for estimating the best-fitting parameters due to simple geometric-structures from gravity anomalies. *Journal of Advanced Research*. <http://dx.doi.org/10.1016/j.jare.2012.11.006>.
- Farquharson C.G., Ash M.R., Miller H.G., 2008, Geologically constrained gravity inversion for the Voisey's Bay ovoid deposit. *The Leading Edge*, 27, 64–69.
- Gallardo L.A., Meju M., 2003, Characterization of heterogeneous near-surface materials by joint 2D inversion of DC and seismic data. *Geophysical Research Letters*, 30, L1658.
- Gupta O.P., 1983, A least-squares approach to depth determination from gravity data. *Geophysics*, 48, 357–360.
- Hammer S., 1977, Graticule spacing versus depth discrimination in gravity interpretation. *Geophysics*, 42, 60–65.

Heincke B., Jegen M., Moorkamp M., Chen J., Hobbs, R.W., 2010, Adaptive coupling strategy for simultaneous joint inversions that use petrophysical information as constraints, 80th Annual International Meeting. SEG, Expanded Abstracts, 29, 2805–2809.

Ialongo S., Fedi M., Florio G., 2014, Invariant models in the inversion of gravity and magnetic fields and their derivatives. *Journal of Applied Geophysics*, 110, 51-62.

Kamm J., Lundin I.A., Bastani M., Sadeghi M., Pedersen L.B., 2015, Joint inversion of gravity, magnetic, and petrophysical data—A case study from a gabbro intrusion in Boden, Sweden. *Geophysics*, 80(5), B131–B152.

Last B.J., Kubik K., 1983, Compact gravity inversion. *Geophysics*, 48, 713-721.

Lelièvre P.G., Farquharson C.G., Hurich C.A., 2012, Joint inversion of seismic travel times and gravity data on unstructured grids with application to mineral exploration. *Geophysics*, 77, K1–K15.

Lines L.R., Treitel S., 1984, A review of least-squares inversion and its application to geophysical problems. *Geophys. Prosp.*, 32, 159-186.

Li Y., Oldenburg D.W., 1998, 3-D inversion of gravity data. *Geophysics*, 63, 109-119.

Marquardt D.W., 1963, An algorithm for least-squares estimation of nonlinear parameters. *Journal of the Society of Indian Applied Mathematics*, 11, 431–441.

Meju M.A., 1994, Geophysical data analysis: Understanding Inverse Problem Theory and Practice, Society of Exploration Geophysics Course Notes Series, 1st edn., No. 6, SEG publishers, Tulsa, Oklahoma, 296 pp.

Menke W., 1984, Geophysical data Analysis: Discrete Inverse Theory, Academic Press, Inc., New York.

Mohan N.L., Anandababu L., Rao, S., 1986, Gravity interpretation using the Melin transform. *Geophysics*, 51, 114-122.

Odegard M.E., Berg, J.W., 1965, Gravity interpretation using the Fourier integral. *Geophysics*, 30, 424-438.

Oldenburg D.W., 1974, The inversion and interpretation of gravity anomalies. *Geophysics*, 39(4), 526-536.

Osman O., Muhittin A.A., Ucan, O.N., 2007, Forward modeling with Forced Neural Networks for gravity anomaly profile. *Math. Geol.*, 39, 593-605.

Osman O., Muhittin A.A., Ucan O.N., 2006, A new approach for residual gravity anomaly profile interpretations: Forced Neural Network (FNN). *Annals of Geophysics*, 49, 6.

Parker R.L., 1972, The Rapid Calculation of Potential Anomalies. *Geophysical Journal of the Royal Astronomical Society*, 31, 447-455.

Peace A.L., Welford J.K., Geng M., Sandeman H., Gaetz B.D., Ryan S.S., 2018, Structural geology data and 3-D subsurface models of the Budgell Harbour Stock and associated dykes, Newfoundland, Canada. *Data in Brief*, 21, 1690-1696.

Peace A.L., Welford J.K., Geng M., Sandeman H., Gaetz B.D., Ryan S.S., 2018, Structural geology data and 3-D subsurface models of the Budgell Harbour Stock and associated dykes, Newfoundland, Canada. *Data in Brief*, 21, 1690-1696.

- Pilkington M., 2006, Joint inversion of gravity and magnetic data for two layer models. *Geophysics*, 71(3), L35–L42.
- Shamsipour P., Chouteau M., Marcotte D., 2011, 3D stochastic inversion of magnetic data. *Journal of Applied Geophysics*, 73, 336–347.
- Shamsipour P., Marcotte D., Chouteau M., 2012, 3D stochastic joint inversion of gravity and magnetic data. *Journal of Applied Geophysics*, 79, 27–37.
- Shamsipour P., Marcotte D., Chouteau M., Keating P., 2010, 3D stochastic inversion of gravity data using cokriging and cosimulation. *Geophysics*, 75, I1–I10.
- Sharma B., Geldart L.P., 1968, Analysis of gravity anomalies of two-dimensional faults using Fourier transforms. *Geophys. Prosp.*, 77-93.
- Shaw R.K., Agarwal N.P., 1990, The application of Walsh transforms to interpret gravity anomalies due to some simple geometrically shaped causative sources: A feasibility study. *Geophysics*, 55, 843-850.
- Skeels D.C., 1947, Ambiguity in gravity interpretation. *Geophysics*, 12, 43-56.
- Telford W.M., Geldart L.P., 1976, *Applied Geophysics*. Cambridge University Press, Cambridge.
- Tlas M., Asfahani J., 2011a, Fair function minimization for interpretation of magnetic anomalies due to thin dikes, spheres and faults. *Journal Applied Geophysics*, 75, 237–243.
- Tlas M., Asfahani J., 2011b, A new best-estimate methodology for determining magnetic parameters related to field anomalies produced by buried thin dikes and horizontal cylinder-like structures. *Pure and Applied Geophysics*, 168, 861–870.
- Tschirhart V., Jefferson C.W., Morris W.A., 2017, Basement geology beneath the northeast Thelon Basin, Nunavut: insights from integrating new gravity, magnetic and geological data. *Geophysical Prospecting*, 65, 617-636.
- Tschirhart V., Morris W.A., Jefferson C.W., Keating P., White J.C., Calhoun, L., 2013, 3D geophysical inversions of the north-east Amer Belt and their relationship to the geologic structure. *Geophysical Prospecting*, 61, 547–560.
- Tsuboi C., 1983, *Gravity*, 1st edn. George Allen & Unwin Ltd, London, 254 pp.
- Williams N.C., 2008, Geologically-constrained UBC-GIF gravity and magnetic inversions with examples from the Agnew-Wiluna Greenstone Belt, Western Australia. Ph.D. thesis, University of British Columbia.
- Zeyen H., Pous H., 1993, 3-D joint inversion of magnetic and gravimetric data with a priori information. *Geophysical Journal International*, 112, 244–256.

<https://doi.org/10.22201/igeof.00167169p.2022.61.4.2228>

Seal Cap Resistivity Structure of Los Humeros Geothermal Field from Direct Current and Transient Electromagnetic Soundings

Carlos Flores^{1*} , Thalia Avilés Esquivel¹, Claudia Arango-Galván²  and José Luis Salas²

Received: March 19, 2020; accepted: August 16, 2022; published on-line: October 1, 2022.

RESUMEN

Los métodos geofísicos dan información importante en la exploración de recursos geotérmicos. En este trabajo buscamos pistas de la presencia de un yacimiento geotérmico conocido (Los Humeros, México) en la estructura somera de la resistividad eléctrica. Interpretamos cerca de 410 sondeos eléctricos verticales (SEV) y 230 sondeos electromagnéticos transitorios (TEM) que dan información de la resistividad eléctrica hasta profundidades de 1 km, alcanzándose en algunos sitios hasta 2 km. La estructura vertical de la resistividad generalmente consiste de una secuencia resistivo-conductor-resistivo. El rasgo más importante es la unidad conductora, conocida como el casquete de arcillas, asociado con arcillas de alteración hidrotermal arriba del yacimiento geotérmico. Esta unidad sufre de un problema de equivalencia, donde no se pueden determinar por separado su resistividad de su espesor. Sin embargo, las temperaturas de los pozos y las arcillas de alteración asociadas ayudan a constreñir este problema. En varias zonas de la unidad resistiva somera encontramos resistividades bajas que podrían representar zonas de recarga donde roca fracturada permite la infiltración de agua meteórica. El casquete de arcillas no solo se presenta sobre el yacimiento, sino que tiene una presencia regional. Sin embargo, sobre el reservorio esta unidad tiene una mayor conductancia y su cima está más somera. Los pocos lugares donde los sondeos eléctricos alcanzaron profundidades del yacimiento con resistividades bien resueltas dan una resistividad media de 118 ohm·m, sin poder diferenciar estadísticamente las zonas productoras de las no productoras. Esta resistividad está dentro del rango de valores encontrados en otras zonas geotérmicas del mundo.

PALABRAS CLAVE: Los Humeros, zona geotérmica, métodos eléctricos y electromagnéticos, resistividad.

Editorial responsibility: Fernando Corbo-Camargo

*Corresponding author at cflores@cicese.mx

¹División de Ciencias de la Tierra, Centro de Investigación Científica y Educación Superior de Ensenada, Carretera Ensenada-Tijuana 3918, Zona Playitas, CP22860, Ensenada, Baja California, México.

²Instituto de Geofísica, Universidad Nacional Autónoma de México. Ciudad Universitaria, Coyoacán, 04510 CDMX, México.

ABSTRACT

Geophysical methods provide important information in the exploration of geothermal resources. In this study, we search for clues in the shallow resistivity structure of the presence of a known geothermal reservoir (Los Humeros, Mexico). We interpret about 410 vertical electric soundings (VES) and 230 transient electromagnetic (TEM) soundings, giving information usually down to depths of 1 km, although in some sites they reached 2 km. The vertical structure of the resistivity generally consists of a resistive-conductive-resistive sequence. The most important feature is the conductive unit, known as the clay-cap, associated with hydrothermal alteration clays overlying the geothermal reservoir. This unit suffers from a widespread equivalence problem, where its resistivity and thickness cannot be determined independently. However, well temperatures and associated alteration clays help to constrain this problem. In the shallow resistive unit we found several zones where its resistivity showed abnormally low values, which could represent recharge zones where fractured rock permits the infiltration of meteoric water to reservoir depths. The conductive clay-cap not only occurs over the geothermal reservoir, but has a regional presence. However, over the reservoir this electric unit has a larger conductance and its top is shallower. The few locations where the resistivity soundings reached depths of the geothermal reservoir with well-resolved estimates give a mean resistivity of 118 ohm·m, with no statistical difference between the producing and non-producing zones. This resistivity value falls within the range found in other geothermal zones in the world.

KEY WORDS: Los Humeros, geothermal field, electric and electromagnetic methods, resistivity

INTRODUCTION

The Los Humeros geothermal field is located 150 km east of Mexico City, at the eastern end of the Mexican Volcanic Belt, inside the largest caldera in Mexico. The geothermal system has been the subject of numerous studies by both the Comisión Federal de Electricidad (CFE), the state agency in charge of the exploration and operation of the field, and the scientific community (e.g., Ferriz, 1982, Arellano *et al.*, 2003, Gutiérrez-Negrín and Izquierdo-Montalvo, 2010, Carrasco-Núñez *et al.*, 2015). In recent years a couple of large projects, CeMIEGeo (Mexican Center for Innovation in Geothermal Energy) and GEMex, a joint geothermal program between the European Community and Mexico have financed a large number of additional studies. The Los Humeros field has been generating electricity since the early ninety's; nowadays it is producing close to 100 MW,

Electrical resistivity is known to be an important physical parameter in the exploration and characterization of geothermal fields. Multiple examples exist of applying resistivity and electromagnetic methods to geothermal systems (Berkold, 1983; Martínez-García, 1992; Spichak and Manzella, 2009; Muñoz, 2014). In this work we analyze the shallow electrical resistivity of Los Humeros geothermal field deduced from more than 600 resistivity and electromagnetic soundings to explore what we can learn on the geothermal reservoir with the analysis of the shallow structure. In here we denote "shallow" to those depths from the surface down to about 1 or 2 km, to differentiate it from the deeper exploration depths of the Magnetotelluric (MT) method, a widely used geophysical method in geothermal exploration.

GEOLOGICAL AND GEOPHYSICAL BACKGROUND

There have been numerous works describing the geology of the area (e.g. Ferriz, 1982, Carrasco *et al.*, 2017, Norini *et al.*, 2019). The most important geologic feature of this geothermal field is the

presence of two nested calderas: Los Humeros and Los Potreros. At about 0.5 Ma the Los Humeros caldera erupted 115 km^3 of pyroclastic deposits, leaving a 21 by 15 km rim. The younger and smaller (10 km diameter) Los Potreros caldera erupted 15 km^3 of ignimbrites at about 0.14 Ma. Although there are over 15 recognizable lithologic units in the geologic column, we will deal with a simplified sequence: basement, pre-caldera, caldera, and post-caldera deposits. The basement rocks are mainly Mesozoic sediments and Tertiary intrusions. The sediments are a Jurassic clastic sequence and Cretaceous marls and limestones. The pre-caldera deposits are andesites and basalt flows with ages from about 4 to 1.5 Ma, 1200 m thick on average. This unit represents the dense but fractured rocks of the geothermal reservoir. Overlying this unit are the calderic pyroclastic deposits with an estimated average thickness of 600 m, covered by the post-caldera volcanism (rhyolitic domes, andesites, and basalts), with an average thickness of 340 m.

Several geophysical studies have been carried out in the area; potential field (e.g. Flores *et al.*, 1977; Campos-Enríquez and Arredondo-Fragoso, 1992; Arzate *et al.*, 2018), active and passive seismicity (Urban and Lermo, 2013; Jousset *et al.*, 2020; Granados-Chavarría *et al.*, 2022) and thermal modeling (Deb *et al.*, 2021). Regarding the techniques used to estimate the subsurface electrical resistivity, studies have been carried out with 413 direct current resistivity soundings (Palacios-Hartweg and García-Velázquez, 1981; Cedillo-Rodríguez, 1999), 61 transient electromagnetic soundings (Seismocontrol, 2005), and two magnetotelluric (MT) studies by Arzate *et al.* (2018), and Benediktsdóttir *et al.* (2020), with 70 and 122 soundings, respectively. The large amount of data of this type probably makes this area the most densely sampled by resistivity techniques in México.

Most of the high-temperature geothermal systems associated with volcanism have a similar resistivity structure (Flóvenz *et al.*, 1985; Pellerin *et al.*, 1996; Anderson *et al.*, 2000; Flóvenz, 2005), characterized by a conductive zone, known as the low-resistivity cap, over the geothermal reservoir (Figure 1). The resistivity is largely dominated by the presence of hydrothermal alteration clays, controlled mainly by the temperature. Starting from the surface, the unaltered volcanic rocks usually have high resistivities. Below this, at temperatures above 70°C , starts the low-resistivity cap, where the conductive clay minerals smectite and zeolite are dominant. At higher temperatures chlorite and/or illite may occur inter-layered with the smectite and zeolites. At temperatures between 220 to 240°C the zeolites disappear and the smectite is replaced by the more resistive chlorite in the core of the geothermal reservoir, which is more resistive than the clays in the low-resistivity cap. The mineral epidote, also resistive, may be present at even higher temperatures.

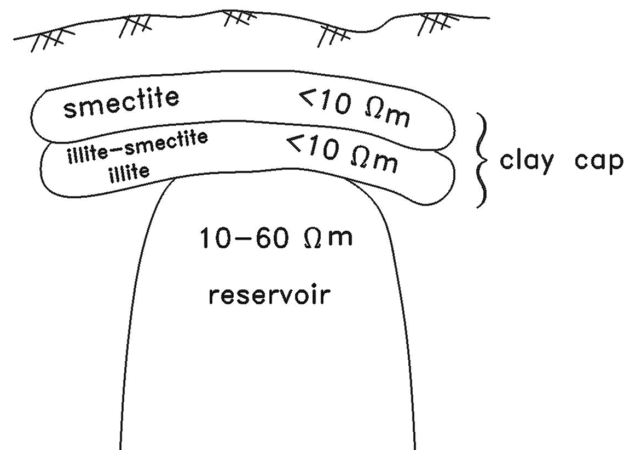


Figure 1. Conceptual model of the distribution of resistivities in a geothermal field (after Pellerin *et al.*, 1996).

In porous or fractured rocks electric conduction is by the movements of ions in the pore fluid. When clay minerals are present there is an additional conduction mechanism, through the electric double layer that forms at the interface of the clay mineral and water, which is more effective than conduction by ionic movement (Ussher *et al.*, 2000). This double-layer conduction, also known as interface conduction, depends on the Cation Exchange Capacity (CEC) of the particular clay mineral; smectite has a significantly higher CEC than chlorite, explaining its higher conductivity in the low-resistivity cap (Ussher *et al.*, 2000).

THE DATA

The working database consists of 413 Vertical Electric Soundings (VES), also known as resistivity soundings, and 234 Transient Electromagnetic (TEM) soundings acquired by CFE. The VES were measured in different field surveys from 1979 to 1986 (Palacios-Hartweg and García-Velázquez, 1981), following the standard field procedure of the Schlumberger array, namely, the gradual increase in steps of the potential electrode spread ($MN/2$) as the current electrode separation ($AB/2$) increases. Typically, the current electrode separations start at 10 m and reach a variable maximum value of 1 to 5.5 km, although most values were 2 and 3.5 km. Figure 3 shows a histogram illustrating these maximum $AB/2$ separations of the Schlumberger data. Figure 2 displays the distribution of these soundings, covering an area of 194 km² with a variable areal density of up to 10 soundings per km² over the reservoir. A Scintrex IPR system was used in the field campaigns.

The transient EM soundings were acquired with the coincident-loop configuration, where a large rectangular or square loop is used as transmitter and a geometrically-coincident horizontal loop is employed as the receiver (Seismocontrol, 2005). The injected direct current (DC) in the loop is periodically interrupted in the form of a linear ramp. An induced current system, flowing in closed paths below the loop and created each time the transmitter current is interrupted, produces a secondary magnetic field. The time variation of the vertical component of this magnetic field induces a voltage in the receiving loop. As the spatial and temporal distribution of the subsurface current system depends upon the ground resistivity, the measured transient voltage gives information about the subsurface resistivity. The locus of the maximum amplitude of the induced currents diffuses downward and outward with time, thereby giving information about deeper regions as time increases (Nabighian, 1979; Hoversten and Morrison, 1982). The shape and time evolution of this induced current resembles the smoke ring of a cigarette smoker.

The area covered by the 234 TEM sounding sites is 22 km², much smaller than the area covered by the resistivity soundings. This area is shown by an irregular blue closed box in Figure 2; for clarity, the location of the individual TEM sites has been omitted. The sites were arranged in a rectangular grid with a 300 m separation between current loops. They were acquired in 2005-2007 with a terraTEM system, employing 330 by 330 m loops. A 1 Hz repetition frequency of the bipolar current waveform was used, injecting currents of about 7.5 A. Although eight transient decays were recorded at each site, about half of them were discarded due to noisy data. Each decay curve represents the stacking of 256 individual voltage decays. Clays may produce Induced Polarization effects, usually manifested as negative voltages at late times (Smith and West, 1989). However, no evidence of this was observed in the data.

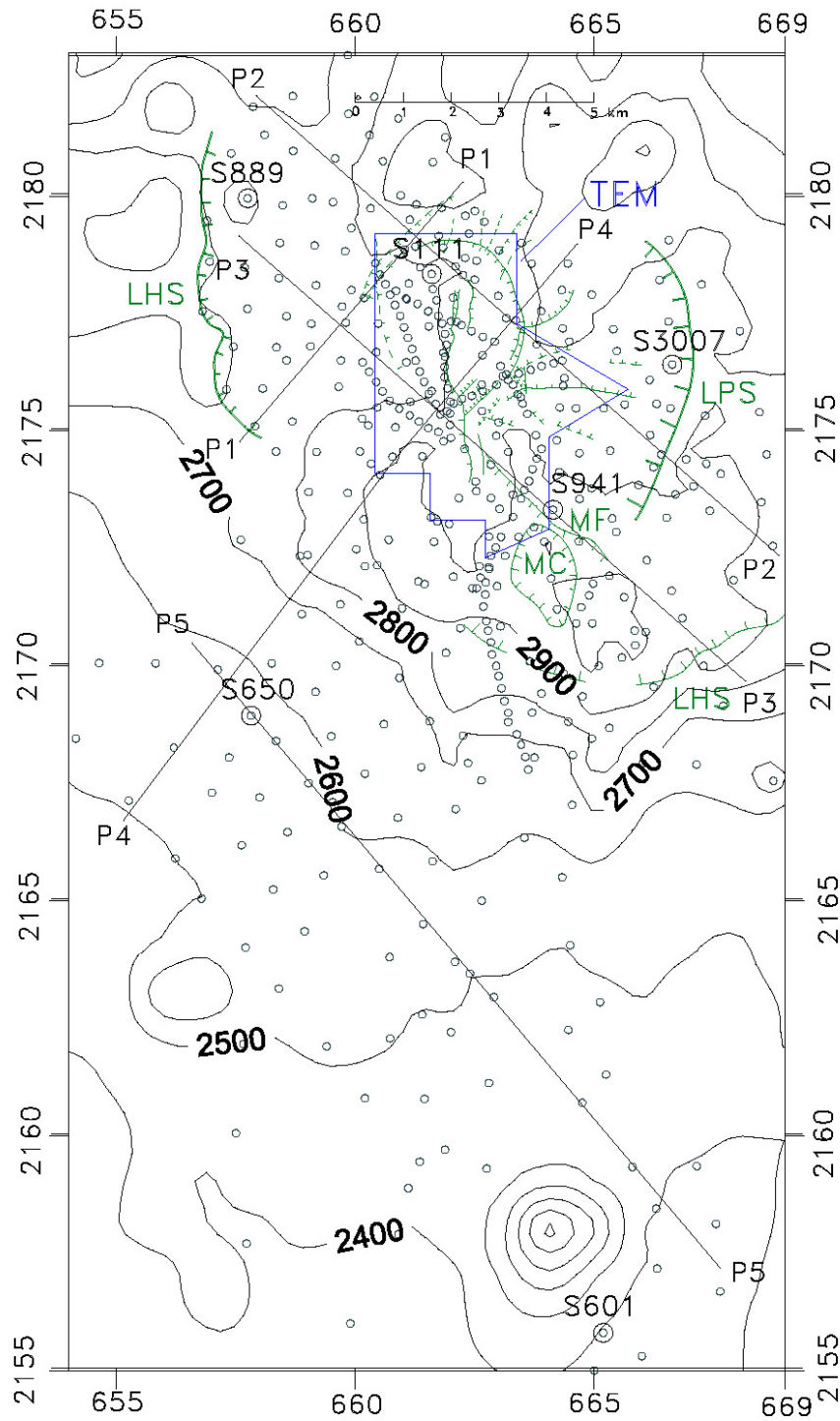


Figure 2. Map of the Los Humeros geothermal zone showing the position of the resistivity soundings (circles) and the transient electromagnetic soundings (area enclosed by the box named TEM). The location of the soundings appearing in Figure 4 and the sections of Figures 5, 8, and 9 are also indicated. Topographic contours every 100 meters. The main structural features are displayed: LHS Los Humeros Scarp, MF Maztaloya Fault, MC Maztaloya crater, and LPS Los Potrerros Scarp.

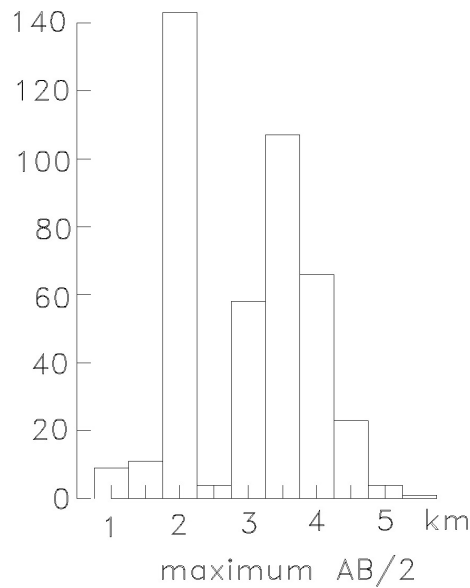


Figure 3. Histogram of the maximum half-separations between the current electrodes used in the resistivity soundings.

DATA MODELING

The soundings were initially inverted to Occam (smooth) models and then to the traditional stratified models with a small number of layers, using in both approaches commercial software. To avoid any possible bias in the interpretation the inversions were carried out independently by three of the co-authors. A general feature of the layered models is a resistive-conductive-resistive structure under the entire study area, standing out the presence of an important conductor. An example of this general structure is shown in Figure 4, where we selected six resistivity soundings from different zones of the study area. Figure 2 shows the location of these example soundings. Each graph shows the measured apparent resistivity data with their estimated error bars, the calculated response, and the inverted model. In each sounding the observed and calculated responses are referred to the left apparent resistivity versus $AB/2$ electrode separation, while the right resistivity axes versus depth should be used for models. The steep decrease in the apparent resistivities responds to the presence of this unit of low resistivity. In soundings 889 and 111 the apparent resistivities display clear rises at the longest electrode separations, the inverted model then showing a deep layer of higher resistivity. In soundings 3007, 650, 601 the electrode separations were not large enough to show this climb in apparent resistivities.

Figure 5 shows two alternative models constructed by stitching together the 1D models along profile P1; its location is described in Figure 2. Figure 5a is the section with the models initially inverted with the commercial program; Figure 5b is a reinterpretation to be described below. The layered models under each sounding site are displayed as color bars, where each color follows the scale exhibited at right. Because the resistivity values have a large range of variation, we adopted a logarithmic scale for the color compartments, with three divisions per decade. Low resistivities are denoted by hot colors (red), while cold colors (blue) are used for high resistivities. As very high resistivities have no interest in geothermal exploration, all values greater than 1,000 $\text{ohm}\cdot\text{m}$ are gathered into a single

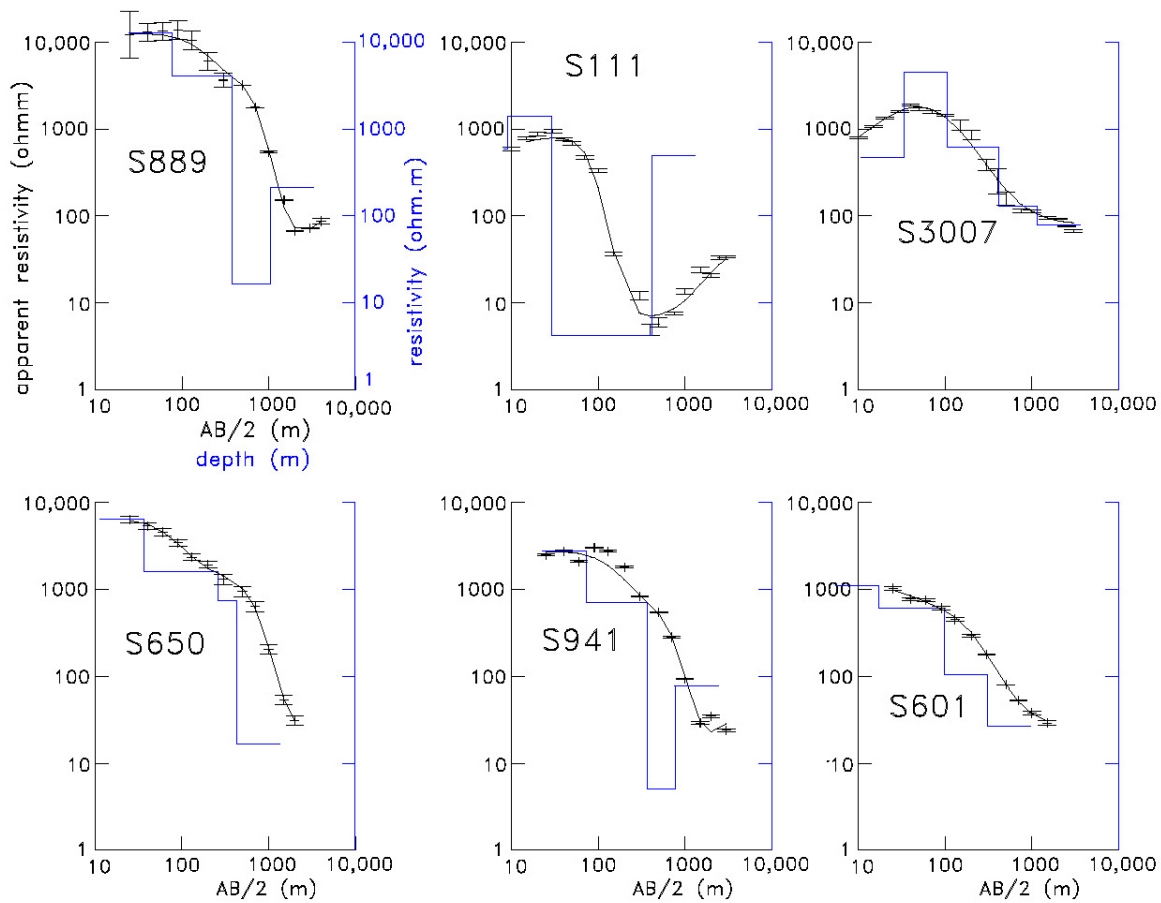


Figure 4. Selected resistivity soundings, their locations shown in Figure 2. Displayed are the observed apparent resistivities and their standard errors (symbols), the inverted layered models and their calculated responses (solid lines)

color compartment (dark blue). We use a vertical exaggeration of two in this section. The zero of the depth scale is at the average altitude of the profile. We also plot the position of the geothermal wells, indicating the depth interval where the geothermal reservoir is located and a simplification of the initial well temperatures estimated with the spherical-radial heat flow assumption by García Gutiérrez (2009). For reasons of clarity we do not show where the different volcanic deposits are located, however, the depth interval covered by the reservoir practically coincides with the pre-caldera volcanism lying above the basement. The locations of the TEM soundings are denoted with the letter "T".

The top and bottom of the conductive unit in the sections of Figure 5 are defined by resistivity values lower than $100 \text{ ohm}\cdot\text{m}$; that is, yellow, orange, and red colors. The threshold value of $100 \text{ ohm}\cdot\text{m}$, although somewhat arbitrary, comes naturally from the distribution of values. In most of the soundings this conductor is directly above the reservoir, which suggests the low resistivities are due to the hydrothermal alteration clays. i.e., it is the clay cap of the conceptual model found in many geothermal systems discussed in the introduction. Mineralogical studies on drill cuttings (Prol-Ledesma, 1990; González *et al.*, 1992; Izquierdo, 1993; Martínez and Alibert, 1994; Martínez-Serrano and Dubois, 1998) show that, indeed, at the depths of the conductive unit there are increased concentrations of montmorillonite (a subclass of smectite) and zeolites, minerals with a high CEC that produce high conductivities.

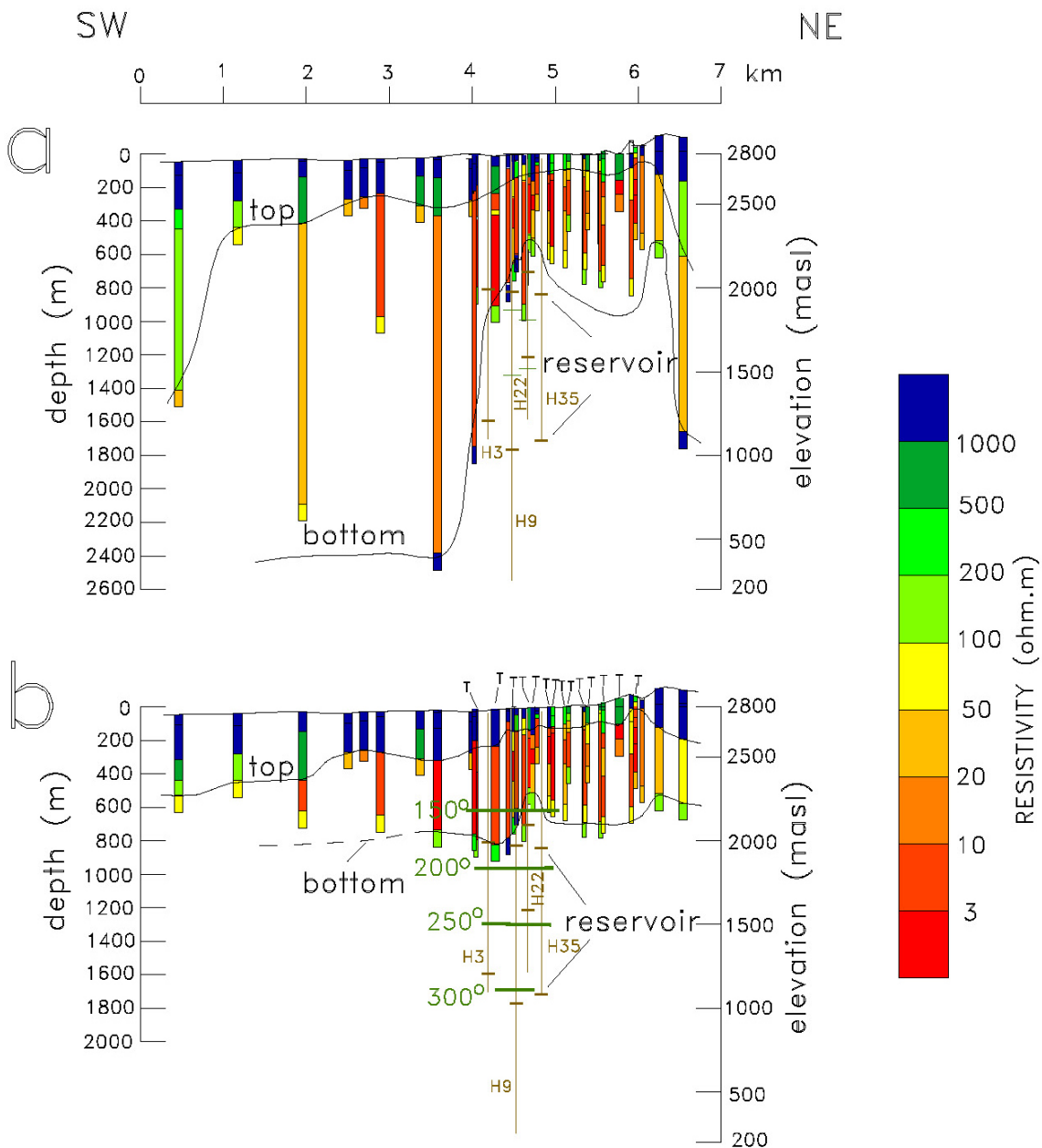


Figure 5. Alternative resistivity sections under profile P1. a) Preliminary model, b) Reinterpreted model. The top and bottom of the conductive unit is defined by resistivities less than 100 ohm.m. Vertical exaggeration of 2x. The depth interval of the geothermal reservoir is indicated in the wells and a simplified version of the initial temperatures. The "Ts" denote the TEM soundings.

The section of Figure 5a shows several anomalous features, such as the thickening of almost 2 km of the conductor in the southwestern part of the profile and abrupt changes in the top or bottom boundaries of the conductor in the northeastern part of the model. Before attempting any interpretation of these features in terms of the structure of the geothermal system, we carried out a sensitivity analysis to estimate how well resolved are the different parameters (resistivities and layer thicknesses)

of the stratified models. This approach, based on the Singular Value Decomposition (SVD) of the Jacobian matrix (Edwards *et al.*, 1981) has been used in different geophysical studies (e.g., Verma and Sharma, 1995; Key and Lockwood, 2010; García-Fiscal and Flores, 2018) to assess which parts of the models are well constrained by the data and which are not. This approach is used only after an adequate fit between the measured and calculated responses has been reached in the inversion process. The sensitivities or Jacobians are approximated by

$$a_{ij} = \frac{p_j}{\varepsilon_i} \frac{dy_i}{dp_j},$$

where dy_i is the change in the i th response due to a small change in the j th parameter dp_j , and ε_i is the uncertainty in the i th measured response. The geophysical response y_i can be the apparent resistivity in the VES case or the voltage in the TEM soundings, and p_j is the natural logarithm of the resistivity or thickness of any layer in the model. By using SVD, the Jacobian matrix A , containing the sensitivities a_{ij} , can be decomposed into the product of three matrices $A=USV^T$ known as the eigendata, singular value, and eigenparameter matrices, respectively, where T stands for the transpose. An estimate of the upper and lower bounds of the j th parameter uncertainty are obtained from the expression proposed by Raiche *et al.* (1985),

$$p_j \pm = p_j \exp(\pm \sigma B_j)$$

where σ is the misfit error, and B_j is defined by

$$B_j = \left[\sum_{i=1}^N (V_{ji} / S_i)^2 \right]^{1/2},$$

where V_{ji} and S_i are elements of the eigenparameter and singular value matrices,

respectively.

As an example of the use of this approach to our data, in Figure 6 we show it for two pairs of close-by resistivity and TEM soundings which are less than 100 m apart. Figure 6a compares the TEM sounding T24 with the resistivity sounding S954, while Figure 6b does the same for the T5 with the S3017. In the upper part the layer resistivities of the inverted models are displayed. The bars in the resistivities and depths to the layer interfaces indicate the uncertainties in these parameters. When one parameter is poorly resolved the estimated errors are extremely high. This is because the SVD technique is based on the linearization of a non-linear problem (Edwards *et al.*, 1981). These large uncertainties are marked with an asterisk in Figure 6. The comparison between calculated and observed apparent resistivities is shown in the lower part of the figure, where symbols correspond to the measured values and their estimated standard errors displayed as error bars. The error bars in the resistivity soundings were estimated from the clutches (known as "empalmes" in Spanish), which are those apparent resistivities measured with one current electrode separation but at least two potential-electrode apertures. The errors in the TEM responses were estimated from the standard deviations of the post-stacked voltages. Notice the large uncertainties in the TEM response for late times, presumably a result of noise. From this analysis the following points can be inferred:

- a) Shallow layering located at depths less than 200 m are detected and well resolved by the resistivity soundings. However, the TEM soundings distinguish only one layer in both soundings and are particularly not well resolved for the model of T5. This is an expected result because the shal-

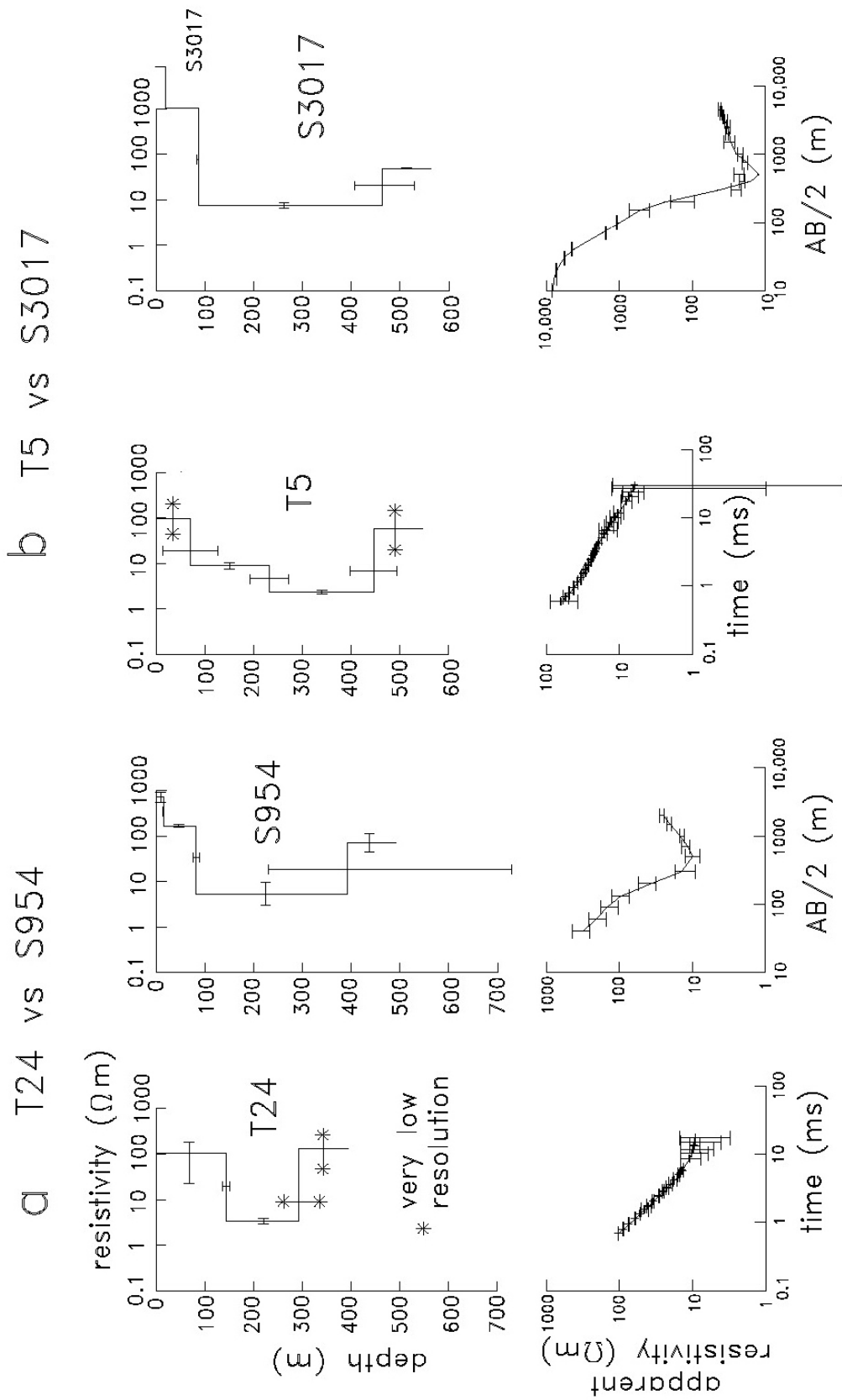


Figure 6. Comparison of inverted models and parameter resolution between a pair of close-by transient electromagnetic (TEM) and resistivity soundings. a) Soundings T24 and S954, b) soundings T5 and S3017. Large uncertainties (low resolution) are indicated with an asterisk. The measured apparent resistivities and standard errors as a function of electrode aperture or time are displayed in the lower part, together with the calculated response from the inverted model.

low part in the transient electromagnetic soundings depends on the shortest recording time after the current shut-off (Spies, 1989), which typically was 700 microseconds. With large loops, such as those used in this study, the loop's self-inductance impedes the use of shorter times.

- b) Both methods resolve fairly well the top to the conductor.
- c) For the second pair of soundings (T5-S3017) the resolution of the thickness of the conductive layer is acceptable. However, for the first pair (T24-S954) the thickness and resistivity of this layer are not well resolved. This is due to an equivalence problem that affected many soundings. This problem will be discussed below.
- d) The resistivity of the underlying resistive unit sometimes is well resolved by the VES; however, the TEM soundings do not resolve this parameter.

This equivalence problem is illustrated with sounding S109 in Figure 7 where four possible models are displayed. These models have the same conductance (the ratio of thickness over resistivity) in the low-resistivity layer but the individual resistivity and thickness are different. The apparent resistivity responses from the four models are shown in the right panel, the differences between them are so small that they cannot be differentiated. According to Orellana (1972), the equivalence in the conductance of a layer occurs with thin and low-resistivity layers, particularly, when the layer transverse resistance (the product of thickness by resistivity) is much less than the cumulative transverse resistance of all the overlying layers. For this model, the cumulative resistance is more than 35 times greater than the resistance of the conductive layer. Then, the practical consequence of this equivalence problem is that there are many pairs of thickness and resistivity of this layer that fulfill the data; it is a non-uniqueness problem, common to several geophysical methods.

Information external to the geophysical method has to be used to solve the equivalence problem. Over the reservoir, the well temperatures and their associated hydrothermal alteration were employed to constrain the base of the conductive zone. As mentioned above, the conductive clay-cap is produced by the presence of smectite and illite, hydrothermal minerals occurring at temperatures between 70° and 200°C. Then, in Figure 5b the bottom of the conductive zone was set at the depth corresponding to the vicinity of 180°C, where these two argillic minerals show a gradual content decrease. For soundings not located over the reservoir, we constrained the models to have a smooth lateral variation in the top and bottom of the conductive unit, done by trial and error in a site-by-site basis. This reinterpretation process for the resistivity soundings was carried out in about 45% of the soundings with an in-house non-linear inversion program based on the algorithm proposed by Jupp and Vozoff (1975) which considers the standard deviation of the data, something that the commercial program ignores. It is important to emphasize that the two models of Figure 5 reproduce the observed data equally well, such that both of them are valid. However, we prefer the second model (Figure 5b) because it is constrained by *a priori* information. In the first model (Figure 5a) anomalous features in the model could have been given geothermal significance when the equivalence problem in fact produces them.

The same two constraints mentioned above were applied to the four profiles of Figures 8 and 9. Profiles P2, P3, and P5 have a NW-SE azimuth, P4 is SW-NE; their locations are indicated in Figure 2. Profile P5 is the only one not passing over the production zone. From these models (Figures 5b, 8, and 9) we can infer the following general features:

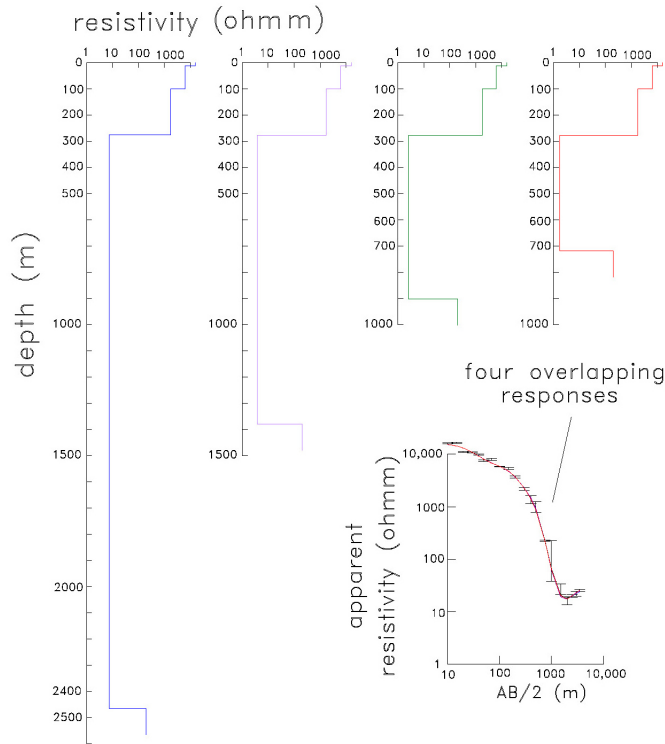
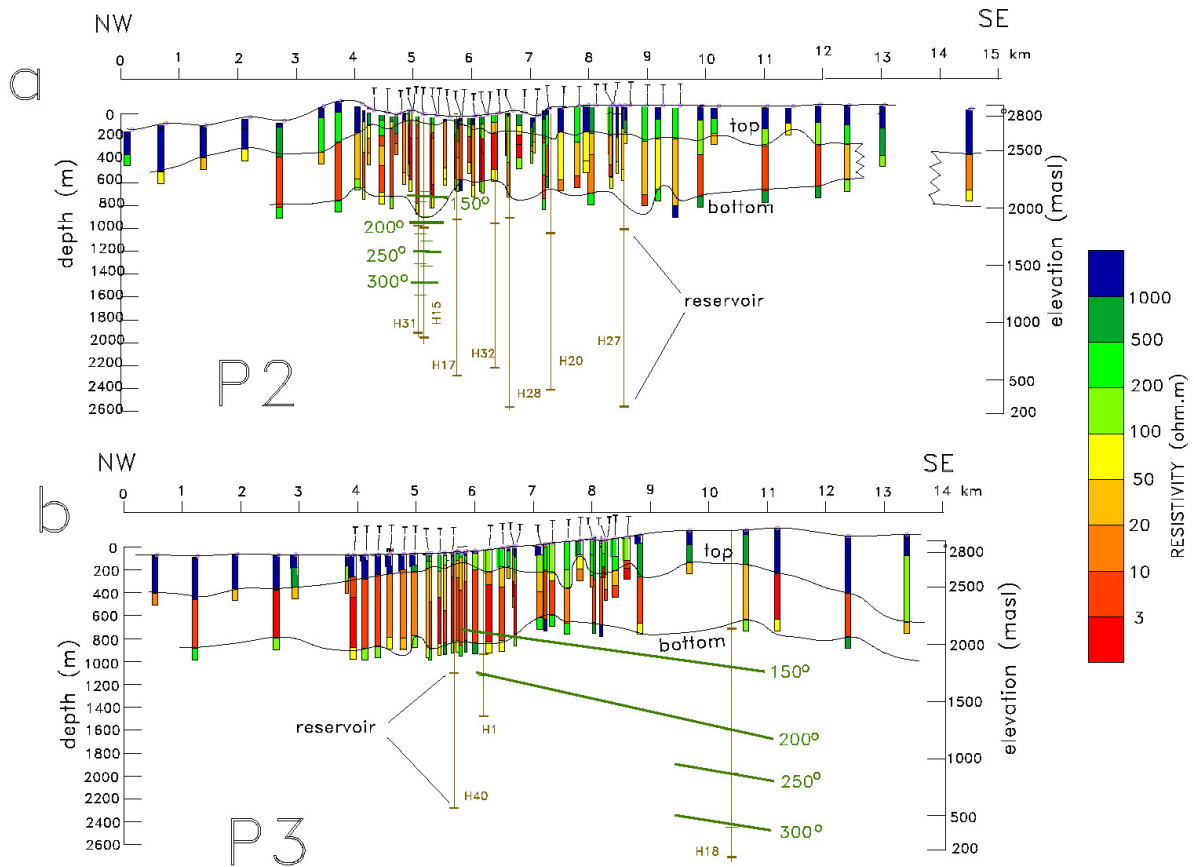


Figure 7. Equivalence problem in the resistivity sounding S109. Four models with the same conductance of the fourth layer produce practically the same apparent resistivity responses. The field data are also shown.

Figure 8. Reinterpreted models constructed for the NW-SE profiles P2 and P3. Profile locations are shown in Figure 2. The top and bottom of the conductive unit is defined by resistivities less than 100 ohm.m. Vertical exaggeration of 2x. The geothermal reservoir is indicated in the wells and a simplified version of the initial temperatures. The "Ts" denote the TEM soundings



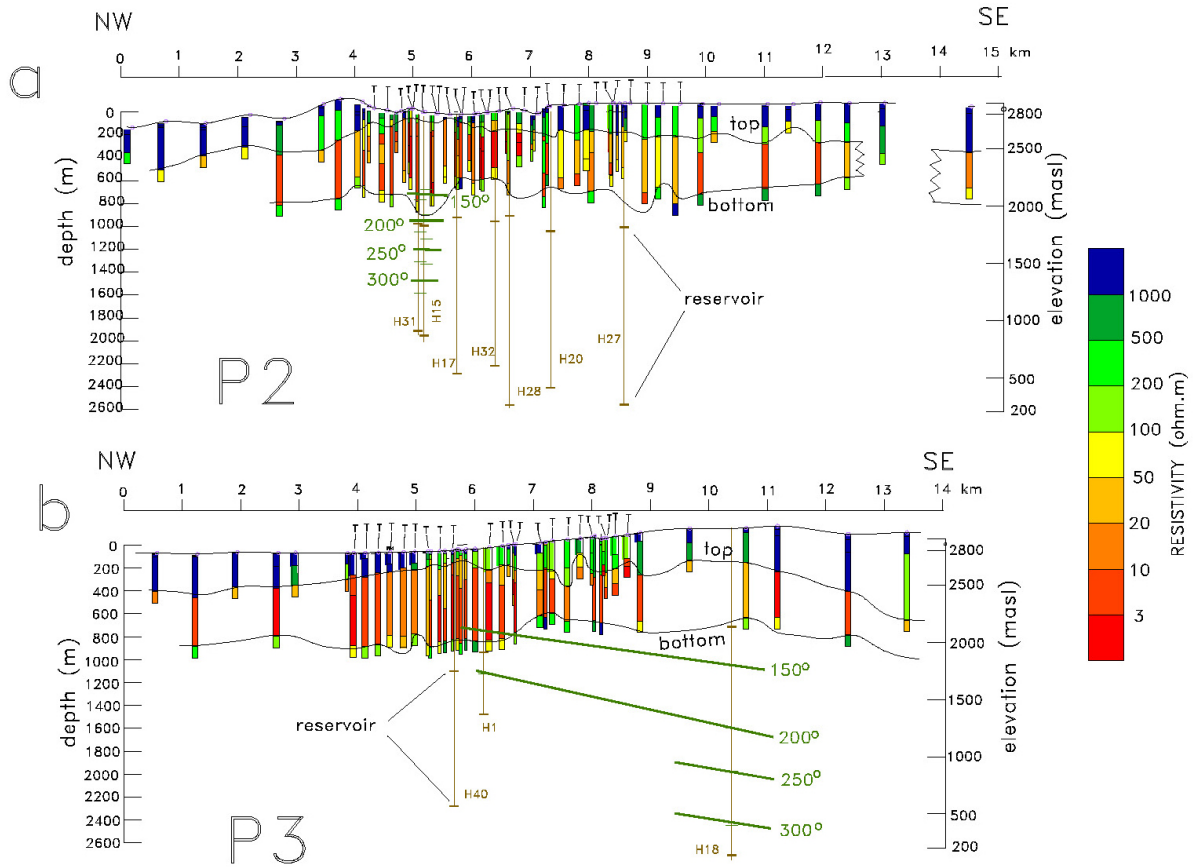


Figure 9. Reinterpreted models constructed for profiles P4 (SW-NE) and P5 (NW-SE). Profile locations are shown in Figure 2. The top and bottom of the conductive unit is defined by resistivities less than 100 ohm.m. Vertical exaggeration of 2x. The geothermal reservoir is indicated in the wells and a simplified version of the initial temperatures. The “Ts” denote the TEM soundings.

- a) The top of the clay cap tends to be shallower over the reservoir;
- b) The resistivity of the clay cap tends to be lower over the reservoir;
- c) The clay cap not only occurs over the geothermal reservoir (as in Figure 1) but is present under the whole area of study.
- d) Not all measurements sensed the top of the deep resistive unit; soundings with half-separations of 2 km or less, such as soundings 601 and 650 of Figure 3, could not detect the resistive layer underlying the clay cap.

MAP DISTRIBUTION OF MODEL PARAMETERS

We now turn to analyze the horizontal distribution of the resistive-conductive-resistive structure. Here we will focus on the results from the resistivity soundings because of its greater areal coverage. It is worth mentioning that the parameters are quite irregular, however, global trends can be drawn. The shallow resistive unit is made by up to five layers, but two and three layers contribute 87% of all the models. The average thickness of this unit is 240 m. To obtain an equivalent resistivity (ρ_{eq})

for this unit, in each sounding we used the following approximation (Maillet, 1947), $\rho_{eq} = \frac{\sum \rho_i t_i}{\sum t_i}$, where ρ_i and t_i are the resistivity and thickness of each layer, respectively, and the sum is over the number of layers. The average for the whole area is 1600 ohm·m, with the lower and upper bounds defined by one standard deviation are 700 and 3900 ohm·m. These bounds are not symmetric because the averaging was performed in the logarithmic space. Figure 10 shows a map of the equivalent resistivity where areas with resistivities less than 1,000 ohm·m are highlighted in red. These low-resistivity zones occur over the geothermal reservoir, in the vicinity of the Los Humeros ring fracture, and in a wide zone in the southern section of the study area (Figure 10). They could be due to rock volumes where the geothermal fluids and their associated argillic alterations reached shallow depths or fractured volcanic rocks saturated with groundwater which allow the percolation of meteoric water, that is, recharge zones. The southern zone could represent the mountain-front recharge area

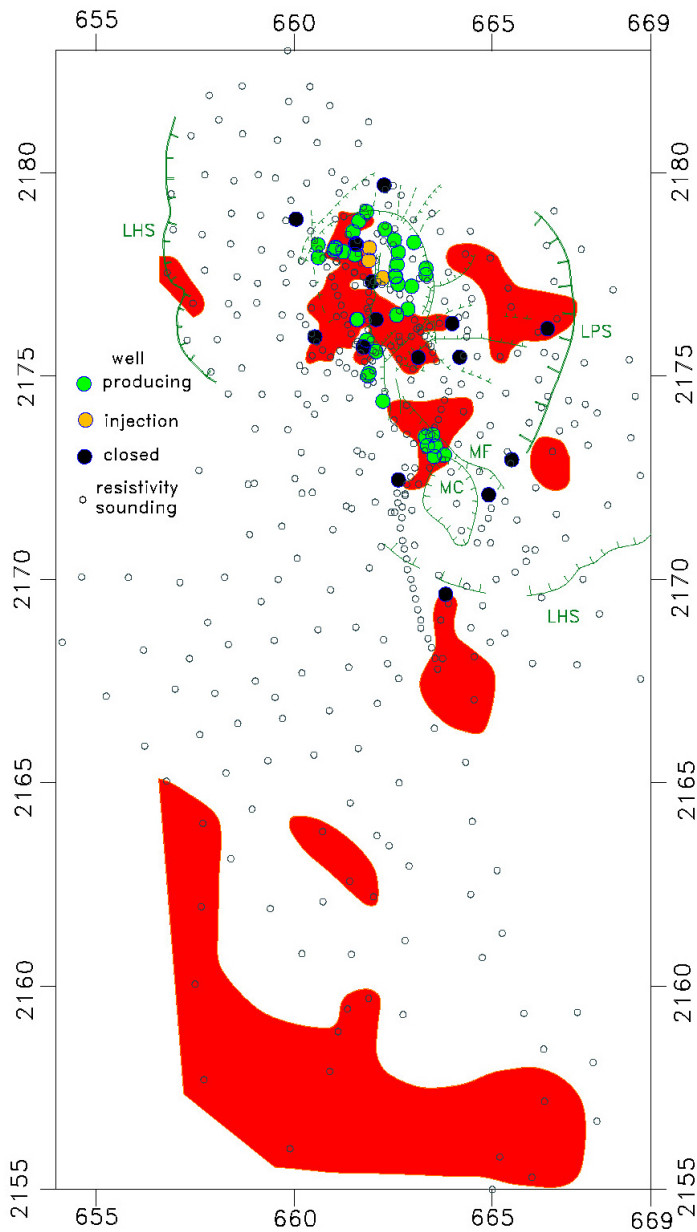


Figure 10. Equivalent resistivity of the shallow resistive unit. Red zones enclose values less than 1,000 Ωm. The main faults are also depicted.

associated with the Cofre de Perote topographic high. These anomalous zones do not seem to be correlated with a particular lithology of the mapped surface geology by Carrasco-Núñez, *et al.* (2017).

Another interesting feature is that there is no evidence of a continuous low-resistivity zone within this resistive unit that could be associated with an aquifer, as is usually the case in a sedimentary basin. This is supported by eight exploration wells reported by Cedillo (1999) (maximum depths from 210 to 360 m), four of them located inside the Los Humeros Caldera and four outside. Only in five of them a phreatic level was detected but at significantly different depths. This suggests they are associated with local aquifers because the regional piezometric surface could not be defined. This indicates that secondary permeability is the controlling factor in the resistive unit.

In the profiles above we noticed that the depth to the top of the conductive unit apparently is shallower where the reservoir is located. Figure 11 shows the spatial behavior of this unit displayed by the depth contours of 200 and 400 m below the surface. Depths shallower than 200 m occur mainly over the production zone. The other zone with shallow depths is located in the southwestern corner of the study area. If a direct relationship exists between a shallow clay cap and the presence of a geothermal reservoir, it would be worth to further explore this southern zone. An alternative explanation for this zone is that an old thermal episode produced the hydrothermal clay alteration but now the temperatures are not sufficiently high for the existence of a geothermal reservoir. The mean resistivity of the conductive unit is $8.7 \pm 6.8 \text{ ohm}\cdot\text{m}$.

Figure 12 shows the conductance of this conductive unit where values greater than 100 Siemens are enclosed by the red contour and are mainly concentrated above the reservoir. It is worth noting the high lateral variability of this parameter, which could be explained by the formation in vertical fractures and faults of the alteration clays.

One last subsurface parameter we analyze is the resistivity of the layer below the clay cap, that is, the deep resistive unit. Many soundings either could not detect this unit or they did not have enough points in the ascending apparent resistivity data to adequately resolve this resistivity. In these cases, the maximum electrode separations of the Schlumberger soundings were not large enough to reach greater depths of investigation. Examples of these responses are soundings 650, 941, and 601, shown in Figure 4. However, 26 soundings rendered models with a deep resistivity reasonably well resolved, such as that of sounding 111 (Figure 4). In this group, the average depth to the top of this deep resistive unit is 600 m. By employing a perturbation analysis on several of these models we estimate this unit extends to depths of the order of 2 km. For this analysis we assumed the presence of an additional test layer with a starting depth to its top of 5 km and resistivity two times or half the value of the deep resistive unit. We then decreased in steps the depth of this test layer, calculating the apparent resistivity response in each step. When the depth was about 2 km the apparent resistivities of the largest electrode separations started to fall beyond the error bars of the measured response, suggesting this as the maximum depth of investigation of these soundings.

The deep resistivities and corresponding uncertainties of the 26 models are displayed in Figure 13. They are sorted into two groups: on the left side of this figure are 16 soundings falling in the drilled area, on the right side are 10 soundings located more than 2 km away from any nearby well. Additionally, the first 11 values of the left group (soundings 88 to 3082) correspond to those located less than 500 m from a producing well, the remaining five soundings do not have a close producing well. The logarithmic means of the three resistivity groups (109, 141, and 150 $\text{ohm}\cdot\text{m}$) and the

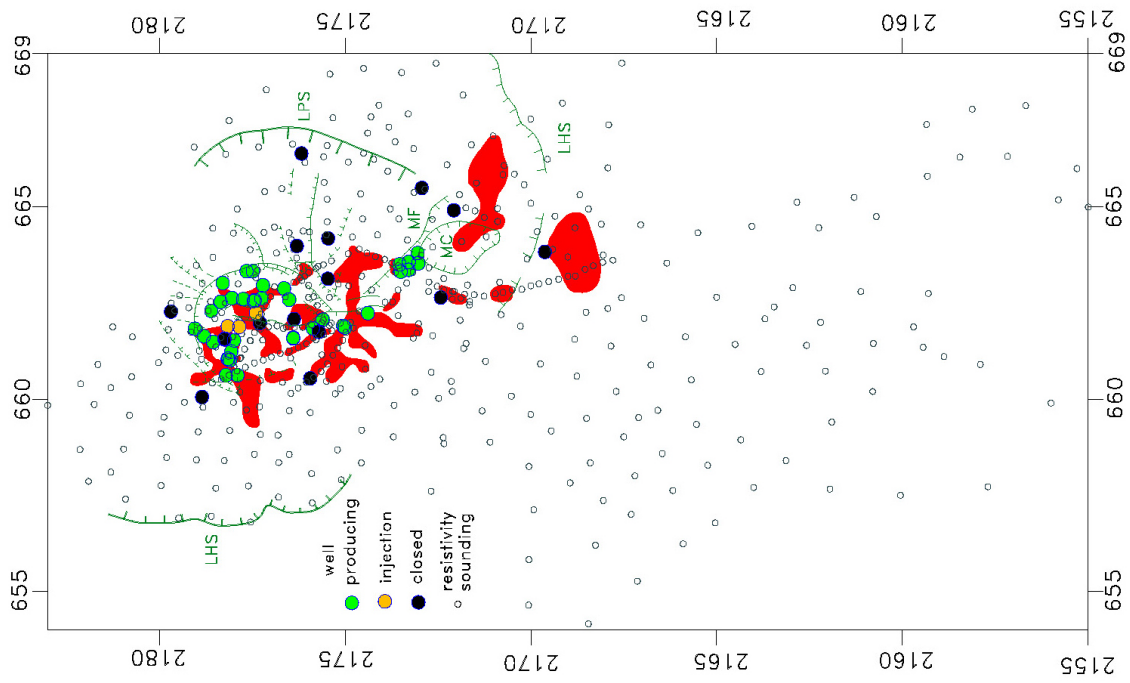


Figure 11. Depths to the top of the conductive unit. Red areas: depths less than 200 m; green areas: depths between 400 and 200 m. The locations of the main faults are also shown.

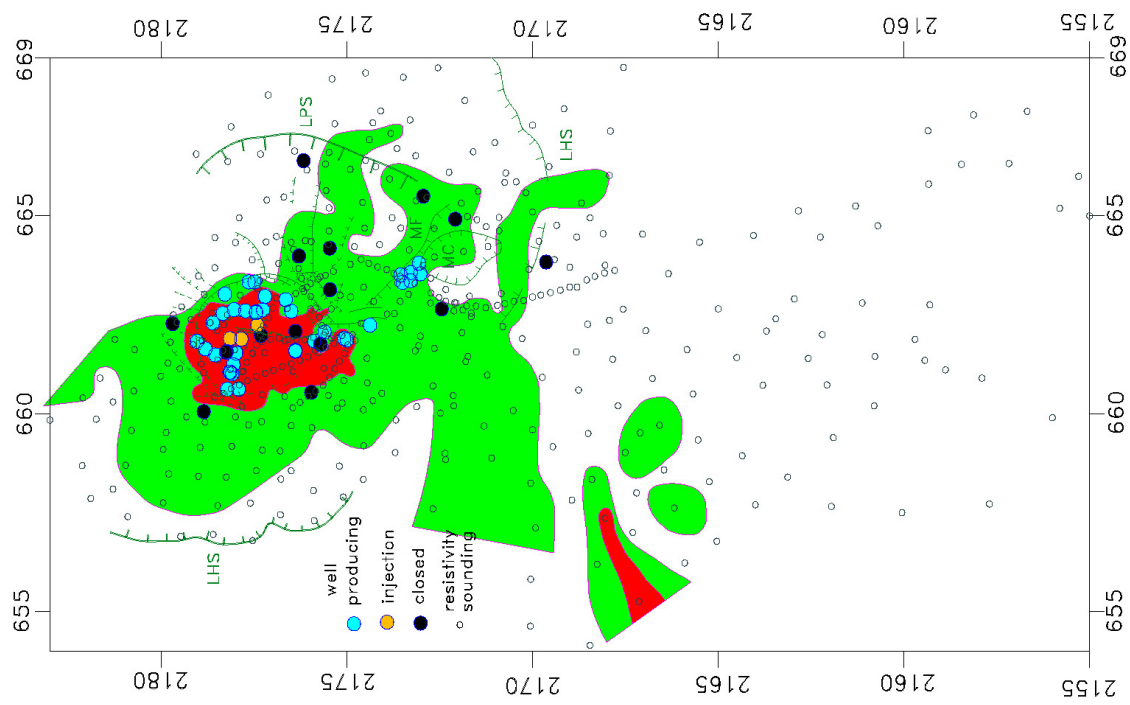


Figure 12. Conductances of the conductive unit higher than 100 Siemens are displayed in red. The locations of the main faults are also shown.

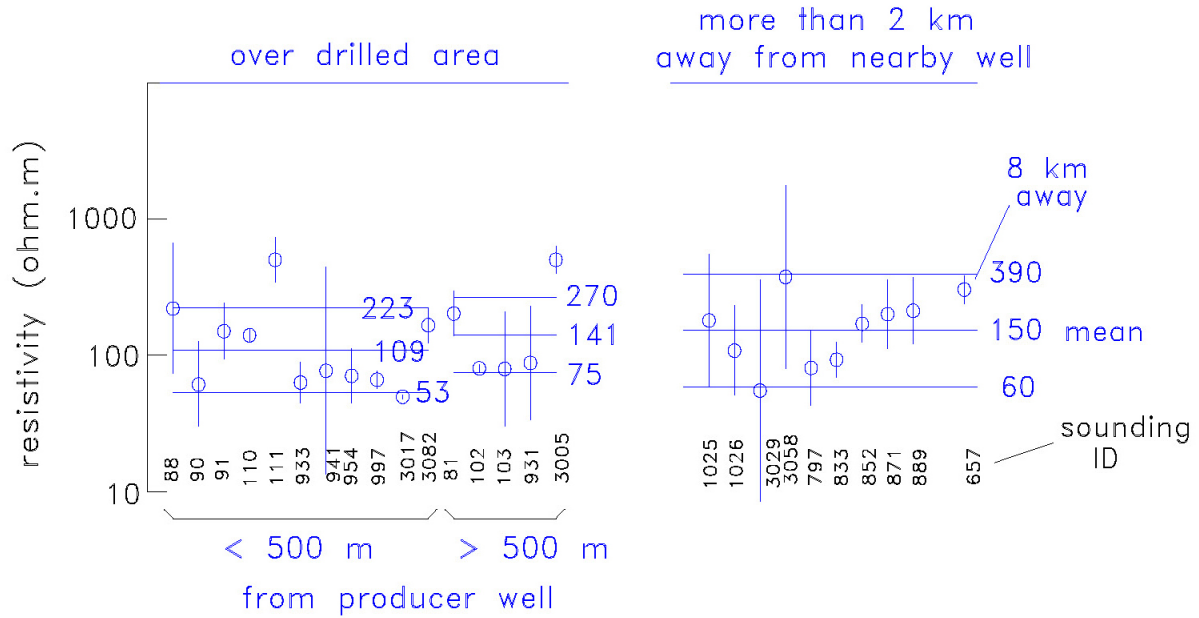


Figure 13. Well resolved resistivities of the deep resistive unit. The individual uncertainties are displayed with error bars. The global average and standard errors are also shown.

corresponding uncertainties (defined by +/- one standard deviation) are indicated in this figure with the horizontal lines. Because the uncertainties overlap, statistically the average resistivities of the three groups are indistinguishable from each other. The average value of the 16 soundings within the drilled area is 118 ohm·m.

DISCUSSION

The resistivity structures inferred from neighboring VES and TEM soundings are similar but rarely are the same. Several factors may explain these differences, among them is the different attitudes the electric currents have in the subsurface; while in the TEM method the induced currents tend to be horizontal, in the DC galvanic technique the injected currents have both horizontal and vertical components. They also have different depths of investigation. For example, in shallow depths the VES can distinguish vertical resistivity changes in the first few meters, while the shallowest interface the TEM soundings can detect is of the order of 200 m (Spies, 1989). Furthermore, the lateral dimensions of the subsurface volume that contributes to a given surface voltage measurement are different; in the TEM soundings the maximum lateral dimensions are of the order of several hundred meters, while in the VES soundings, depending on the maximum AB/2 electrode separation, they can reach several kilometers. Therefore, the TEM soundings are expected to have a better lateral resolution.

The resistivity and TEM data could, at least in theory, be inverted to a 3D model. However, this is a difficult task for the large size of the matrices involved in the inversion. For example, assuming the use of a finite differences inversion approach, would require defining grid nodes at each of the current and potential electrodes, which would require at least 22,000 nodes to model all the VES data; the size of the resulting matrices would be hard to handle. Furthermore, the coordinates of the center of each sounding are known, but not the required x,y position of the electrodes.

The recharge zone, where meteoric water percolates and feeds the deep hydrothermal fluids, is an important component of any conceptual model of a geothermal field. There are two trends on where the recharge zone is located. Cedillo Rodríguez (1999) suggests a local recharge zone situated within the Los Humeros caldera, where the various mapped faults work as the downward conduits of rainwater. Other studies (Yáñez, 1980; Pinti *et al.*, 2017; Les Landes *et al.*, 2020; Lelli *et al.*, 2021) support a regional recharge from the nearby outcropping Mesozoic limestones of the Sierra Madre Oriental. Figure 10 outlines the areas where the shallow resistive unit has equivalent resistivities less than 1000 ohm m. They occur mainly over the geothermal field and a large zone in the southern edge of the study area; their decreased resistivities could be produced by the presence of water in enhanced permeability zones, which could represent recharge zones. The low resistivity zone in the vicinity of the reservoir would favor the proposal of Cedillo Rodríguez (1999) of a local recharge zone, while the region in the southern limit of the study area would suggest a regional recharge zone. As we do not have any sounding over the Mesozoic calcareous rocks, we cannot estimate the possible contribution to the recharge from this type of outcrops.

The results displayed in Figure 13 are important for the search of a link between the deep resistivity and the presence of the geothermal reservoir. In this figure we sorted the deep resistivities according to the distance to a drilled well. In the first group are those soundings located less than 500 m from a productive well, in the second, those positioned within the drilled area but more than 500 m from any productive well, and in the third those situated outside the drilled area and more than 2 km from any nearby well. The lower average value of the first group (109 ohm·m) with respect to those of the second (141 ohm·m) and third (150 ohm·m) groups could be interpreted as the effect of hot and saline fluids residing in the near-vertical fractured rocks of the geothermal reservoir, decreasing the rock resistivity. Unfortunately, the uncertainties of the inverted resistivities and the overlapping of the standard deviations of the average values (Figure 13) preclude confirming such correlation. The higher mean value of the third group (150 ohm·m) with respect to those of the first and second groups could be due to an absence of hot geothermal fluids. But again, these resistivities are not statistically different, such that this claim cannot be assured.

Assuming that 8 km south of the drilled area (where sounding 657 is located) there is no geothermal reservoir, the deep resistivity value of 303 ohm·m obtained for this sounding (Figure 13) could be produced by the presence of chlorite, a hydrothermal alteration mineral that decreases the resistivity, but not to the extent as lower temperature minerals such as smectite does. The presence of this intermediate resistivity, together with the generalized occurrence of the conductive unit suggests the existence of one or several thermal events that produced this regional presence of alteration minerals.

The average value of 109 ohm·m of the resistive unit representing the reservoir is higher than the upper limit of 60 ohm·m proposed by Pellerin *et al.* (1996) in their conceptual model depicted in Figure 1. To test how common is this 10 to 60 ohm·m interval for the so-called resistive core, we carried out a survey of published literature in geothermal fields around the world that report wells with temperatures of at least 200 °C and estimated resistivities at these depths, the result of inversion of geophysical data (usually with the magnetotelluric method). We found published papers on 28 geothermal fields that fulfilled these two requirements. The results are shown in Table 1 and displayed in Figure 14 as a histogram with three resistivity divisions per decade. Although the most common occurrence is from 20 to 50 ohm·m, geothermal fields with reservoir resistivities from 100 to 200 ohm·m are not uncommon. Then, the mean value of 109 ohm·m for the Los Humeros reservoir resistivity cannot be considered anomalous.

Figure 14. Histogram of the reservoir resistivities of the 28 geothermal fields reported in Table 1.

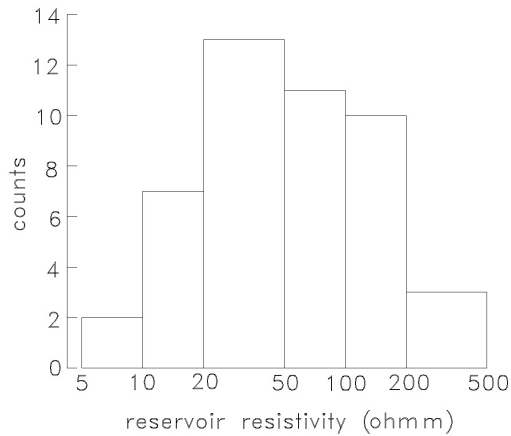


Table 1. Estimated reservoir resistivities in geothermal fields around the world.

Geothermal field	resistivity (Ωm)	Source
Hengill, Iceland	~ 150	Arnasson <i>et al.</i> , 2010
Ohaaki, New Zealand	50 to 100	Bertrand <i>et al.</i> , 2012
Aluto-Langano, Ethiopia	20 to 50	Cherkose & Mizunaga, 2018
Glass Mountain, USA	100 to 150	Cumming and Mackie, 2010
Krafla, Iceland	30 to 80	Gasperikova <i>et al.</i> , 2011
Namora, Indonesia	8 to 25	Gunderson <i>et al.</i> , 2000
Awibengkok, Indonesia	15 to 30	Gunderson <i>et al.</i> , 2000
Rotokawa, New Zealand	~ 100	Heise <i>et al.</i> , 2008
Krýsuvík, Iceland	3 to 200	Hersir <i>et al.</i> , 2020
Northern Negros, Philippines	20 to 60	Layugan <i>et al.</i> , 2005
Southern Leyte, Philippines	40 to 100	Layugan <i>et al.</i> , 2005
Mahagna, Philippines	30 to 60	Layugan <i>et al.</i> , 2005
Coso, USA	40 to 200	Lindsey <i>et al.</i> , 2017
Mahanagdong, Philippines	20 to 50	Los Baños & Maneja, 2005
Travale, Italy	200 to 500, 250 & 60 to 90	Manzella <i>et al.</i> , 2010
Tolhauaca, Chile	30 to 60	Melosh <i>et al.</i> , 2010
Mutnov, Russia	60 to 100	Nurmukhamedov <i>et al.</i> , 2010
Lahendong, Indonesia	15 to 40	Raharjo <i>et al.</i> , 2010
Kamojang, Indonesia	50 to 150	Raharjo <i>et al.</i> , 2010
Irruputuncu, Chile	~ 20	Reyes <i>et al.</i> , 2011
Asal, Djibouti	26	Sakindi, 2015
Aluto-Langano, Ethiopia	10	Samrock <i>et al.</i> , 2015
Sumikawa, Japan	100 to 200 & 300	Uchida, 1995
Mataloko, Indonesia	100 to 200 & 300	Uchida <i>et al.</i> , 2002 & Uchida, 2005
Ogiri, Japan	200	Uchida, 2010
Yanaizu-Nishiyama, Japan	10 to 30	Uchida <i>et al.</i> , 2011
Takigami, Japan	100 to 200	Ushijima <i>et al.</i> , 2005
Sabalan, Iran	20 to 30	Talebi <i>et al.</i> , 2005
Dixie Valley, USA	70 to 200 & ~ 100	Wannamaker <i>et al.</i> , 2007

It is interesting to compare the deep resistivities at reservoir depths estimated with the VES soundings with those obtained with the Magnetotelluric (MT) method. There are two MT field data, those acquired in the CeMie-GEO project (Arzate *et al.*, 2018), and those measured in the GEMex project (Benediktsdóttir *et al.*, 2020). They have been interpreted using 1D (Romo-Jones *et al.*, 2020), 2D (Arzate *et al.*, 2018), and 3D inversion approaches (Corbo-Camargo *et al.*, 2020; Benediktsdóttir *et al.*, 2020; Romo-Jones *et al.*, 2021). Focusing in the 3D results, it is not easy to carry out comparisons between the modeled resistivities because the analyzed profiles in these works are different. However, the models close to producing wells can be compared. In the vicinity of productive wells H-7 and H-8 the resistivities in the depth range of the reservoir are: 50 to 200, 15 to 170, and 15 to 120 $\text{ohm}\cdot\text{m}$ given, respectively, by Corbo-Camargo *et al.*, 2020, Benediktsdóttir *et al.*, 2020, and Romo-Jones *et al.*, 2021. Close to another productive well H-19, the resistivities are about 200, 15 to 50, and 5 to 200 $\text{ohm}\cdot\text{m}$, respectively, from the same articles in the same order. Although there are obvious differences between the MT results and also with our results (50 to 220 $\text{ohm}\cdot\text{m}$, Figure 13), the ranges of variation overlap in several cases.

CONCLUSIONS

With the interpretation of DC resistivity and transient electromagnetic soundings we found a global resistive-conductive-resistive vertical sequence. The shallow resistive unit has an average thickness and resistivity of 240 m and 1600 $\text{ohm}\cdot\text{m}$, respectively. There are two low-resistivity zones within this unit, over the reservoir and in the southern region; these might be recharge zones where the downward circulation of meteoric water feeds the reservoir.

The resistivity and thickness of the conductive unit, interpreted as the clay cap, cannot be estimated separately due to an equivalence problem. This was circumvented by using the well temperatures and their association with the argillic hydrothermal alteration. The average thickness and resistivity of this unit are 440 m and 7.4 $\text{ohm}\cdot\text{m}$, respectively. The depth to the top tends to be shallower and their resistivities have lower values over the reservoir. We propose that these features could be used as proxy indicators of a geothermal reservoir in other prospective areas. The conductive unit appears under the whole studied area, indicating a regional hydrothermal alteration, possibly resulting from several thermal events.

In 26 VES models the resistivities of the third unit were well resolved with reasonable small uncertainties; these depths correspond to where the geothermal reservoir lies, with average values from 100 to 150 $\text{ohm}\cdot\text{m}$. The resistivities close to productive wells have average values slightly lower than those far from the wells, unfortunately their uncertainties overlap, such that they are not statistically different from each other. There are partial agreements between our resistivities and those estimated from previous magnetotelluric inversions. To examine how common is our estimated range of resistivities compared with other geothermal fields in the world, we searched for published studies with wells with temperatures over 200 °C and estimated reservoir resistivities with geophysics, finding 28 of them. Our range of 100 to 150 $\text{ohm}\cdot\text{m}$ is not the most frequent, but represents a significant 36% of all the cases.

ACKNOWLEDGEMENTS

We thank Gerencia de Proyectos Geotermoeléctricos from CFE for kindly providing the data. We particularly acknowledge the effort and dedication of CFE geophysical staff which acquired the direct current data during several years of field work.

REFERENCES

- Anderson, E., Crosby, D., and Ussher, G., 2000, Bulls-eye! – Simple resistivity imaging to reliably locate the geothermal reservoir, *Proc. World Geothermal Congress*, 909-914.
- Arellano Gómez, V.M., García, A., Barragán, R.M., Izquierdo, G., Aragón, A., and Nieva, D., 2003, An updated conceptual model of the Los Humeros geothermal reservoir (Mexico), *J. Volcanol. Geoth. Res.*, 124, 67-88 doi:10.1016/S0377-0273(03)00045-3
- Arnason, K., Eysteinnsson, H., and Hersir, G.P., 2010, Joint 1D inversion of TEM and MT data and 3D inversion of MT data in the Hengill area, SW Iceland, *Geothermics*, 39, 13-34 doi:10.1016/j.geothermics.2010.01.002
- Arzate, J., Corbo-Camargo, F., Carrasco-Núñez, G., Hernández, J., and Yutsis, V., 2018, The Los Humeros (Mexico) geothermal field model deduced from new geophysical and geological data, *Geothermics*, 71, 200-211 <http://dx.doi.org/10.1016/j.geothermics.2017.09.009>
- Benediktsdóttir, A., Hersir, G.P., Vilhalmsson, A.M., Manzella, A., Santilano, A., and Held, S., 2020, Report on resistivity modeling and comparison with other SHGS, Deliverable 5.2, GEMex, Postdam Meeting, 165 pp. www.gemex-h2020.eu
- Berkthold, A., 1983, Electromagnetic studies in geothermal regions, *Geophys. Surv.*, 6, 173-200.
- Bertrand, E.A., Caldwell, T.G., Hill, G.J., Bennie, S.L., and Soonkono, S., 2013, Magnetotelluric imaging of the Ohaaki geothermal system, New Zealand: Implications for locating basement permeability, *J. Volcanol. Geotherm. Res.*, 268, 36-45 <http://dx.doi.org/10.1016/j.volgeo.2013.10.010>
- Campos-Enríquez, J.O., and Arredondo-Fragoso, J.J., 1992, Gravity study of Los Humeros Caldera complex, Mexico: structure and associated geothermal system, *J. Volcanol. Geoth. Res.*, 49, 69-90 [https://doi.org/10.1016/0377-0273\(92\)90003-x](https://doi.org/10.1016/0377-0273(92)90003-x)
- Carrasco-Núñez, G., Arzate, J., Bernal, J.R., Carrera, J., Cedillo, F., Dávila-Harris, P., Hernández, J., Hurwitz, S., Lermo, J., Levresse, G., López, P., Manea, V., Norini, G., Santoyo, E., and Wilcox, C., 2015, A new geothermal exploration program at Los Humeros volcanic and geothermal field (eastern Mexican Volcanic Belt), *Proc. World Geothermal Congress*, Melbourne, Australia.
- Carrasco-Núñez, G., López-Martínez, M., Hernández, J., and Vargas, V., 2017, Subsurface stratigraphy and its correlation with the surficial geology at Los Humeros geothermal field, Eastern Trans-Mexican volcanic belt, *Geothermics*, 67, 1-17 <http://dx.doi.org/10.1016/j.geothermics.2017.01.001>
- Cedillo Rodríguez, F., 1999, Modelo hidrogeológico de los yacimientos geotérmicos de Los Humeros, Pue., México, *Geotermia, Rev. Mex. de Geoenergía*, 15(3), 159-170.
- Cherkose, B.A., and Mizunaga, H., 2018, Resistivity imaging of Aluto-Langano geothermal field using 3-D magnetotelluric inversion, *J. of African Earth Sciences*, 139, 307-318 <https://doi.org/10.1016/j.jafrearsci.2017.12.017>
- Corbo-Camargo, F., Arzate, J., Fregoso, E., Norini, G., Carrasco-Núñez, G., Yutsis, V., Herrera, J., and Hernández, J., 2020, Shallow structure of Los Humeros (LH) caldera and geothermal reservoir from magnetotelluric and potential field data, *Geophys. J. Int.*, 223, 666-675 doi:10.1093/gji/ggaa338
- Cumming, W., and Mackie, R., 2010, Resistivity imaging of geothermal resources using 1D, 2D and 3D MT inversion and TDEM static shift correction illustrated by a Glass Mountain Case History, *Proc. World Geothermal Congress*, Bali Indonesia, 1-10.

- Deb, P., Giordano, G., Shi, X., Lucci, F., and Clauser, C., 2021, An approach to reconstruct the thermal history in active magmatic systems: Implications for the Los Humeros volcanic complex, Mexico, *Geothermics*, 96, 102162 <https://doi.org/10.1016/j.geothermics.2021.102162>
- Edwards, R.N., Bailey, R.C., and Garland, G.D., 1981, Conductivity anomalies: lower crust or asthenosphere?, *Physics Earth Planet. Interiors*, 25, 263-272.
- Ferriz, H., 1982, Geologic and preliminary reservoir data on the Los Humeros geothermal system, Puebla, Mexico, *Proc. Eight Workshop on Geothermal Reservoir Engineering*, 19-24, Stanford University.
- Flores, C., Alvarez, R., Singh, S.K., and Urrutia, J., 1977, Aeromagnetic survey of Los Humeros caldera, Mexico, *Geof. Intern.*, 17, 4145-428.
- Flóvenz, O.G., Georgsson, L.S., and Árnason, K., 1985, Resistivity structure of the upper crust in Iceland, *J. Geophys. Res.*, 90(B12), 10136-10150 <https://doi.org/10.1029/jB090iB12p10136>
- Flóvenz, O.G., Spangenberg, E., Kulenkampff, J., Árnason, K., Karlsdothir, R., and Huenges, E., 2005, The role of electrical interface conduction in geothermal exploration, *Proc. World Geothermal Congress*.
- García-Fiscal, S., and Flores, C., 2018, Sensitivity of galvanic and inductive Induced Polarization methods to the Cole-Cole parameters, *Journal of Applied Geophys.*, 158, 1-10 <https://doi.org/10.1016/j.jappgeo.2018.05.008>
- García Gutiérrez, A., 2009, Estado térmico inicial del campo geotérmico de Los Humeros, Puebla, México, *Geotermia*, 22(1), 59-70.
- Gasperiškova, E., Newman, G., Feucht, D., and Arnason, K., 2021, 3D MT characterization of two geothermal fields in Iceland, *Geoth. Resources Council Trans.*, 35, 1667-1671.
- González-Partida, E., Barragán-Reyes, R.M., y Vázquez-Escobedo, R., 1992, Distribución y condiciones de formación de los minerales de arcilla en un campo geotérmico – El caso de Los Humeros, Estado de Puebla, *Revista Inst. de Geología, UNAM*, 10(1), 47-53.
- Granados-Chavarría, I., Calò, M., Figueroa-Soto, A., and Jousset, P., 2022, Seismic imaging of the magmatic plumbing system and geothermal reservoir of the Los Humeros caldera (Mexico) using anisotropic shear wave models, *J. Volcanol. Geoth. Res.*, 421, 107441, <https://doi.org/10.1016/j.jvolgeores.2021.107441>
- Gunderson, R., Cumming, W., Astra, D., and Harvey, C., 2000, Analysis of smectite clays in geothermal drill cuttings by the methylene blue method: for well site geothermometry and resistivity sounding correlation, *Proc. World Geothermal Congress*, Kyushu-Tohoku, Japan, 1175-1181.
- Gutiérrez-Negrín, L.C.A., and Izquierdo-Montalvo, G., 2010, Review and update of the main features of the Los Humeros geothermal field, Mexico, *Proc. World Geothermal Congress*, Bali, Indonesia.
- Heise, W., Caldwell, T.G., Bibby, H.M., and Bannister, S.C.F., 2008, Three-dimensional modeling of magnetotelluric data from the Rotokawa geothermal field, Taupo Volcanic Zone, New Zealand, *Geophys. J Int.*, 173, 740-750 <https://doi.org/10.1111/j.1365-246X.2008.03737.x>
- Hersir, G.P., Árnason, K., Vilhjálmsson, A.M., Saemundsson, K., Ágústsdóttir, P., and Fridleifsson, G.Ó., 2020, Krýsuvík high temperature geothermal area in SW Iceland: Geological setting and 3D inversion of magnetotelluric (MT) resistivity data, *J. Volcanol. Geoth. Res.*, 391, 106500 <https://doi.org/10.1016/j.jvolgeores.2018.11.021>

- Hoversten, G.M., and Morrison, H.F., 1982, Transient fields of a current loop source above a layered earth, *Geophysics*, 47, 1068-1077 <https://doi.org/10.1190/1.1441370>
- Izquierdo, M.G., 1993, Difracción de rayos X en la caracterización de especies arcillosas: un caso de aplicación en el pozo H-29 del campo de Los Humeros, Pue., *Geof. Intern.*, 32(2), 321-329.
- Jousset, P., Agustsson, K., Barison, E., Böhm, G., Caló, M., Chavarría, I.G., Farina, B., Gaucher, E., Loer, K., Martins, J., Pertou, M., Poletto, F., Saenger, E., Figueroa Soto, A., Toledo, T., Verdel, A., and Werner, C., 2020, Seismic structures of the Acoculco and Los Humeros geothermal fields, Deliverable 5.2, GEMex, Postdam. www.gemex-h2020.eu
- Jupp, D.L.B., and Vozzoff, K., 1975, Stable iterative methods for the inversion of geophysical data, *Geophys. J. Roy. astr. Soc.*, 42, 957-976 <https://doi.org/10.1111/j.1365-246X.1975.tb06461.x>
- Key, K., and Lockwood, A., 2010, Determining the orientation of marine CSEM receivers using orthogonal Procrustes rotation analysis, *Geophysics*, 75(3), F63-F70 <https://doi.org/10.1190/1.3378765>
- Layugan, D.B., Rigor, D.M., Apuada, N.A., Los Baños, C.F., and Olivar, R.E.R., 2005, Magnetotelluric (MT) resistivity surveys in various geothermal systems in Central Philippines, *Proc. World Geothermal Congress*, Antalya, Turkey.
- Lelli, M., Kretschmar, T., Cabassi, J., Doveri, M., Sánchez-Ávila, J.I., Gherardi, F., Magro, G., and Norelli, F., 2021, Fluid geochemistry of the Los Humeros geothermal field (LHGF – Puebla, Mexico): New constraints for the conceptual model, *Geothermics*, 90, 101983 <http://doi.org/10.1016/j.geothermics.2020.101983>
- Les Landes, A.A., Maurel, C., Lopez, S., and Calcagno, P., 2020, Hydrogeological model of Los Humeros: hydrothermal processes at the regional scale, Report 3.3, 2020 GEMex Report, Postdam, 47 pp. www.gemex-h2020.eu
- Lindsey, N.J., Kaven, J.O., Davatzes, N., and Newman, G.A., 2017, Compartmentalization of the Coso East Flank geothermal field imaged by 3-D full-tensor MT inversion, *Geophys. J. Int.*, 208, 652-662 <https://doi.org/10.1093/gji/ggw408>
- Los Baños, C.F., and Maneja, F.C., 2005, The resistivity structure of the Mahanagdong geothermal field, Leyte, Philippines, *Proc. World Geothermal Congress*, Antalya, Turkey.
- Maillet, R., 1947, The fundamental equations of electrical prospecting, *Geophysics*, 12(4), 529-556 <https://doi.org/10.1190/1.1437342>
- Manzella, A., Ungareli, C., Ruggieri, G., Giolito, C., and Fiordelisi, A., 2010, Electrical resistivity of the Travale geothermal field (Italy), *Proc. World Geothermal Congress*, Bali, Indonesia.
- Martínez-García, M., 1992, Electromagnetic induction in geothermal fields and volcanic belts, *Surveys in Geophysics*, 13, 409-434 <https://doi.org/10.1007/BF01903485>
- Martínez Serrano, R., and Alibert, C., 1994, Características geoquímicas de las rocas volcánicas del sistema geotérmico Los Humeros, Puebla y su relación con la mineralogía de alteración, *Geof. Intern.*, 33(4), 585-605.
- Martínez-Serrano, R.G., and Dubois, M., 1998, Chemical variations in chlorite at the Los Humeros geothermal system, Mexico, *Clays and Clay Minerals*, 46(6), 615-628.

- Melosh, G., Cumming, W., Benoit, D., Wilmarth, M., Colvin, A., Winick, J., Soto-Neira, E., Sussman, D., Urzúa-Monsalve, L., Powell, T., and Peretz, A., 2010, Exploration results and resource conceptual model of the Tolhuaca geothermal field, Chile, *Proc. World Geothermal Congress*, Bali, Indonesia.
- Muñoz, G., 2014, Exploring for geothermal resources with electromagnetic methods, *Surveys in Geophysics*, 35, 101-122 <https://doi.org/10.1007/S10712-013-9236-0>
- Nabighian, M.N., 1979, Quasi-static transient response of a conducting half-space: An approximate representation, *Geophysics*, 44, 1700-1705 <https://doi.org/10.1190/1.1440931>
- Norini, G., Carrasco-Núñez, G., Corbo-Camargo, F., Lermo, J., Hernández Rojas, J., Castro, C., Bonini, M., Montanari, D., Corti, G., Moratti, G., Piccardi, L., Chávez, G., Zuluaga, M.C., Ramírez, M., and Cedillo, F., 2019, The structural architecture of the Los Humeros volcanic complex and geothermal field, *J. Volcanol. Geoth. Res.*, 381, 312-329 <https://doi.org/10.1016/j.jvolgeores.2019.06.010>
- Nurmukhamedov, A.G., Chernev, I.I., Alekseev, D.A., and Yakovlev, A.G., 2010, 3D geoelectric model of the Mutnov steam hydrothermal deposit, *Izvestiya, Physics of the Solid Earth*, 46(9), 739-750 <https://doi.org/10.1134/S106935131009003X>
- Orellana, E., 1972, *Prospección eléctrica en corriente continua*, 523 pp, Paraninfo, Madrid.
- Palacios-Hartweg, L., and García-Velázquez, H., 1981, Informe geofísico del proyecto geotérmico Los Humeros-Derrumbadas. Estados de Puebla y Veracruz, Internal Report, Com. Fed. de Electricidad, 96 pp.
- Pinti, D.L., Clara Castro, M., López-Hernández, A., Han, G., Shouakar-Stash, O., Hall, C.M., and Ramírez-Montes, M., 2017, Fluid circulation and reservoir conditions of the Los Humeros Geothermal Field (LHGF), Mexico, as revealed by a noble gas survey, *J. Volcanol. Geoth. Res.*, 333-334, 104-115 <http://dx.doi.org/10.1016/j.jvolgeores.2017.01.015>
- Prol-Ledesma, R.M., 1990, Recent cooling in Los Humeros geothermal field (Mexico), inferred from clay minerals distribution, *Geoth. Res. Council Transactions*, 14(II), 959-964
- Pellerin, L., Johnston, J.M., and Hohmann, G.W., 1996, A numerical evaluation of electromagnetic methods in geothermal evaluation, *Geophysics*, 61, 121-130 <https://doi.org/10.1190/1.1443931>
- Raharjo, I.B., Maris, V., Wannamaker, P., and Chapman, D.S., 2010, Resistivity structures of Lahendong and Kamojan geothermal systems revealed from 3D magnetotelluric inversions, A comparative study, *Proc. World Geothermal Congress*, Bali Indonesia.
- Raiche, A.P., Jupp, D.L.B., Rutter, H., and Vozoff, K., 1985, The joint use of coincident loop transient electromagnetic and Schlumberger sounding to resolve layered structures, *Geophysics*, 50(10), 1618-1627.
- Reyes, N., Vidal, A., Ramírez, E., Arnason, K., Richter, B., Teingrimsson, B., Acosta, B., Acosta, O., and Camacho, J., 2011, Geothermal exploration at the Irruputunca and Olca volcanoes: pursuing a sustainable mining development in Chile, *Geoth. Resources Council Trans.*, 35, 983-986.
- Romo-Jones, J.M., Avilés-Esquivel, T., Arango-Galván, C., Ruiz-Aguilar, D., Salas-Corrales, J.L., Benediktsdóttir, A., and Hersir, G.P., 2020, Depth-average estimation of 1D subsurface resistivity from MT data in Los Humeros geothermal field, Mexico, *Proc. World Geothermal Congress*, Reykjavik, Iceland, 9 pp

- Romo-Jones, J.M., Arango-Galván, C., Ruiz-Aguilar, D., Avilés-Esquivel, T., and Salas-Corrales, J.L., 2021, 3D electrical resistivity distribution in Los Humeros and Acoculco geothermal zones, Mexico, *Proc. First EAGE Workshop on Geothermal Energy in Latin America*, 1-5.
- Sakindi, G., 2015, Three-dimensional inversion of magnetotelluric data: Geological/Geothermal interpretation of Asal geothermal field, Djibouti, M.Sc. Thesis, Faculty of Earth Sciences, Univ. of Iceland, 111 pp.
- Samrock, F., Kuvshinov, A., Bakker, J., Jackson, A., and Fisseha, S., 2015, 3-D analysis and interpretation of magnetotelluric data from the Aluto-Langano geothermal field, Ethiopia, *Geophys. J. Int.*, 202, 1923-1948 <https://doi.org/10.1093/gji/ggv270>
- Seismocontrol, S.A., 2005, Estudio de resistividad con transitorio electromagnético en el campo geotérmico de Los Humeros, Puebla, Internal Report GF-HU-08-05 for the Comis. Federal de Electricidad.
- Smith, R.S., and West, G.F., 1989, Field examples of negative coincident-loop transient electromagnetic responses modeled with polarizable half-planes, *Geophysics*, 54, 1491-1498 <https://doi.org/10.1190/1.1442613>
- Spichak, V., and Manzella, A., 2009, Electromagnetic soundings of geothermal zones, *J. Applied Geophys.*, 68, 459-478 <https://doi.org/10.1016/j.jappgeo.2008.05.007>
- Spies, B.R., 1989, Depth of investigation in electromagnetic sounding methods, *Geophysics*, 54, 872-888 <https://doi.org/10.1190/1.1442716>
- Talebi, B., Khosrawi, K., and Ussher, G., 2005, Review of resistivity surveys from the NW Sabalan geothermal field, Iran, *Proc. World Geothermal Congress*, Antalya, Turkey.
- Uchida, T., 1995, Resistivity structure of Sumikawa geothermal field, northeastern Japan, obtained from magnetotelluric data, *Proc. World Geothermal Congress*, Florence, Italy.
- Uchida, T., Lee, T.J., Honda, M., Asuari and Andan, A., 2002, 2-D and 3-D interpretation of magnetotelluric data in the Bajawa geothermal field, central Flores, Indonesia, *Bull. Geol. Surv. of Japan*, 53(2/3), 265-283.
- Uchida, T., 2005, Three-dimensional magnetotelluric investigation in geothermal fields in Japan and Indonesia, *Proc. World Geothermal Congress*, Antalya, Turkey, 12 pp.
- Uchida, T., 2010, Three-dimensional interpretation of AMT data in Ogiri geothermal field, Japan, *Proc. World Geothermal Congress*, Bali, Indonesia.
- Uchida, T., Takakura, S., Ueda, T., Adachi, M., Ozeki, H., Kamada, K., and Sato, T., 2011, 3D Magnetotelluric survey at the Yanaizu-Nishiyama geothermal field, Northern Japan, *Proc. 9th Asian Geothermal Symposium*.
- Urban, E., and Lermo, J.F., 2013, Local seismicity in the exploitation of Los Humeros geothermal field, Mexico, *Proc. Thirty-Eighth Workshop on Geothermal Reservoir Engineering*, Stanford Univ.
- Ushijima, K., Mustopa, E.J., Jotaki, H., and Mizunaga, H., 2005, Magnetotelluric soundings in the Takigami geothermal area, *Proc. World Geothermal Congress*, Antalya, Turkey.
- Ussher, G., Harvey, C., Johnstone, R., and Anderson, E., 2000, Understanding the resistivity observed in geothermal systems, *Proc. World Geothermal Congress*, 1915-1920.

Verma, S.K., and Sharma, S.P., 1995, Focused resolution of thin conducting layers by various dipole EM systems, *Geophysics*, 60, 381-389 <https://doi.org/10.1190/1.1443774>

Wannamaker, P.E., Doerner, W.M., and Hasterok, D.P., 2007, Integrated dense array and transect MT surveying at Dixie Valley geothermal area, Nevada; structural controls, hydrothermal alteration and deep fluid sources, *Proc. Thirty-Second Workshop on Geoth. Reservoir Engineering*, Stanford Univ., 6 pp.

Yáñez, C., 1980, Informe geológico del proyecto geotérmico Los Humeros – Las Derrumbadas, estados de Puebla y Veracruz, Internal Report, Comisión Federal de Electricidad, 59 pp.